Image Analysis of the Carotid Artery: A (Semi-)Automatic Approach

Andrés M. Arias Lorza

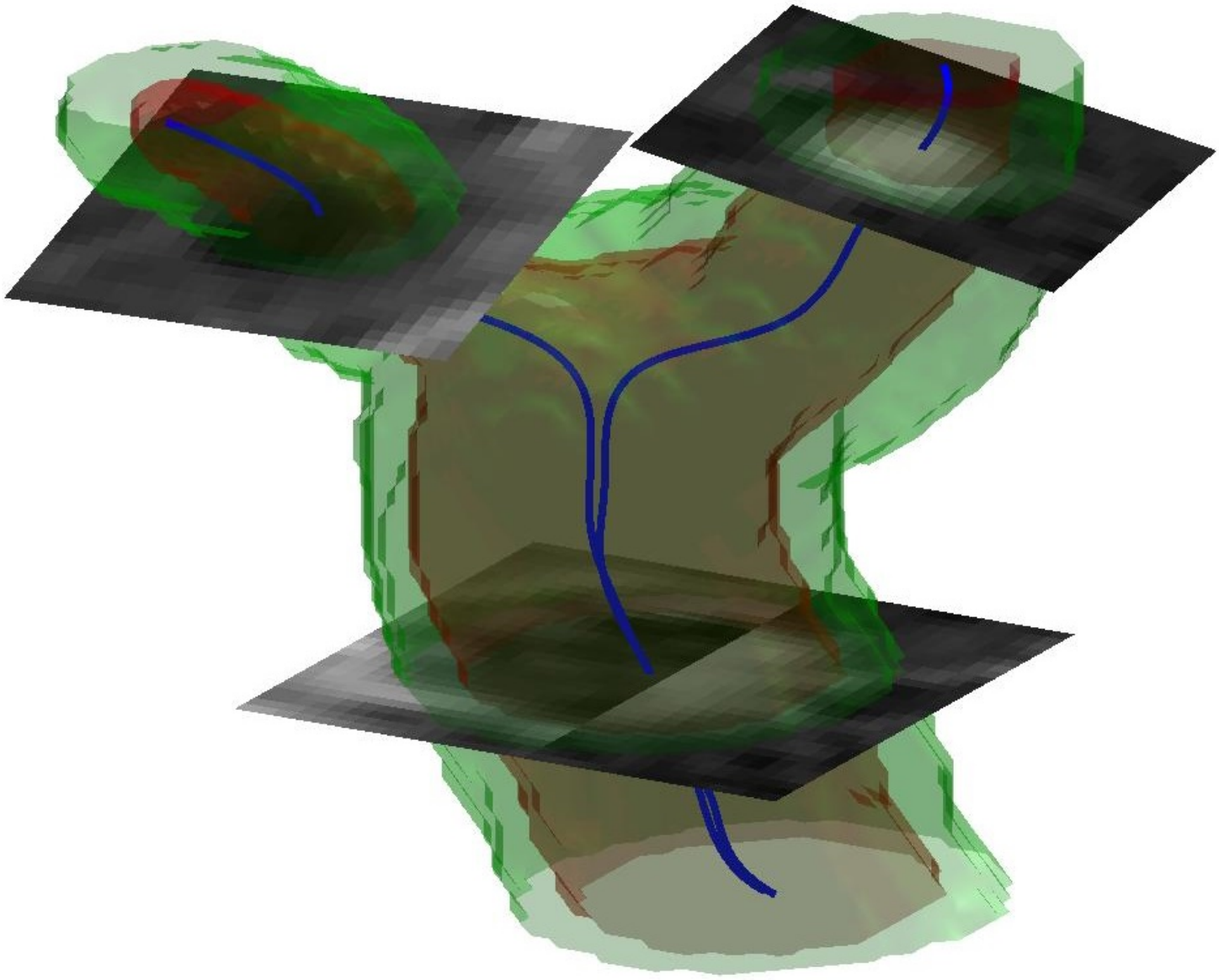

Image Analysis of the Carotid Artery: A (Semi-)Automatic Approach

Andrés M. Arias Lorza

Colophon

Cover design by the author using Matlab. The graphic on the cover represents a segmented wall of the carotid artery, together with the centerline overlaying cross-sections of Black-Blood MRI and the registered Phase-Contrast MRI.

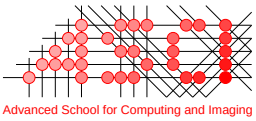

This work was carried out in the ASCI and COEUR graduate schools.
ASCI dissertation series number 376.

The research described in this thesis was carried out at the Departments of Radiology and Medical Informatics of the Erasmus MC – University Medical Center Rotterdam (Rotterdam, the Netherlands).
This work was part of the STW Biostress project and it was financially supported by the Netherlands Organization for Scientific Research (NWO).

Financial support by the Dutch Heart Foundation for the publication of this thesis is gratefully acknowledged. Additional financial support for printing of this thesis was kindly provided by the department of Radiology, Erasmus MC, and ASCI.

ISBN 978-94-6332-249-2

Printed by GVO drukkers & vormgevers B.V.

Image Analysis of the Carotid Artery: A (Semi-)Automatic Approach

Beeldanalyse van de Halsslagader: Een (Semi-)Automatische Aanpak

Thesis

to obtain the degree of Doctor from the
Erasmus University Rotterdam
by command of the
rector magnificus

Prof.dr. H.A.P. Pols

and in accordance with the decision of the Doctorate Board.
The public defence shall be held on

Tuesday 31 October 2017 at 13:30 hrs
by

Andrés M. Arias Lorza
born in Cali, Colombia

Erasmus University Rotterdam

Doctoral Committee:

Promotor:	**Prof.dr. W.J. Niessen**
Other members:	**Dr.ir. J.J. Wentzel**
	Prof.dr.ir. M. Breeuwer
	Prof.dr. D.W.J. Dippel
Copromotor:	**Dr. M. de Bruijne**

To my parents,

Ana Milena Lorza Mazuera
&
Guillermo Alberto Arias Marin

Contents

Colophon **iii**

1 Introduction **1**
1.1 Carotid Atherosclerosis . . . 1
1.2 Carotid Artery Imaging . . . 2
1.3 Carotid Artery Image Processing . . . 2
1.3.1 Thesis Overview . . . 2
1.3.2 Segmentation (Chapters 2-4) . . . 3
1.3.3 MRI-US Registration (Chapter 5) . . . 4
1.3.4 Centerline Extraction (Chapter 6) . . . 5
1.3.5 Application in Population Studies (Chapter 7) . . . 5

2 Carotid Artery Wall Segmentation in Multispectral MRI by Coupled Optimal Surface Graph Cuts **7**
2.1 Introduction . . . 8
2.2 Method . . . 9
2.2.1 Method overview . . . 9
2.2.2 Initialization by centerline extraction . . . 10
2.2.3 Optimal surface graph construction and optimization . . . 11
2.3 Experiments and Results . . . 15
2.3.1 Image Data . . . 15
2.3.2 Manual annotations . . . 15
2.3.3 Preprocessing . . . 16
2.3.4 Inter-observer variability . . . 17
2.3.5 Parameter Tuning . . . 17
2.3.6 Comparison with manual annotations . . . 18
2.3.7 Reproducibility analysis . . . 22
2.3.8 Comparison with Other methods . . . 23
2.4 Discussion . . . 24
2.5 Conclusion . . . 26

3 Maximization of Regional probabilities using Graphs: Application to Carotid Artery Segmentation in MRI **27**
3.1 Introduction . . . 28
3.2 Method . . . 30

3.2.1 Optimal Surface Graph Method . . . 30
3.2.2 Regional Information and OSG . . . 31
3.2.3 Regional Probability Maps . . . 33
3.3 Experiments and Results . . . 33
3.3.1 Image Data and preprocessing . . . 33
3.3.2 Experiments . . . 34
3.3.3 Feature set . . . 34
3.3.4 SVM classification . . . 35
3.3.5 Graph Parameter Optimization . . . 35
3.3.6 Methods Comparison Results . . . 37
3.3.7 Performance Evaluation of the Method . . . 38
3.4 Discussion . . . 41
3.5 Conclusion . . . 43

4 Carotid artery lumen segmentation on 3D free-hand ultrasound images using surface graph cuts 45
4.1 Introduction . . . 46
4.2 Method . . . 46
4.3 Experiments and Results . . . 49
4.4 Discussion and Conclusion . . . 51

5 Automated Registration of Free-hand B-mode Ultrasound and MRI of the Carotid Arteries Based on Geometrical Features 53
5.1 Introduction . . . 54
5.2 Method . . . 57
5.2.1 US-MRI Registration Framework . . . 57
5.2.2 Optimal Surface Graph Method for Lumen Segmentation . . . 60
5.3 Experiments . . . 62
5.3.1 Data . . . 62
5.3.2 Evaluation of MRI Lumen Segmentation . . . 62
5.3.3 Evaluation of US Lumen Segmentation . . . 63
5.3.4 Evaluation of Registration Accuracy . . . 63
5.4 Results . . . 64
5.4.1 US Lumen Segmentation Results . . . 64
5.4.2 Registration Results . . . 65
5.5 Discussion . . . 67
5.6 Conclusion . . . 70

6 Cooperative Carotid Artery Centerline Extraction in MRI 71
6.1 Introduction . . . 72
6.2 Method . . . 74
6.2.1 Method overview . . . 74
6.2.2 Cost image . . . 74
6.2.3 Minimum cost path using anisotropic fast marching . . . 74
6.2.4 Cooperative centerline extraction . . . 76
6.3 Experiments and Results . . . 77

6.3.1 Image Data . . . 77
6.3.2 Manual annotations . . . 78
6.3.3 Preprocessing . . . 78
6.3.4 Parameter selection and Configuration . . . 79
6.3.5 Evaluation Metric . . . 80
6.3.6 Comparison with manual annotations . . . 80
6.3.7 Results in a large population data set . . . 81
6.4 Discussion . . . 82
6.5 Conclusion . . . 84

7 Comparison of CT and MRI for detection and quantification of carotid artery calcification: The Rotterdam Study 85
7.1 Background . . . 86
7.2 Material And Methods . . . 86
7.2.1 Setting . . . 86
7.2.2 Assessment of CT-based calcification . . . 87
7.2.3 Assessment of MRI-based calcification . . . 87
7.2.4 Assessment of history of stroke . . . 88
7.2.5 Statistical analysis . . . 88
7.3 Results . . . 89
7.4 Discussion . . . 90
7.5 Conclusion . . . 93

8 Summary and Discussion 95
8.1 Summary . . . 95
8.1.1 Segmentation . . . 95
8.1.2 MRI-US Registration . . . 96
8.1.3 Vessel Centerline Extraction . . . 96
8.1.4 Population Studies . . . 97
8.2 Discussion . . . 97

Bibliography 99

Samenvatting 107

PhD Portfolio 111

Publications 113

Acknowledgments 115

Curriculum Vitae 117

Chapter One

Introduction

1.1 Carotid Atherosclerosis

Cardiovascular diseases are among the leading causes of death worldwide [3]. Between them, cerebrovascular disease ranks as the third leading cause of death [67]. Inflammation in the arterial walls, leading to the formation of a plaque also known as atherosclerosis is a common vascular disease [69]. This process frequently occurs in a pair of vessels located in the neck called the carotid arteries which supply the brain and muscles of the face with blood (see Figure 1.1). Atherosclerotic plaques in the carotid arteries can rupture and may cause thrombus formation and embolization of plaque content and/or thrombus into the distal intracranial vasculature resulting in a stroke [18, 38, 90]. Therefore, preventing plaque rupture is essential.

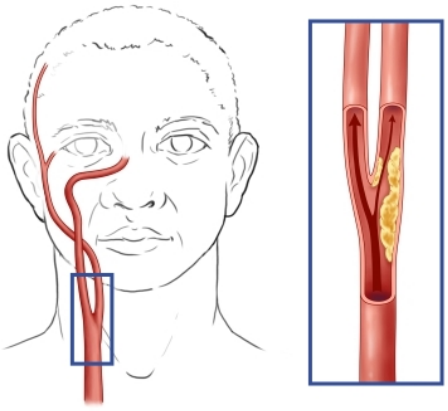

Figure 1.1. Carotid artery and plaque formation. The common carotid artery splits into two branches, the external and internal carotid arteries that provide blood to the head. A plaque in the artery, here shown as a yellow mass, may reduce blood flow through the lumen (central space in the artery through which blood flows) or be a source of emboli which can travel to the brain and cause stroke. Image source: http://chicago.medicine.uic.edu/cms/One.aspx?portalId=506244&pageId=2862343

1.2 Carotid Artery Imaging

To assess the risk of plaque rupture, it is important to detect plaque and to accurately quantify lumen narrowing, plaque volume, plaque morphology and plaque composition [84]. In case of lower rupture risk, the patient can be treated with medication [26, 40], whereas in patients with higher risk a surgical procedure is generally advised [71]. Currently, the treatment decision is primarily based on lumen narrowing, but including more features could improve risk assessment.
Detection of plaque and quantification of the vessel and plaque properties is possible using various imaging modalities. Different modalities supply complementary information on the carotid artery wall and plaque therein [22, 39, 97]. Even though most imaging modalities show the lumen and artery wall, each one emphasizes different properties: angiography is especially useful to assess the stenosis severity; Computed Tomography (CT) visualizes plaque calcifications well; Magnetic Resonance Imaging (MRI) can be used for assessing intra-plaque hemorrhage, and necrotic cores; finally, Ultrasound (US) shows ulcerations well. Figure 1.2 shows examples of carotid artery images from the same patient using US and MRI.

1.3 Carotid Artery Image Processing

After visualizing the carotid artery, several image analysis techniques can be applied for plaque detection and plaque and vessel quantification. The main techniques are segmentation, registration, and centerline extraction. Segmentation consists of the annotation of the contours, typically the contours of the lumen and outer wall, and the different plaque components. Using the contours, volumes and morphology can be derived. Image registration is the process to spatially transform an image, so at the end the images of the carotid arteries are aligned and comparable. This allows side-by-side comparison of images, which can be used to better inspect the carotid artery and its components. Centerline extraction provides information about the location and shape of the artery by marking its center points, which allows to measure several shape features. Note that to obtain better results it is typically necessary to combine these methods, so for instance to achieve better segmentations, a prior registrations and centerline extraction may be required (see Chapters 2 and 3).

1.3.1 Thesis Overview

Applying all these image processing methods manually is a difficult and time consuming process, subject to inter and intra-observer variability [46]. Therefore, (semi-) automatic techniques are highly desirable. This thesis aims to develop and evaluate new (semi-)automatic methods for processing of carotid artery images. While the methods presented in this thesis are only applied to US and MRI, they can be generalized to other modalities such as CT. First, we propose new segmentations techniques of the arterial wall in MRI and US (Chapters 2-4). Next, we present a registration approach between MRI and US (Chapter 5). Subsequently, we present an approach

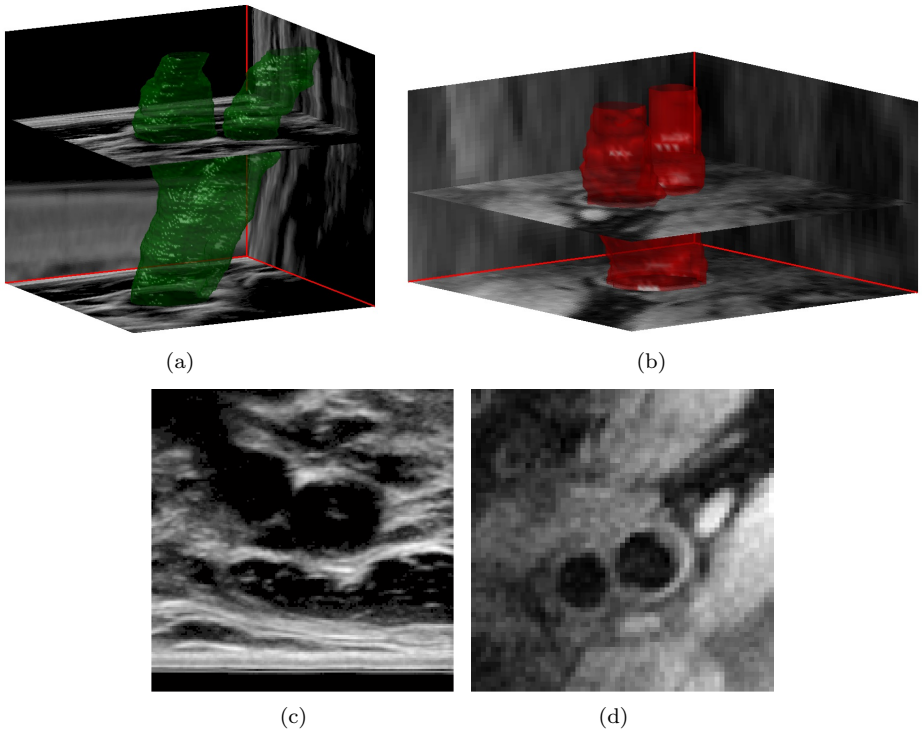

Figure 1.2. Multimodal carotid artery imaging. A 3D reconstruction of an US scan (a), and a MRI scan of the carotid artery of the same patient (b). The green and red volumes represent the artery in both modalities. 2D slices intersecting the arteries taken at similar position close to the bifurcation on both modalities are shown in (c) and (d).

to detect the artery centerlines (Chapter 6). Finally, some of the developed methods are applied in a population study to compare plaque calcifications derived from CT and MRI (Chapter 7). Main findings are summarized and discussed in Chapter 8.

1.3.2 Segmentation (Chapters 2-4)

Segmentation of the arterial wall is important for assessing the presence and for the proper analysis and severity of atherosclerotic plaques. In both MRI and US the arterial wall can be visualized, with the special advantage that both modalities do not involve any ionizing radiation, and US is a relatively low-cost modality.
(Semi-)automatic vessel segmentation methods for different vessel anatomies and different imaging modalities have been presented previously [60]. In most methods, the vessel is modeled as a 3D surface. Image intensity and gradient magnitude are commonly used as image features. For optimization of the model, graph cuts, snakes, contour evolution models and level sets are currently the most popular. For the specific case of carotid artery segmentation, several automatic and semi-automatic methods

have been proposed to segment the arterial wall in MRI [45, 53, 59, 94, 103, 110] and US images [50, 63, 101]. However, still this is a challenging problem, as often errors are present at the artery bifurcation or a high amount of user interaction is required.
In Chapter 2, we use a multi-surface graph cut segmentation method which allows the integration of prior shape information [76] to segment the carotid artery inner and outer wall in MRI. Graph cut optimizers have recently become very popular because they can achieve a global optimum with low processing times. The integration of shape information in the graph structure of the method contributes to improved segmentation in high curvature areas such as the carotid bifurcation. Furthermore, segmentation methods as [76], allow to simultaneously find both inner and outer wall, permitting to integrate topology information in the method.
The method presented in Chapter 2 only uses edge information as segmentation feature, and due to the presence of noise and lack of contrast in the carotid MRI images, some errors were obtained specially at the outer border of the artery wall. Therefore, in Chapter 3 we extended this method by including more features apart from edge information. In this new segmentation method several descriptive features of the regions to segment are used to obtain regional probability maps, and the graph cut optimizes the segmented regions that maximize the probabilities per region.
In Chapter 4 we applied a similar method as used in Chapter 2 to segment the inner border of the artery in US, however we extended it using an iterative approach to compensate for possible errors in the graph initialization.

1.3.3 MRI-US Registration (Chapter 5)

Registration is required for side-by-side visualization and analysis of different imaging modalities. Registration between MRI and US is clinically relevant as some plaque components are better differentiated in the different modalities. However, since US and MRI have very different image appearance, registration of these images is a challenging problem.
Registration is achieved by finding a transformation that minimizes a dissimilarity metric between images. This dissimilarity measures the difference between image features (image intensities, landmarks).
Most registrations approaches use image intensity dissimilarity metrics based on correlation, mutual information, or gradients. However, due to the different image appearance of MRI and US, registration based on only image intensity dissimilarity may result in errors [20].
MRI-US registration of the carotid artery has been addressed in previous works [20,24, 43,72,91]. However, generally the registration accuracy is not good or a high amount of user interaction is needed. Furthermore, it was shown in [20] that the addition of geometrical features such as the centerline as input for the registration is useful. In Chapter 5, we therefore propose a novel automated method for registering US and MRI images of the carotid artery. The method is an extension of [20] and adds geometric information in the form of lumen segmentations to improve registration performance, where the lumen is segmented in MRI and US applying the presented methods in Chapters 2 and 4 respectively.

1.3.4 Centerline Extraction (Chapter 6)

Extracting the artery centerline is important for analyzing vessel geometry [94]. Additionally, the segmentation and registration methods presented in Chapters 2-5 require a vessel centerline as input. Large errors in extracted centerlines likely result in wrong segmentations and/or registrations.
There are two main types of approaches to extract vessel centerlines using different image modalities: global optimization methods based on minimum cost paths, and local approaches [85]. Local methods include tracing the medial axis from inscribed disks or spheres [4, 19], finding the centers of intensity ridge traversals [7, 10], and finding maxima points using filters [41, 79].
Minimum cost paths methods have the advantage to be robust to image artifacts [94]. However, defining a proper cost especially at the bifurcation region of the artery is difficult. This may cause methods to detect the centerline based on minimum cost paths to fail. The carotid artery centerline is defined by the combination of two minimum cost paths, from common to internal and from common to external. In cases where errors in the cost images are present, a cooperatively approach to detect both paths may result in better centerlines. In Chapter 6 we use this idea to develop a new carotid artery centerline detection approach in MRI where both paths are detected cooperatively. Here in the cost to extract each centerline, we integrate a constraint section derived from geometrical and anatomical information from the neighbor centerline, to avoid errors as intersections between centerlines.

1.3.5 Application in Population Studies (Chapter 7)

One of the main advantages of (semi-)automatic approaches is the ability to process high volumes of data as they are e.g. obtained in population or clinical studies. Several population studies included carotid artery images and also (semi-)automatic processing techniques have been applied to those data in the past [87, 98, 106].
In certain populations, a relevant topic is to use other imaging modalities than CT to avoid radiation exposure. In the specific case of the carotid artery, plaque calcifications are commonly visualized in CT [22]. In Chapter 7, we compare the quantified calcium volumes in CT and MRI to evaluate whether MRI can replace CT to detect plaque calcifications. To do this, we use a semi-automatic method to register several MRI sequences, which are further used to manually annotate the calcifications, and computer their volumes. These volumes are compared to manually measured calcium volumes in CT.

Chapter Two

Carotid Artery Wall Segmentation in Multispectral MRI by Coupled Optimal Surface Graph Cuts

Abstract — We present a new three-dimensional coupled optimal surface graph-cut algorithm to segment the wall of the carotid artery bifurcation from Magnetic Resonance (MR) images. The method combines the search for both inner and outer borders into a single graph cut and uses cost functions that integrate information from multiple sequences. Our approach requires manual localization of only three seed points indicating the start and end points of the segmentation in the internal, external, and common carotid artery. We performed a quantitative validation using images of 57 carotid arteries. Dice overlap of 0.86 ± 0.06 for the complete vessel and 0.89 ± 0.05 for the lumen compared to manual annotation were obtained. Reproducibility tests were performed in 60 scans acquired with an interval of 15 ± 9 days, showing good agreement between baseline and follow-up segmentations with intraclass correlations of 0.96 and 0.74 for the lumen and complete vessel volumes respectively.

Based upon: Andrs M. Arias-Lorza, Jens Petersen, Arna van Engelen, Mariana Selwaness, Aad van der Lugt, Wiro J. Niessen, and Marleen de Bruijne, "Carotid Artery Wall Segmentation in Multispectral MRI by Coupled Optimal Surface Graph Cuts", *published* in IEEE Transactions on Medical Imaging, 2015.

2.1 Introduction

Atherosclerosis is one of the primary causes of death in the world [67]. Atherosclerotic plaques in the carotid arteries may rupture causing thrombus formation and embolization of plaque content and/or thrombus into the distal intracranial vessel resulting in a stroke [90]. For risk assessment, detection of plaque and accurate quantification of plaque volume is important.

Magnetic Resonance (MR) enables 3D imaging of the carotid artery vessel wall [1,93]. For a proper analysis of the vessel wall, segmentation of both vessel lumen and outer vessel wall is required. Manual segmentation of the vessel walls in MR images is a time consuming process and subject to inter-observer variability [46]. Therefore, automatic techniques for segmenting the vessel wall are highly desirable.

Several automatic and semi-automatic methods have been proposed to segment the artery wall in MR images [5, 45, 53, 59, 94, 103, 110]. The methods presented in [53, 59, 94] are based on deformable models and can only segment the inner border. [5, 45, 103, 110] are able to segment inner and outer artery walls. Van 't Klooster et al. [110] proposed a 3D deformable vessel model, in which a vessel is modeled using a cylindrical surface that can be modified by moving control points located on the model surface. Good results were reported on Proton Density Weighted (PDw) Black-Blood MRI (BBMRI) images. However, only the Common Carotid Artery (CCA) and not the bifurcation region were segmented. This method also uses a local optimization procedure with the lumen segmentation as initialization, which may get stuck in a local optimum for instance in diseased vessels where the distance between the inner and outer wall is large. Hameeteman et al. [45] extended this method with a learning-based postprocessing step. In this approach, two separate cylindrical deformable surface models must be used to segment from CCA to the Internal Carotid Artery (ICA), and from CCA to the External Carotid Artery (ECA), which may lead to inaccuracies in the bifurcation area. Recently, Ukwatta et al. [103] proposed a globally optimal evolution approach for segmenting the carotid artery wall from BBMRI images. They obtained good results segmenting the complete bifurcation region with low processing times. This method requires the initial estimation of the intensity probability density functions of the lumen, wall, and background using marks of the three regions on a 2D transverse slice. Therefore, problems may arise at sections of the artery that are different from the estimated probability density functions.

Graph-based methods have been used for segmenting various types of vessels on several imaging modalities obtaining promising results [5, 11, 36, 66, 120]. Most common are voxel-based graph cut methods which represent the voxels of an image as vertices in a graph. Generally, in these approaches all vertices are connected to the sink and source vertices, and only neighbor vertices are linked. This approach allows cuts between neighboring voxels to segment foreground and background regions. A fully automatic voxel-based graph method to segment the aortic arch and carotid artery from CTA scans was proposed by Freiman et al. [36]. Bauer et al. [11] proposed another voxel-based graph method to segment vessels, in which an energy function that combines gradient magnitude information and the distance to an initialization shape is minimized.

A second class of graph-based methods is the optimal surface methods [5, 61, 65, 76,

120]. Here the graph vertices represent image positions, and these are arranged in columns. Each of these columns intersects the sought surface, and the positions where the columns intersect the surface discretely represent the segmentation solution. This construction makes it possible to enforce topology constraints and to incorporate an initialization volume in the graph structure. Often, the graph is defined based on a coarse initial segmentation. Petersen et al. [76] proposed to generate the graph columns from an initial segmentation surface using non-intersecting columns based on flow lines and applied this to segment airways in CT images. These non-intersecting columns avoid self-intersecting surface results, making it possible to segment high curvature surfaces such as the bifurcation of airways or vessels. In a preliminary study of the present work, we adapted this approach to segment the carotid artery wall on individual MRI sequences [5]. However, if the image information of the individual MRI sequences is combined and integrated into a surface graph, it may provide more accurate border locations since different image sequences have better contrast either at the inner or outer wall.
In this chapter, we present an extension of this previous work [5] which uses an optimal surface graph to segment the complete carotid artery wall bifurcation on MRI images using minimal user interaction. This method guarantees global minimization of a cost function, ensuring smooth surfaces and topological constraints between surfaces. The contributions of this chapter are as follows:

- New graph edge cost function that integrates information from several images.
- Initialization using an automated centerline extraction method as opposed to [5] which requires a lumen segmentation.
- A much extended validation compared to [5]: 57 carotid arteries in contrast to 32, parameter optimization and evaluation by full data set evaluation using a cross-validation approach in contrast to data set division, many more manually annotated cross-sections (one for every 1mm centerline in contrast to 6 cross-sections per artery at random positions).
- We present improved results compared to [5]. Additionally, we extended the evaluation including inter-observer variability analysis, scan-rescan reproducibility test, and comparison with a state-of-the-art MRI artery wall segmentation method [45] on a public database.

2.2 Method

2.2.1 Method overview

The main steps of the method are:

1. Obtain a 3D coarse segmentation of the lumen as initialization. This segmentation is obtained by a dilation of an extracted artery centerline.
2. Based on the initialization construct the surface graph. The steps to construct the graph are:

(a) Obtain from the initialization the graph column trajectories.

(b) On the graph column trajectories assign the graph vertices.

(c) Assign graph edges between vertices with a respective cost. The cost for edges between graph columns is given by a constant value, while the cost of the edges in a column is a function of the image information.

3. Compute minimum graph cut. The segmented surface is located at the cut locations.

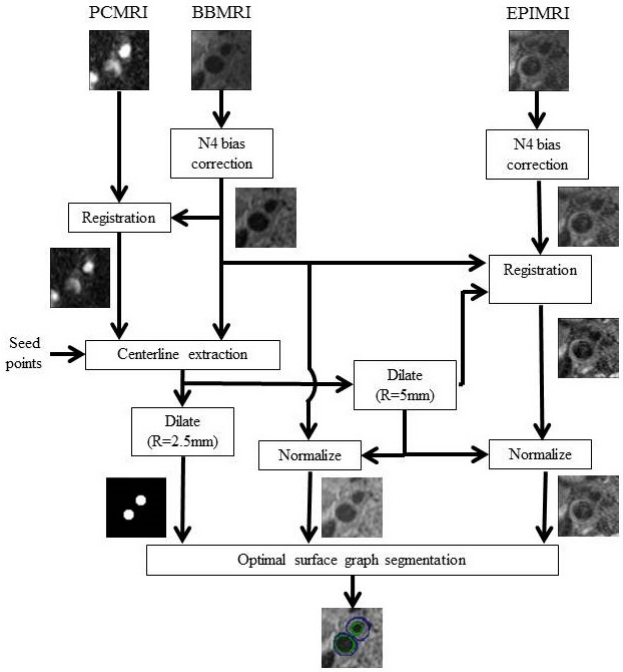

Figure 2.1. Schematic of the segmentation method. At the top the used images are shown, next are depicted the preprocessing steps. Finally, at the bottom the segmentation is shown using the proposed method.

2.2.2 Initialization by centerline extraction

To build the graph we require a coarse initial segmentation. From this initial segmentation the graph columns are constructed. The coarse initial segmentation is obtained by computing the centerline of the vessel lumen using the semi-automatic centerline extraction method proposed by Tang et al. [94]. In this method, the lumen centerline is determined as the minimum cost path between user-defined seed points in the common $\boldsymbol{x}_c$, internal $\boldsymbol{x}_i$, and external $\boldsymbol{x}_e$ carotid arteries. Two minimum cost paths are computed, one between $\boldsymbol{x}_c$ and $\boldsymbol{x}_i$ (we denote the set of points that define this path

by $\boldsymbol{C}^i$), and the other between $\boldsymbol{x}_c$ and $\boldsymbol{x}_e$ ($\boldsymbol{C}^e$). The cost is defined by a combination of the inverse of medialness filtering [41] and inverse of lumen intensity similarity metric [94] outputs. The minimum cost path is obtained by applying Dijkstra's algorithm. Subsequently, the centerline is refined by re-computing the minimum cost path after multi-planar reformatting perpendicular to the centerline [94]. The two obtained centerlines $\boldsymbol{C}^i$ and $\boldsymbol{C}^e$ are connected in order to have the centerline of the complete artery: $\boldsymbol{C} = \boldsymbol{C}^i \cup \boldsymbol{C}^e$. Finally, we obtain a 3D binary image representation of the centerlines I^c: $\mathbb{Z}^3 \rightarrow \{0, 1\}$ by mapping the centerline set of image positions $\boldsymbol{C}$ to a binary scalar space I^c.
A coarse approximation of the lumen Q: $\mathbb{Z}^3 \rightarrow \{0, 1\}$ is obtained by computing a binary morphological dilation of I^c with a disk structuring element with radius R.

2.2.3 Optimal surface graph construction and optimization

Based on the coarse initial segmentation Q, we construct the graph $G = (V, E)$ with vertices V and edges E. The vertices are associated with positions in the image, and represent potential border locations. As in [76], these are grouped by non-intersecting graph columns, which guarantee non self-intersecting segmentations. The set of edges E connects the vertices of the graph, and represents the association between vertices. High-cost edges are expected to connect vertices of the same class. Low-cost edges are expected between vertices from different classes. The segmentation solution is given by the minimum graph cut, which represents the separation of the graph vertices in two sets: source part $V_s \subseteq V$ (foreground) and sink part $V_t \subseteq V$ (background), such that $V_t = V \backslash V_s$. In our case we have two surfaces to segment, the inner and the outer carotid artery wall, therefore coupling two graphs is necessary to find both borders simultaneously. One graph is used to separate the vessel lumen from the wall and background while the other graph is used to separate the lumen and wall from the background. We represent the coupling of graphs by connecting vertices of the two sub-graphs. This graph construction approach coupling several graphs is described in detail in section 2.2.3.2. A minimal cut minimizes the total cost of the edges that are being cut [52]:

$$\begin{aligned} &\min_{v_i \in V_s,\ v_j \in V_t} \sum Cost(v_i \rightarrow v_j), \\ &s.t. \quad s \in V_s, t \in V_t, V_t = V \backslash V_s, (v_i \rightarrow v_j) \in E, \end{aligned} \tag{2.1}$$

where $Cost(v_i \rightarrow v_j)$ is the associated cost of the directed edge $v_i \rightarrow v_j$ between the vertices v_i and v_j, and the vertices s and t denote the source and sink points of the graph. This minimization is solved by applying a min-cut/max-flow optimization algorithm [17].
The following three subsections explain in detail the graph construction approach.

2.2.3.1 Graph column trajectories

To construct the graph, first the graph columns have to be traced in the image. Each graph column is composed of a set of vertices representing the possible image positions

the surface can take. The graph column trajectories are traced from the surface voxels of the coarse initial segmentation Q. This set of image locations at the starting surface is represented by $\mathbf{X}_Q = \{\, \boldsymbol{x}_{i,0} |\, i \in \{0, .., N_Q\}\}$, where N_Q is the number of voxels on the surface.

A requirement to guarantee segmented surfaces that do not self-intersect is that the graph columns do not intersect each other [76]. Graph columns based on flow lines as described in [76] have these characteristics. Here, the graph columns are traced from $\boldsymbol{x}_{i,0}$, and follow the flow lines $\boldsymbol{f}_i$: $\mathbb{R} \rightarrow \mathbb{R}^3$ of the gradient vector field of a Gaussian smoothing of the initial segmentation represented by Q_σ: $\mathbb{R}^3 \rightarrow \mathbb{R}$, where σ^2 represents the variance of the Gaussian kernel. That is, the flow lines $\boldsymbol{f}_i$ are obtained by solving:

$$\frac{\partial \boldsymbol{f}_i}{\partial t}(t) = \nabla Q_\sigma(\boldsymbol{f}_i(t)), \tag{2.2}$$

with initial value given by $\boldsymbol{f}_i(0) = \boldsymbol{x}_{i,0}$. These flow lines vary in length depending on the point where the gradient of the scalar field Q_σ flattens. A schematic of a gradient vector field of a smoothed segmentation Q_σ is shown in Figure 2.2(a). A 2D sketch of the flow lines traced along this gradient vector field, starting from the graph vertices located at the initialization surface is depicted in Figure 2.2(b).

2.2.3.2 Graph construction

Graph vertices Solving Eq. 2.2 for all $\boldsymbol{x}_{i,0} \in \mathbf{X}_Q$ such that $\boldsymbol{f}_i(0) = \boldsymbol{x}_{i,0}$ leads to all graph columns. Each individual flow line $\boldsymbol{f}_i$ defines two graph columns: V_i^{Inner} and V_i^{Outer}, whose vertices represent sets of possible positions for the inner and the outer wall respectively.

Using the Runge-Kutta-Fehlberg method, the solution of $\boldsymbol{f}_i(t)$ in Eq. 2.2 is approximated at regular intervals δ defining the positions of the graph vertices by:

$$\boldsymbol{x}_{i,k} = \boldsymbol{f}_i(k\delta), \tag{2.3}$$

where $k \in \mathbb{Z}$, $\boldsymbol{x}_{i,k}$ is the image position associated with the graph vertex $v_{i,k}^m$. For each vertex $v_{i,k}^m$, $m \in M$ and $M = \{Inner, Outer\}$ represent the set of surfaces to find. The vertex $v_{i,k}^m$ is part of the graph column V_i^m, such that $V_i^m = \left\{ v_{i,k}^m \middle|\, k = -I_i, I_i + 1, \ldots, 0, \ldots, O_i - 1, O_i \right\}$, where the vertices $v_{i,0}^m$ represent positions at the initial surface given by $\boldsymbol{x}_{i,0}$, and $v_{i,-I_i}^m$ and v_{i,O_i}^m represent the innermost and outermost vertices of column V_i^m. Each vertex $v_{i,k}^m$ describes a possible position of wall m in column V_i^m. An example depicting this graph column construction based on flow lines is shown in Figure 2.2(c).

The complete set of vertices of the graph is represented by the set of all column vertices and the vertices s and t. Unlike the vertices of a column V_i^m, s and t do not have an associated position in the image. Thus the complete set of vertices V is defined by:

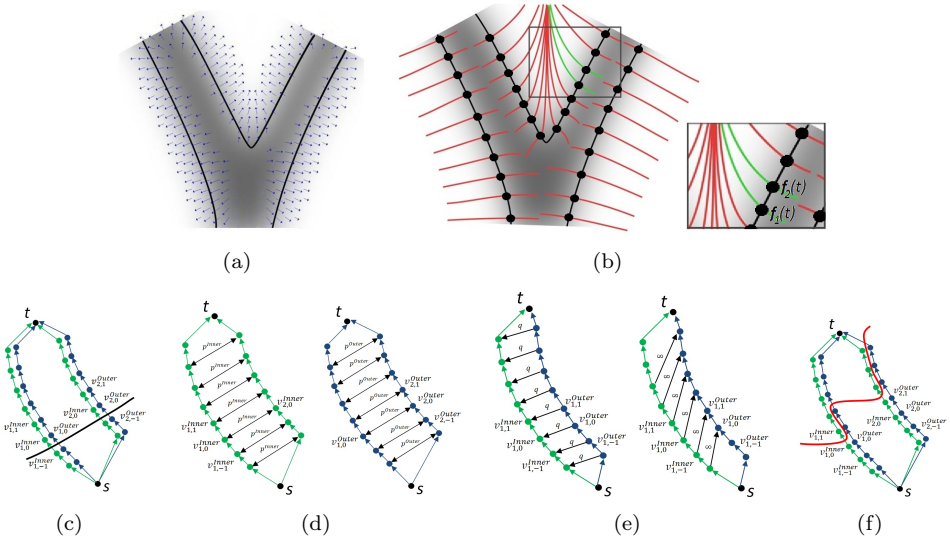

Figure 2.2. Construction of graph columns based on flow lines. First, the coarse initial segmentation is smoothed (gray colored tubular structure) and a gradient vector field is computed, see (a). Subsequently, (b) shows the flow lines represented by red lines which trace this gradient field both inwards and outwards from the initialization surface vertices represented by dots. These flow lines represent the graph columns trajectories. Two flow lines $\boldsymbol{f}_1(t)$ and $\boldsymbol{f}_2(t)$ indicated by the green curves are selected. In (c), each of these two flow lines represent two graph columns: inner (green dots) and outer (blue dots) wall columns. The graph column vertices are indicated by the dots. Here, some of the vertices labels are shown. The intra-column edges are depicted by arrows. The black dots s and t are the source and sink vertices respectively, and the initialization surface is represented by the black curve. Further, the smooth penalty edges are shown in (d) and the surface coupling edges in (e). Finally, a graph cut example represented by a red curve is depicted in (f).

$$V = \left\{ \bigcup_{i,m} V_i^m \right\} \cup \{s, t\}, \qquad (2.4)$$
$$s.t. \quad i \in \{0, .., N_Q\}, M = \{Inner, Outer\}\,.$$

Graph edges The set of edges E connects the vertices of the graph, and represents the association between vertices. The edge between the vertices $v_{i,k_1}^{m_1}$ and $v_{j,k_2}^{m_2}$ is denoted by $v_{i,k_1}^{m_1} \rightarrow v_{j,k_2}^{m_2}$ with an associated cost of $Cost(v_{i,k_1}^{m_1} \rightarrow v_{j,k_2}^{m_2})$.
The edge set E consists of intra-column edges E_{intra} and inter-column edges E_{inter} [5, 76].

- **Intra-column edges:** The intra-column edges E_{intra} connect two consecutive

vertices $v^m_{i,k}$ and $v^m_{i,k+1}$ in the same column by directed edges. The cost of edges $v^m_{i,k} \rightarrow v^m_{i,k+1}$ represents local image information associated with the border location, and must satisfy the condition $Cost(v^m_{i,k} \rightarrow v^m_{i,k+1}) \geq 0$ [76]. To ensure the surfaces cross each column only once, the edges $v^m_{i,k+1} \rightarrow v^m_{i,k}$ are assigned an infinite cost. Finally, the source vertex s is connected to all innermost vertices in the graph by $s \overset{\infty}{\rightarrow} v^m_{i,-I_i}$, and all outermost vertices are connected to the sink vertex t by $v^m_{i,O_i} \overset{Cost(v^m_{i,O_i} \rightarrow t)}{\rightarrow} t$. Note: $Cost(v^m_{i,O_i} \rightarrow t)$ is equivalent to $Cost(v^m_{i,O_i} \rightarrow v^m_{i,O_i+1})$, where t represents the nonexisting vertex v^m_{i,O_i+1}. A representation of the intra-column edges is shown in Figure 2.2(c).

The intra-column edge cost in column V^m_i should indicate the border location, and therefore the minimum should be at the position of surface m. We achieve a low cost $Cost(v^m_{i,k} \rightarrow v^m_{i,k+1})$ at the image border, by letting the cost be inversely proportional to the first order derivative of the image intensity $\frac{\partial \tilde{I}^{s_q}(\boldsymbol{f}_i(t))}{\partial t}$ along the graph column trajectory $\boldsymbol{f}_i$, where $\tilde{I}^{s_q}(\boldsymbol{f}_i(t))$ is a cubic interpolation of the MRI image sequence s_q: I^{s_q}: $\mathbb{Z}^3 \rightarrow \mathbb{R}$, at the position $\boldsymbol{f}_i(t)$. The MRI image intensity transitions from low to high from the lumen to the vessel wall, and usually from high to low intensity from the vessel wall to the background. Therefore only the positive part of $\frac{\partial \tilde{I}^{s_q}(\boldsymbol{f}_i(t))}{\partial t}$ is considered for $Cost(v^{Inner}_{i,k} \rightarrow v^{Inner}_{i,k+1})$, whereas for $Cost(v^{Outer}_{i,k} \rightarrow v^{Outer}_{i,k+1})$ only the negative part is considered.

Costs obtained from different spatially registered MR sequences are combined in a weighted sum, with the weights for inner and outer surfaces tuned separately. This approach may provide more accurate border locations since different image sequences have better contrast either at the inner or outer wall. Therefore, we define the intra-column cost by the equation:

$$Cost(v^m_{i,k} \rightarrow v^m_{i,k+1}) = K^m - \sum_{s_q \in S} \beta^{m,s_q} \left| \frac{\partial \tilde{I}^{s_q}(\boldsymbol{f}_i(k\delta))}{\partial t}^{Sign(m)} \right|, \tag{2.5}$$

with $Sign(m) = \begin{cases} + & if\ m = Inner \\ - & if\ m = Outer \end{cases}$, S represents the set of MRI image sequences, and $\beta^{m,s_q} \in [0,1]$ is a weighting parameter that indicates the contribution of each image sequence, such that $\sum_{s_q \in S} \beta^{m,s_q} = 1$. In Eq. 2.5, K^{Inner} and K^{Outer} represent respectively the most positive and most negative part of the weighted sum of the first order derivatives in the entire graph, such that $Cost(v^m_{i,k} \rightarrow v^m_{i,k+1}) \geq 0$. The derivatives in Eq. 2.5 are computed using central differences from the interpolated image intensity values along the flowlines.

- **Inter-column edges:** The edges between columns E_{inter} incorporate information from different graph columns. Using these, the wall position can be determined in graph columns in which the boundaries are not clearly visible. There are two types of edges: smooth penalty edges, and surface coupling edges.

Smooth penalty edges represented by $v_{i,k}^m \leftrightarrow v_{j,k}^m$ between the neighboring columns V_i^m and V_j^m, penalize irregularities, ensuring smooth segmentations. When the length of two neighboring columns is different, the remaining vertices at the innermost part of the column are connected to the source vertex s, and the remaining vertices at the outermost part of the column are connected to the sink t [76]. As in [5], we linearly penalize (Eq. 2.1) displacements of the graph cut between neighboring columns. To do this, the cost of these edges is given by a constant value p^m for each surface m: $v_{i,k}^m \overset{p^m}{\longleftrightarrow} v_{j,k}^m$. A representation of the smooth penalty edges is shown in Figure 2.2(d). Surface coupling edges are used to obtain topologically correct segmentations by constraining or penalizing the distance between the inner and outer walls. To ensure that the outer surface is outside the inner surface with a minimum distance of Δ vertices, we assign edges an infinite cost: $v_{i,k}^{Inner} \overset{\infty}{\rightarrow} v_{i,k+\Delta}^{Outer}$; and to linearly penalize the distance between the inner and outer wall, we assign the edges $v_{i,k}^{Inner} \overset{q}{\leftarrow} v_{i,k}^{Outer}$ with a constant cost value q. A representation of the surface coupling edges is shown in Figure 2.2(e).

2.3 Experiments and Results

2.3.1 Image Data

To validate the proposed method, we used MRI of the carotid bifurcation from 31 subjects with carotid artery plaques with at least one artery with a maximum wall thickness $\geq 2.5\,mm$ measured in ultrasound from the Rotterdam study [105]. Five arteries were excluded due to manual annotation errors. Therefore, 57 carotid arteries were used to evaluate the proposed method. We used both PDw-BBMRI and Phase Contrast MRI (PCMRI) images to compute the lumen centerline [94], which serves as initialization to construct the graph. In addition, we used PDw Echo Planar Imaging MRI (EPIMRI) and/or BBMRI images to compute the intra-column edge cost in Eq. 2.5. The acquisition time for each sequence is between $\sim$3 min and $\sim$6 min. EPIMRI images clearly distinguish the carotid artery wall [5], while in BBMRI the artery lumen is well defined [82]. In this study we compare segmentation results using either one of the two images (EPIMRI or BBMRI), and the combination of those. The BBMRI images have an in-plane voxel size of 0.507×0.507mm and 0.9mm slice thickness, while the PCMRI images have $0.703 \times 0.703 \times 1$mm, and the EPIMRI images $0.507 \times 0.507 \times 1.2$mm (see Van den Bouwhuijsen et al. [105] for details of the acquisition protocol).

2.3.2 Manual annotations

To evaluate and to optimize the parameters of the presented method, we used manual annotations in all BBMRI images. We used a similar manual annotation framework as described for CTA images in [46]. Here, the manual annotation process starts with a manual definition of the centerline. Subsequently, longitudinal contours along this centerline were drawn in a curved planar reformatted image for both the inner and outer border. These longitudinal contours were then used to create cross-sectional con-

tour images at 1mm intervals perpendicular to the centerline. Subsequently, all cross-sectional images were checked and contours were adjusted when needed. The resulting cross-sectional contour images were re-sampled at a resolution of 0.05×0.05mm, so ten times higher than the in-plane original image resolution, which permits validating the proposed method at a higher accuracy. Since the length of the automatic and manual centerlines may differ, cross-sections for which the automatic centerline is not defined are discarded from the evaluation.

For cases where it is not possible to evaluate the cross-sectional contours (Subsection 2.3.4 and 2.3.8), we compared 3D masks for the lumen and the complete vessel. These 3D masks were obtained by generating a 3D implicit function from the cross-sectional contours, which subsequently is filled to create the 3D masks [99]. The 3D masks of the lumen are obtained from the inner wall contours and the complete vessel 3D mask from the outer wall contours.

2.3.3 Preprocessing

The BBMRI and EPIMRI images suffer from intensity inhomogeneity within the neck area [45]. This was corrected using N4 bias field correction [100], which is one of the most popular methods to correct intensity nonuniformity in MRI data. We used the default parameters of the method on the complete image as described in [100].

To compute the lumen centerline for initialization we followed the same procedure as in [94]. First we registered PCMRI to BBMRI using 3D rigid transformation followed by a 3D affine transformation, with mutual information as similarity metric. Subsequently, three seed points were manually placed by an expert in the BBMRI images and the centerlines were computed using a cost obtained from BBMRI and PCMRI images as described in section 2.2.2.

The graph initializations were obtained by dilating the resulting centerlines using a disk structuring element with radius R of 2.5mm. The value of R was selected based on the average radius of the carotid artery which is between 2.3mm and 3.05mm depending on gender and section of the artery [56].

Subsequently, all EPI images were non-rigidly registered to the BBMRI data. We used the registration configuration presented in [111]. Here, a circular registration mask of 10mm diameter which covers the complete vessel was required. We obtained this by dilating the centerlines using a disk structuring element with a radius of 5mm. As suggested in [111], we used a 3D B-spline transformation with 15mm grid spacing, and mutual information as similarity metric.

Finally, we normalized the image intensities by a linear intensity normalization. For each image I^{s_q} with $s_q \in \{BBMRI, EPIMRI\}$, we computed the intensity values that accumulate 5%: $I^{s_q}_{5\%}$, and 95%: $I^{s_q}_{95\%}$ of the intensities distribution inside the same 10mm-diameter circular mask. Subsequently, these intensity values were scaled between 0 and 255 to obtain the normalized image $I^{s_q}_N$ by: $I^{s_q}_N(\mathbf{x}) = 255\frac{I^{s_q}(\mathbf{x}) - I^{s_q}_{5\%}}{I^{s_q}_{95\%} - I^{s_q}_{5\%}}$. These images are used to compute the intra-column cost defined in Eq. 2.5. A schematic of the preprocessing including the segmentation is shown in Figure 2.1.

2.3.4 Inter-observer variability

We compared manual annotations performed by two different experts with similar experience to assess inter-observer agreement. ICA and CCA were manually annotated by both observers in a subset of 28 carotid arteries. However, the generated cross-sectional contours for the two observers are at different positions due to differences in the manually annotated centerlines. Therefore, comparing the manually annotated cross-sections was not possible, and instead we generated 3D masks for the lumen and the complete vessel based on the cross-sectional contours of the inner and outer wall. To compare the 3D masks, we axially cropped the volumes such that the masks of both observers were defined on the same axial image slices in the cropped volume. We measured the volume overlap between observers by computing the Dice Similarity Coefficient (DSC) [31]. The obtained average DSC between observers was 0.81 ± 0.04 for the lumen and 0.91 ± 0.04 for the complete vessel. Figure 2.3 shows scatter plots describing the correlation of lumen and vessel wall (complete vessel segmentation minus lumen segmentation) volumes between the two observers. The obtained Intraclass Correlation Coefficient (ICC) for the lumen volumes was $ICC = 0.82$, and for the wall $ICC = 0.63$. We performed Friedman analysis, which is a non-parametric statistical test that allows comparing > 2 results at the same time. We found that the volumes from both observers were significantly different for the lumen and for the wall ($p < 0.01$) .

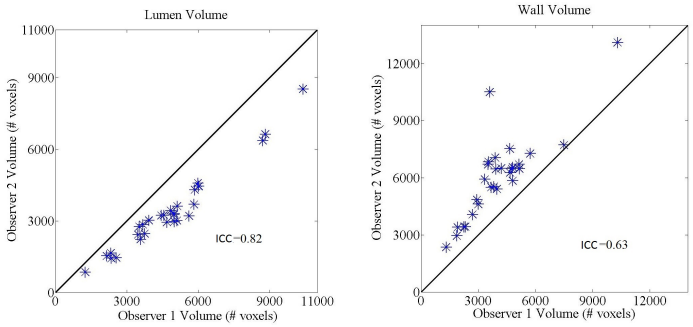

Figure 2.3. Scatter plots comparing observer 1 and observer 2 for segmented lumen volumes (a), and wall volumes (complete vessel minus lumen segmentation) (b), for 28 carotid arteries.

2.3.5 Parameter Tuning

Three-fold cross-validation experiments were performed in which the best set of parameters were determined on 20-21 images and subsequently used to segment the held out 10-11 images. This cross-validation allows evaluating the method on the complete data set, and the results represent performance on unseen data acquired with a similar scan protocol. To approximate the best set of parameters, we used an iterative

random binary search algorithm [76] to find the parameter set that maximizes the average vessel wall DSC between the automatically and manually segmented cross-sections from observer 1. Based on our previous work [5], we fixed the sampling interval of the flow lines δ described in section 2.2.3.2 to 0.35mm. The minimum distance between inner and outer borders in the graph Δ is fixed to two vertices: $\Delta = 2$, which represents a distance of 0.7mm (the minimum carotid wall thickness is about 0.8mm [89]). The parameters to optimize are then: the σ of the Gaussian kernel used to smooth the initial segmentation defined in section 2.2.3.1; the smoothness penalties p^{Inner}, p^{Outer}, the inner-outer border separation penalty q defined in section 2.2.3.2; and the weighting parameters in Eq. 2.4: $\beta^{Inner,BBMRI}$, $\beta^{Outer,BBMRI}$, $\beta^{Inner,EPIMRI}$, and $\beta^{Outer,EPIMRI}$. Since $\beta^{Inner,EPIMRI} = 1 - \beta^{Inner,BBMRI}$ and $\beta^{Outer,EPIMRI} = 1 - \beta^{Outer,BBMRI}$, we only need to optimize two weighting parameters: $\beta^{Inner,BBMRI}$ and $\beta^{Outer,BBMRI}$.

The average of the resulting best set of parameters for the three folds using each image sequence and combination are shown in Table 2.1. In general, low parameter variation was observed, however, higher variations were observed in the parameters of the combination method. In BBMRI, a high variation was observed in p^{Inner}. We observed that the best wall separation penalty q is zero in all cases. This indicates that it is preferred not to penalize the distance between borders to allow segmentations of thick vessel walls in the presence of plaque. When combining several image sequences, the contribution of the BBMRI image information was larger than EPIMRI for detecting both the inner and outer wall. As EPIMRI is registered to BBMRI, small alignment errors may occur causing the lower contribution of EPIMRI image information. However, EPIMRI contributed more to detecting the outer wall, which could be explained by the high outer border contrast in the EPIMRI images. We observed higher values for p^{Outer} than for p^{Inner}. As in our MR images the inner border contrast is better than the outer border contrast, more smoothing of the segmentation is required for the outer border, while for the inner border it is possible to rely more on the local derivative information.

Table 2.1. Determined best set of parameters using each image sequence and the combination. These were obtained applying a three-fold cross-validation and an iterative random binary search algorithm [76]. Remark: the values are the means obtained from the three folds, and between brackets the range is shown.

Image Sequence	**Best set of Parameters**					
	$\sigma(mm)$	p^{Inner}	p^{Outer}	q	$\beta^{Inner,BBMRI}$	$\beta^{Outer,BBMRI}$
BBMRI	2.25 [2 2.5]	66.3 [43.8 103.9]	573.3 [529.5 625]	0	1	1
EPIMRI	1.7 [1.5 2]	189.6 [127.7 257.8]	548.6 [412.9 700]	0	0	0
BBMRI & EPIMRI	1.63 [0.9 2]	107.81 [92.5 121.87]	387.47 [98.7 550]	0	0.91 [0.75 1]	0.58 [0 0.93]

2.3.6 Comparison with manual annotations

Based on the best set of parameters determined in two of the folds, we applied the proposed segmentation method in the held out folds. Figure 2.4 shows cross-sectional

segmentation results using the proposed method combining BBMRI and EPIMRI. Further, Figure 2.5 shows a 3D mask obtained from the manual annotations and the corresponding 3D segmentation result.

Table 2.2 shows the mean DSC between the automatic and manually annotated cross-sections from observer 1 for inner DSC^{Inner} and outer vessel borders DSC^{Outer} for the 57 carotid arteries. Additionally, the signed and absolute wall thickness differences (manual minus automatic) are shown in the table. To measure the wall thickness in the automatic and manual segmentations, we measured the mean distance between the inner border and the outer border over all points for each segmented cross-section. The distance for each point is measured along a ray from the centerline position and is given by the length of the segment stretching from inner border to outer border. We performed Friedman analysis and subsequently a post-hoc analysis based on Tukey-Kramer testing for multiple comparisons to determine which of the differences were significant. The highest average DSC for the inner border was obtained by combining BBMRI and EPIMRI image sequences, and this was significantly higher ($p = 0.01$) than for using only EPIMRI, but not significantly higher than for using only BBMRI. For the outer border the highest DSC was obtained using BBMRI only, which was significantly higher than using EPIMRI alone ($p = 0.04$). Thus, for both inner and outer wall segmentation no significant differences were observed between using both sequences and using only BBMRI. The mean wall thickness differences for the three options were very close, and no significant differences were observed. In all three cases a slight over-segmentation of the wall with respect to manual annotations of less than the voxel size was observed.

To evaluate how the method performs in the presence of disease represented as a wall thickening; we evaluated the inner and outer DSC of all manual and automatic cross-sections as a function of the wall thickness. The wall thickness per cross-section was measured as the 90% percentile distance between inner border points to the outer border (we do not use the maximum wall thickness as this is more sensitive to noise in the measures). The DSC for increasing wall thickness is shown in Figure 2.6. From the figure we see that similar results were obtained for BBMRI and the combination of BBMRI and EPIMRI. For these two options the results are very robust to thickening of the wall, both for the inner and outer wall. In the remainder of this section, all results reported are for the method combining BBMRI and EPIMRI images.

Table 2.2. DSC overlap for inner border (DSC^{Inner}) and outer border (DSC^{Outer}), and Signed and absolute Wall Thickness Differences (SWTD, AWTD) between the automatic and manual annotated cross-sections for each image sequence combination († shows that those results were significantly different to EPIMRI).

	BBMRI	EPIMRI	BBMRI & EPIMRI
DSC^{Inner}	0.88 ± 0.06	0.88 ± 0.03	$0.89 \pm 0.05^{\dagger}$
DSC^{Outer}	$0.86 \pm 0.06^{\dagger}$	0.85 ± 0.05	0.85 ± 0.06
SWTD (mm)	-0.15 ± 0.3	-0.19 ± 0.4	-0.22 ± 0.4
AWTD (mm)	0.26 ± 0.2	0.34 ± 0.3	0.37 ± 0.2

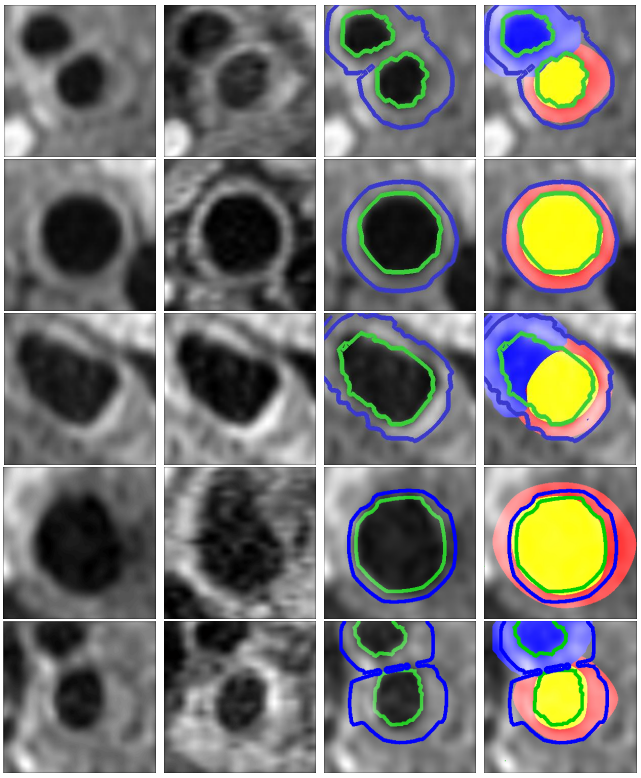

Figure 2.4. Cross-sectional segmentation results using the proposed method combining BBMRI and EPIMRI image sequences. The BBMRI images are shown in the first column, and the EPIMRI image in the second column. The automatic segmentations are depicted by green (inner wall) and blue (outer wall) contours in the third column. The manual annotations are shown by the yellow surface (lumen) and the red surface (vessel wall) in the fourth column, with automatic segmentation results overlaid. The blue areas are excluded from evaluation, as the manual annotation described only part of the cross-section in the bifurcations.

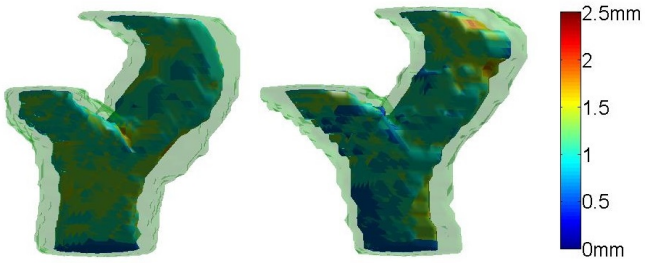

Figure 2.5. Obtained 3D manual annotation (left) and automatic segmentation result (right) for the same carotid artery. The transparent green layer depicts the outer vessel border. The colors in the inner wall represent the wall thickness (mm).

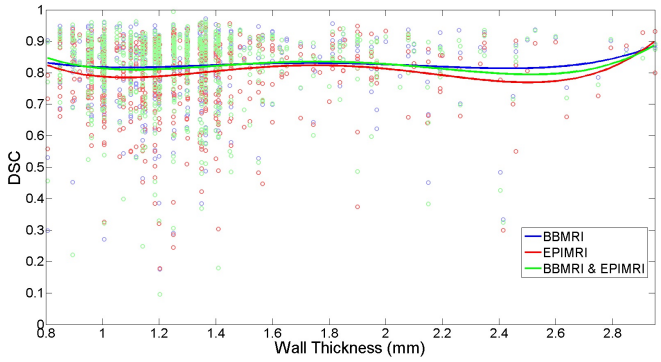

(a) DSC^{Inner}

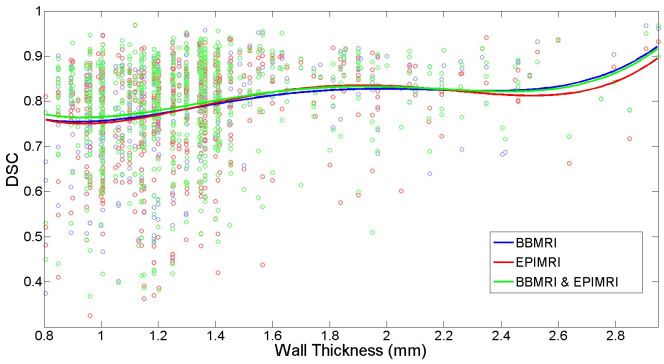

(b) DSC^{Outer}

Figure 2.6. DSC as a function of maximum wall thickness for each image sequence and their combination, for all cross-sections. The wall thickness is represented by the 90% percentile thickness in the manually segmented cross-section. Finally, polynomial curves that fit the points for each of the sequence combinations are shown in the figures.

Scatter plots of the volumes for automated segmentations against the manual annotations from observer 1, as measured in the upsampled cross-sectional slices, are given in Figure 2.7 for lumen and vessel wall. We found an excellent correlation $ICC = 0.99$ between lumen volumes and a good correlation $ICC = 0.72$ between wall volumes.

Finally, we compared the results of the proposed method to the manual segmentations from the second observer. As the second observer segmented only ICA and CCA, the ECA sections of the segmentations by the proposed method and by observer 1 were excluded. Using the manual ECA segmentations of observer 1, we created the exclusion area by creating a 3D mask of this manually annotated ECA section, and applied an axial dilation with a disk structuring element of 3mm radius to guarantee the exclusion of the automatically segmented ECA. Subsequently, we cropped the segmented volumes such that all segmentations were defined in all axial slices. Finally, we computed DSC outside the excluded area. The results for the subset of 28 carotid arteries that were manually annotated by both observers are described in Table 2.3.

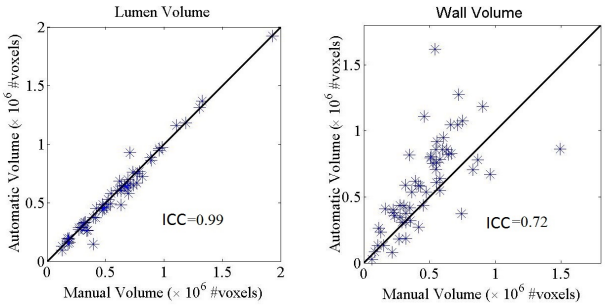

(a) (b)

Figure 2.7. Scatter plots comparing manual and the automatic segmented lumen volumes (a), and wall volumes (complete vessel-lumen segmentation) (b) using the proposed segmentation method combining BBMRI and EPIMRI image sequences.

The overlap of the automatic lumen segmentations and the segmentations of observer 1, was significantly higher ($p < 0.001$) than the overlap between observer 1 and observer 2, and the overlap between observer 2 and the automatic segmentations. For the outer border, the overlap between observer 1 and observer 2 was significantly higher than the overlap between observer 1 and the automatic segmentation, and between observer 2 and the automatic segmentation. From the SWTD results, we observed an over-segmentation of the wall with respect to observer 1 and an under-segmentation with respect to observer 2. Based on the AWTD, agreement of wall thickness measures was better between the automated approach and both observers than between observers.

Table 2.3. Agreement between the automatic method, observer 1 (Obs. 1) and observer 2 (Obs. 2). ^{1}, ^{2} and ^{3} indicate that the obtained result is significantly better than the corresponding results in row 1, 2 or 3, respectively. For the automatic segmentations, we combined BBMRI and EPIMRI. The ECA has been excluded for this analysis, so values are different from Table 2.2.

	DSC^{Inner}	DSC^{Outer}	SWTD (mm)	AWTD (mm)
Obs. 1 Vs. Obs. 2	0.81 ± 0.04	$0.91 \pm 0.04^{2,3}$	-0.62 ± 0.25	0.62 ± 0.25
Obs. 1 Vs. Auto	$0.88 \pm 0.06^{1,3}$	0.83 ± 0.06	-0.27 ± 0.4^{3}	0.41 ± 0.24^{1}
Obs. 2 Vs. Auto	0.78 ± 0.04	0.84 ± 0.08	0.34 ± 0.4	0.39 ± 0.4^{1}

2.3.7 Reproducibility analysis

Scan-rescan reproducibility was assessed on 30 patients who were imaged twice within a short time interval (15 ± 9 days). Significant changes in carotid anatomy were

therefore not expected, and lumen and wall volume must be similar. The proposed method, combining BBMRI and EPIMRI images using the average set of parameters as described in Table 2.2, was applied to the baseline and follow-up images of 60 carotid arteries. All segmented volumes were cropped from 13.5mm below up to 9mm above a manually allocated carotid bifurcation point in order to compare similar regions on baseline and follow-up. Scatter plots describing the correlations for lumen and vessel wall volumes between baseline and follow-up are shown in Figures 2.8(a) and 2.8(b). The obtained intraclass correlation for the lumen volumes is $ICC = 0.96$, and for the wall $ICC = 0.74$. The mean absolute wall volume difference between scan-rescan was $23\% \pm 23\%$. Figures 2.8(c) and 2.8(d) show an example of a baseline and follow-up segmentation pair.

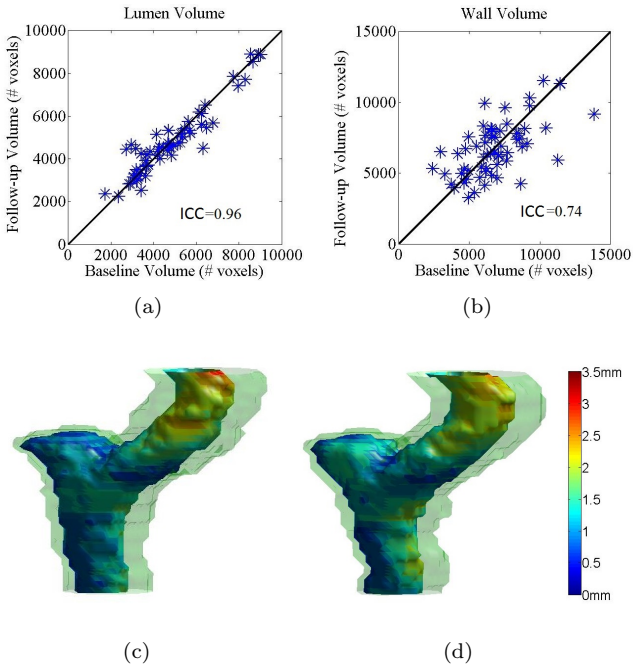

Figure 2.8. Comparison of baseline and short-term follow-up segmentations. (a) and (b) depict scatter plots comparing baseline and follow-up segmented lumen volumes (a), and wall volumes (b). The scatter plots show the results for 60 carotid arteries. In (c) a segmented baseline is shown, and (d) shows the corresponding segmented follow-up.

2.3.8 Comparison with Other methods

Finally, we compared the proposed method to another carotid artery wall segmentation method in MRI on a public data set. Hameeteman et al. [45] proposed a cylindrical deformable surface model with a learning-based postprocessing step to segment the carotid artery wall in MRI. We choose this method because these results

were made publicly available at http://ergocar.bigr.nl. In addition, to date their reported results are among the best for carotid artery wall segmentation in MRI. As only ICA and CCA were segmented using the method presented in [45] the segmented ECA sections were excluded from our resulting segmentations as described in section 2.3.6. Subsequently, we cropped the segmented volumes 25mm centered at the bifurcation point as described in [45]. Fourteen subjects were used for the evaluation. From the 28 carotid arteries, one was discarded due to manual annotation errors and four others because we observed big displacements on the ECA sections between automatic and manual segmentations and it was not possible to exclude the ECA using the method described in section 2.3.6. Table 2.4 shows the DSC on the manually annotated volumes from observer 1 for inner and outer border using both methods in 23 arteries. For the inner border, the presented method was significantly better ($p < 0.01$), while for the outer border it was not significantly different ($p = 0.06$). In addition, Table 2.4 shows the SWTD and AWTD (manual-automatic) for both methods, here we observed lower SWTD and significantly lower AWTD using the method proposed by Hameeteman et al. [45] ($p < 0.01$).

Table 2.4. Comparison of the proposed method to the method proposed by Hameeteman et al. [45] using DSC for inner (DSC^{Inner}) and outer border (DSC^{Outer}) between automatic results and 3D manual annotations, and signed and absolute wall thickness differences (SWTD, AWTD) between automatic and manual annotated cross-sections († shows that those results were significantly better than the other method).

	Hameeteman et al. [45]	Proposed Method
DSC^{Inner}	0.87 ± 0.09	$0.91 \pm 0.04^{\dagger}$
DSC^{Outer}	0.88 ± 0.08	0.86 ± 0.05
SWTD (mm)	-0.02 ± 0.24	-0.14 ± 0.54
AWTD (mm)	$0.20 \pm 0.15^{\dagger}$	0.46 ± 0.30

2.4 Discussion

In this chapter, we presented a new 3D method for carotid artery wall segmentation in MRI. This finds a globally optimal solution based on a cost function and jointly segments the complete lumen and outer wall including the bifurcation section. The method requires an initialization to build the graph. However, as the graph column trajectories extend both inwards and outwards from this initialization, a coarse approximation of the lumen is sufficient.

We evaluated the quality of the automatic segmentations by cross-validation and comparison with manual segmentations performed by two experts. We also evaluated the method using several image combinations (BBMRI, EPIMRI, and BBMRI & EPIMRI). Based on the cross-validation, we did not observe big DSC variances using different parameter settings as shown in Table 2.2. This means that the methods are able to generalize to unseen data acquired with a similar scan protocol. However,

to apply the method to data acquired with a different scan protocol, the method parameters need to be re-tuned, as is the case for most segmentation approaches. The results for all combinations were good, with lumen overlap $DSC^{Inner} > 0.88$ and complete vessel overlap $DSC^{Outer} > 0.85$, and absolute wall thickness differences $AWTD < 0.37mm$, less than the in-plane voxel size. Segmentations based on EPIMRI had the lowest accuracy. This can be partly explained by the fact that the manual annotations were performed in BBMRI. Therefore possible misregistrations of EPIMRI to BBMRI are measured as segmentation errors in EPIMRI, and in cases where low image contrast or artefacts in BBMRI lead to a certain annotation, this is more likely to be reproduced by an automatic segmentation using BBMRI than by one using EPIMRI. Similar results with no significant differences were observed between BBMRI and the combination of BBMRI and EPIMRI. This similarity was also observed in the relation with wall thickness, where both methods had similar good performances in healthy and diseased sections of the artery. We conclude that the proposed edge cost function that can integrate information from several images will give better or similar results than using only one image. In cases where the available images only have good contrast in one of the borders to segment, such combined cost function can be beneficial. However, as BBMRI itself has a good inner and a fair outer wall contrast, combining BBMRI with EPIMRI did not make a difference in our experiments.

The segmentation errors we obtained for the artery lumen are comparable to the inter-observer variation. As can be seen in Figure 2.3(a), Observer 2 showed a strong, consistent undersegmentation of the lumen with respect to Observer 1, which resulted in a relatively low agreement of this observer with both the automated method and Observer 1. This underlines the importance of objective measurements, such as those obtained automatically in this chapter, in the analysis of carotid MR images. For the outer border, the overlap with the manual annotations of both observers was significantly lower than between observers. This lower accuracy at the outer border was also visible in the reproducibility study in the scatter plots in Figure 2.8(b) where the variation in wall volume measured in repeated scans is larger than the variation in lumen volume. Even though the correlation for the wall volumes is lower, we believe the proposed method presents a good reproducibility for lumen and wall volumes, as these correlations were higher compared to the inter-observer volume correlations. This is an important result: if we can measure similar volumes for the scan-rescan images, we should be able to do volume tracking for longitudinal analysis in clinical intervals. One possible reason for the lower performance at the outer border could be that the outer border contrast is often lower. The proposed cost function based on intensity image derivatives may therefore fail. In such cases, a cost function that integrates more features in addition to image intensity derivatives might give a better representation of the location of the outer border.

We compared the proposed method to the method presented in [45], which is an improved version of [110]. In [45], they reported statistically better results than those obtained using van t Klooster et al. [110] ($DSC^{Inner} = 0.83$ and outer border $DSC^{Outer} = 0.85$). In this chapter, the comparisons were performed on CCA and ICA only, because the method presented in [45] cannot segment the complete bifurcation. We obtained better DSC^{Inner} and the method presented in [45] resulted

in lower wall thickness differences. Despite the similarity of the results, we consider our method relevant for this application as it can segment the complete bifurcation, which is medically relevant using a single graph cut segmentation. On the other hand, methods such as [45], which search a single tubular shape, could be used to segment the entire bifurcation by segmenting the individual vessel segments separately and joining the resulting segmentations. However, this may result in errors in the bifurcation region where the model of a single tube shape is not appropriate. Methods to segment only the lumen such as [94] reported a $DSC^{Inner} = 0.89$, which is similar to the reported DSC^{Inner} for the proposed method. Further, Ukwatta et al. [103] reported an average inner border $DSC^{Inner} > 0.85$ and outer border $DSC^{Outer} > 0.87$ using similar images. These results are comparable to the results obtained by our method, however, results cannot be compared directly as the data used for validation is different. Advantages of the proposed method are that it requires less user interaction than the method presented by Ukwatta et al. [103] therefore it is easier to fully automate using automated seed point detection or lumen detection methods as in [64], and that it can segment the complete bifurcation in one global optimization in contrast to Hameeteman et al. [45] and van t Klooster et al. [110].
Because of the good quality inner border segmentations, the presented method can be used in clinical practice for lumen stenosis detection, or to analyze abnormalities in the carotid artery geometry. Additionally, the method can be used to analyze the vessel wall in large population studies. For wall analysis in clinical practice, an interactive approach that would allow more accurate quantitative wall measurements may be desirable.

2.5 Conclusion

To conclude, we have presented an optimal surface graph-based method for segmenting the complete carotid artery wall, which requires minimal user interaction and can combine information from several images. The method shows good agreement with manual segmentations. In contrast to previous approaches, our method jointly optimizes both surfaces: inner and outer border, finds a globally optimal solution, and can reliably segment the bifurcation section which is the most clinically relevant area to assess.

Chapter Three

Maximization of Regional probabilities using Graphs: Application to Carotid Artery Segmentation in MRI

Abstract — We present a segmentation method that maximizes regional probabilities enclosed by coupled surfaces using an Optimal Surface Graph (OSG) cut approach. This OSG cut determines the globally optimal solution given a graph constructed around an initial surface. We applied this to automatically segment the vessel wall of the carotid artery in magnetic resonance images. First, voxel-wise regional probability maps were obtained using a Support Vector Machine classifier trained on local image features. While most methods for vessel wall segmentation only use edge information, we show that maximizing regional probabilities using an OSG improves the segmentation results. The method was evaluated on 49 carotid arteries from 30 subjects. The proposed method shows good accuracy with a Dice wall overlap of $74.1\% \pm 4.3\%$, and significantly outperforms another published method using only edge information, the obtained segmentations using voxel-wise classification alone, and another published artery wall segmentation method based on a deformable surface model. Intra-class correlations (ICC) with manually measured lumen and wall volumes were similar to those obtained between observers. Finally, we show a good reproducibility of the method with $ICC = 0.86$ between the volumes measured in scans repeated within a short time interval.

Based upon: Andrs M. Arias-Lorza, Arna van Engelen, Jens Petersen, Aad van der Lugt, and Marleen de Bruijne, "Maximization of Regional probabilities using Graphs: Application to Carotid Artery Segmentation in MRI", *submitted*.

3.1 Introduction

Multi-region coupled surface segmentation is an important topic as several applications are represented by coupled surfaces, such as vessel wall segmentation, intraretinal layers detection, and pulmonary airway wall segmentation. In the specific case of the carotid artery vessel wall, its segmentation is required to make a proper analysis of potential presence and severity of atherosclerotic plaques. Such analysis is important as plaques may rupture resulting in a stroke [90]. Wall segmentation of the carotid artery is possible in MRI, however, manual segmentation is time consuming and subject to inter-observer variability [46].

Several methods to automatically segment the carotid artery vessel wall in MRI have been proposed in the literature [6,45,103,110]. In most of these methods, the segmentation is obtained by performing a minimization of a cost function which generally integrates features and geometric vascular models and incorporates smoothness and topological constraints in the segmentation solution. However, lack of proper features, erroneous models, and an inaccurate cost function or optimizer may lead to segmentation errors. All these methods use a limited set of features: image intensity derivatives [6, 45, 110], or intensity Probability Density Function (PDF) [103]. However, these features are not sufficient to describe the artery wall adequately in all possible cases. Further, optimizers such as the one used by [110] and [45] may get stuck at a local minimum of the cost function. Therefore, a more descriptive set of features and an optimizer that guarantees a global optimum of a cost function based on those features would be desirable.

Promising results have been obtained using graph-based optimicization methods in different applications [6,11,36,76,120]. Graph-based methods allow to obtain a global minimization of a cost function with low processing times [17]. This cost function is represented in the graph, and the minimization is performed by a graph-cut approach. However, formulating meaningful cost functions represented by the graph can be a challenging problem.

A class of graph-based segmentation methods commonly called Optimal Surface Graph (OSG) is especially interesting. Here the graph is built based on an initial shape, allowing an easy integration of prior shape information in the cost function [118]. Previously in Chapter 2, we presented a method to segment the carotid artery vessel wall in MRI using an OSG model [6]. The cost function used edge features, based on directional image derivatives, over the inner and outer vessel wall, integrating smoothness and topology constraints. Generally good results were observed, however, segmentation errors may arise as the carotid vessel wall in MRI can have low contrast with the background and/or show high intensity variation, especially in plaque regions, as depicted in figure 3.1(a). In such cases the edges are not clearly visible and are therefore more difficult to detect using image derivatives as shown in figures 3.1(b) (inner border) and 3.1(c) (outer border). In these cases, edge information is not sufficient to obtain good segmentation results, and incorporating information from the regions bounded by the sought surfaces may help to obtain better segmentation. To do this, the segmentation problem has to be reformulated to identify the different bounded regions, instead of finding the surfaces.

Multi-region segmentation methods combining global optimization techniques with

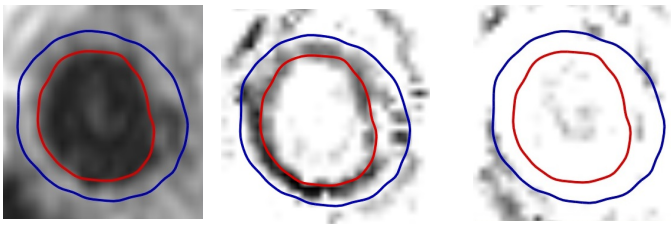

(a) (b) (c)

Figure 3.1. Example of an MRI image of the carotid artery (a) and the local edge information features based on directional image derivatives for the inner vessel wall border (b) and the outer border (c) as described in Chapter 2. Manual annotations for inner and outer border are represented by the red and blue contours respectively.

regional information have been used before [30, 44, 103, 119]. Ukwatta et al. [103] introduced a global optimization contour evolution method based on matching intensity PDFs of the carotid artery wall in MRI. A convex relaxation of a cost based on this PDFs is minimized using a continuous max-flow model. This is an interesting approach as it can optimize the cost without a graph, thus avoiding metrication errors. However, as this approach requires an initial estimation of the PDFs, errors may arise in case of inaccuracies in this estimation. Better results may be obtained if more regional features are used besides intensity, and if an explicit shape prior is integrated in the model. The use of graph models together with regional information has become popular in image segmentation. For instance, Delong and Boykov [30] proposed a voxel-wise graph model which incorporates the spatial distribution of colors within an object to segment multiple enclosed region structures. In contrast, OSG which opposed to voxel-wise graph models are built based on an initial shape. This may be beneficial to segment structures with complex geometry. Wu et al. [119] and Haeker et al. [44] used a similar global OSG model [61]. The OSG model presented in [61] unfold the image using an initialization, transforming the problem to a terrain-like surface segmentation. However, this unfolding process is not clear for more complex shapes such as a bifurcating artery and may lead to errors in regions with high curvature. In these cases, OSG models such as [6, 76] which construct the graph based on smooth flow lines are more suitable. In [61] the optimization problem is formulated such that they find a closed set of vertices with the minimum cost, by transforming the graph G into a new graph G_{st}. Wu et al. [119] used this graph model to minimize the intraclass intensity variance, while Haeker et al. [44] used it to maximize the regional probabilities within a region.

In this chapter we adapted the coupled OSG model presented in Chapter 2 to perform multi-region segmentation by incorporating regional information in the graph to improve the overall segmentation results. We apply this method to segment the carotid artery wall in MRI. We follow a similar approach to incorporate the regional information as in [44]. The regional information is included in the graph as edge costs, and this cost is defined such that after the graph cut, the enclosed sum of regional probabilities is maximized considering smoothness and topological constraints.

However, we cannot directly apply the edge cost presented by [44] to get the desired maximization, as these graph models [61] are different to the OSG graph structure model we use [52]. While they search for the minimum-cost closed set of vertices in a graph G by transforming G to a graph G_{st} as mentioned above, we do not apply this transformation and we specify the problem directly in terms of minimum cost surfaces. Therefore, we reformulated the cost function defined in [44] that could be applied in a graph model as [52]. We represent the regional information as Regional Probability Maps (RPMs) obtained using a support vector machine classifier. These RPMs allow incorporation of a large number of image features, which results in a better representation of the regions and more robust segmentation results.

3.2 Method

3.2.1 Optimal Surface Graph Method

OSG methods as proposed by [118] allow optimal multiple surface segmentation solutions incorporating topology constraints and shape prior information. In the OSG methods the optimization is defined as the minimization of a cost function represented as the sum of graph edge costs, and the minimization is computed using a minimum cut algorithm. The graph $G = (V, E)$ is composed of vertices V and edges E. V is composed of the vertices associated with positions in the image, and the vertices s and t which denote the source and sink points of the graph. The edges E connect the vertices of the graph, and represent the association between vertices. Therefore, to obtain meaningful segmentations, costly edges are expected to connect vertices from the same region, whereas low-cost edges are expected to connect vertices from different regions. The segmentation solution is defined by the minimum cut that separates the graph in two parts: source part $V_s \subseteq V$ and sink part $V_t \subseteq V$, such that $V_t = V \backslash V_s, s \in V_s, t \in V_t$. Given the edge cost $\omega : E \to \mathbb{R}$, the minimum cut minimizes the total cost of the edges that are being cut represented by $\min_{(v_i \in V_s,\ v_j \in V_t)} \sum \omega(v_i \to v_j)$ [52]. For multiple surface segmentation, all surfaces are segmented simultaneously using a single minimum cut. Each surface is thus represented by a subgraph and the individual surface subgraphs are coupled using surface coupling edges between vertices of each subgraph. This coupling also allows to incorporate topological constraints in the segmentation solution [6, 76].

We follow a similar graph construction approach as presented in Chapter 2 to segment the carotid artery wall on MRI. In Chapter 2, the graph is constructed starting from a coarse initial segmentation of the innermost surface, and the vertices are grouped by smooth non-intersecting graph columns tracing inwards and outwards from this initial segmentation. Non-intersecting graph columns are guaranteed if these are defined on the trajectory of flow lines of the Gaussian smoothed initial segmentation. Given the flow lines $\boldsymbol{f}_i$: $\mathbb{Z} \to \mathbb{R}^3$ where $i \in \{1, ..., N\}$ with N the number of voxels on the initial segmentation surface, the graph vertex $v_{i,k}^m \in V$ is associated with the image position $\boldsymbol{f}_i(k)$ and a possible position of surface $m \in \{1, ..., M\}$, where M is the maximum number of coupled surfaces to segment. The graph columns are defined by the set of vertices $V_i^m = \{v_{i,k}^m | k \subset \mathbb{Z},\ I_i, O_i \in \mathbb{Z},\ k = -I_i, -I_i + 1, \ldots, O_i - 1\ , O_i\}$ where the

uniform separation distance between vertices is given by $\delta = \|\boldsymbol{f}_i(k+1) - \boldsymbol{f}_i(k)\|$. Here $v^m_{i,-I_i}$ and v^m_{i,O_i} represent the innermost and outermost vertices of column V^m_i. Several edges are defined in the graph [6]: 1) the edges $v^m_{i,k} \rightarrow v^m_{i,k+1}$ in the same graph column indicate the relation between inside and outside of surface m such that $\omega(v^m_{i,k} \rightarrow v^m_{i,k+1})$ should be a minimum at the position of the surface; 2) the smoothing penalty edges between neighboring graph columns given by $v^m_{i,k} \overset{p^m}{\longleftrightarrow} v^m_{j,k}$; 3) topological constraint edges in the same graph columns $v^m_{i,k+1} \overset{\infty}{\rightarrow} v^m_{i,k}$; and finally the graph coupling edges $v^m_{i,k} \overset{\infty}{\rightarrow} v^{m+1}_{i,k+\Delta}$ to guarantee that surface $m+1$ is outside surface m with a minimum distance of Δ vertices in between; 4) finally, the source vertex s is connected to all innermost vertices, and the sink vertex t to all outermost vertices.
In Chapter 2, to get a minimum of $\omega(v^m_{i,k} \rightarrow v^m_{i,k+1})$ at the position of surface m, the method favors positions with high image gradient, such that ω is inversely proportional to the positive or negative part of the first order derivative of the image intensity $I : \mathbb{R}^3 \rightarrow \mathbb{R}$ along the graph column trajectory $\boldsymbol{f}_i$. This is defined by: $\omega(v^m_{i,k} \rightarrow v^m_{i,k+1}) \propto |(\frac{\partial I(\boldsymbol{f}_i(k))}{\partial k})^{\{+,-\}}|^{-1}$, where $I(\boldsymbol{f}_i(k))$ is the image intensity at the position $\boldsymbol{f}_i(k)$. An example of these edge cost mapped in the image space are depicted in Figure 3.1.

3.2.2 Regional Information and OSG

Ideally, the cost functions as described in Chapter 2 would yield low costs at the surface positions. However, in the carotid vessel wall in MRI, the plaque sections and surrounding structures of the vessel are highly variable in intensities, which leads to poor contrast at the border or may even cause other structures to have stronger edges and therefore lower costs than the true vessel borders, as shown in Figure 3.1. Although cost errors in individual graph columns may be corrected thanks to the smoothing penalty edges and the coupling edges during the global graph minimization, inaccuracies in the final segmentation may still arise.
In these cases where the vessel border is not clearly visible in the image, edge information is not sufficient to get good segmentation results, and better segmentations are expected by using regional information that integrates several features. Let the probability that an image position belongs to region R_m be defined by $P_{R_m} : \mathbb{R}^3 \rightarrow [0,1]$. The segmentation problem can be defined as the separation of regions that maximizes the total sum of regional probabilities. Following [44], $R = \bigcup_{m=0,..M} R_m$ is the region to segment, where $R_0, \ldots, R_m$ are enclosed by the surface $m+1$, and there is no overlap between regions, so $R_a \cap R_b = \emptyset$ for $a \neq b$ and $a, b \in \{0, ..., M\}$, then the optimal segmentation solution is represented by the separation of the regions $R_0, \ldots, R_M$ that maximizes the total sum of regional probabilities, that is:

$$\underset{R_0,\ldots,R_M}{\arg\max} \left(\sum_{m=0}^{M} \left(\sum_{\boldsymbol{x} \in R_m} P_{R_m}(\boldsymbol{x}) \right) \right). \tag{3.1}$$

As in [44], Eq. 3.1 is modified to get a separate expression for each of the enclosed regions so this can be solved using a graph cut. As the sum of all probabilities in R is a constant: $\sum_{\boldsymbol{x} \in R} P_{R_m}(\boldsymbol{x}) = Constant$, and the set of regions that maximizes Eq.

3.1 is not changed by adding constant values, Eq. 3.1 is reformulated as:

$$\underset{R_0,\ldots,R_M}{\arg\max} \left(\sum_{m=0}^{M} \left(\sum_{\boldsymbol{x} \in R_m} P_{R_m}(\boldsymbol{x}) \right) + \sum_{m=1}^{M-1} \left(\sum_{\boldsymbol{x} \in R} P_{R_m}(\boldsymbol{x}) \right) \right). \tag{3.2}$$

After expanding and reorganizing Eq. 3.2, we obtain:

$$\underset{R_0,\ldots,R_M}{\arg\max} \left(\sum_{m=0}^{M-1} \left(\sum_{\boldsymbol{x} \in \{R_0,..,R_m\}} P_{R_m}(\boldsymbol{x}) \; + \sum_{\boldsymbol{x} \in \{R_{m+1},..,R_M\}} P_{R_{m+1}}(\boldsymbol{x}) \right) \right). \tag{3.3}$$

Eq. 3.3 defines a maximization based on a sum for each of the enclosed regions in the surfaces. We have to reformulate this equation so it can be solved using a minimum cut in our graph structure. As R can also be represented by the union of the vertex positions in the graph columns, we have that $R = \bigcup_{i=1,..N} \boldsymbol{f}_i$. Therefore, replacing each position $\boldsymbol{x} \in R$ by the position in the graph column $\boldsymbol{f}_i$, we can further expand Eq. 3.3 to:

$$\underset{R_0,\ldots,R_M}{\arg\max} \left(\sum_{m=0}^{M-1} \sum_{i=1}^{N} \left(\sum_{\substack{\boldsymbol{f}_i(k_1) \in R_0,..,R_m \\ k_1 \in -I_i,\ldots,O_i}} P_{R_m}(\boldsymbol{f}_i(k_1)) \; + \sum_{\substack{\boldsymbol{f}_i(k_2) \in R_{m+1},..,R_M \\ k_2 \in -I_i,\ldots,O_i}} P_{R_{m+1}}(\boldsymbol{f}_i(k_2)) \right) \right). \tag{3.4}$$

As the graph columns progressively cross each region from R_0 to R_M, for each graph column there is a vertex position $\boldsymbol{f}_i(k_{i,m})$ given $k_{i,m} \in \{-I_i, -I_i+1, \ldots, O_i-1, O_i\}$ located at the outer surface of R_m that satisfies that all vertices in the column below and including it are inside the enclosed regions by this surface, that is: $\{\boldsymbol{f}_i(-I_i), \boldsymbol{f}_i(-I_i+1), ..., \boldsymbol{f}_i(k_{i,m})\} \in \{R_0,..,R_m\}$ and $\{\boldsymbol{f}_i(k_{i,m}+1), ..., \boldsymbol{f}_i(O_i)\} \in \{R_{m+1},..,R_M\}$. Finally, we transform Eq. 3.4 from maximization into a minimization that can be solved by computing a minimum graph cut, by introducing the arbitrary constant K. Therefore, we can reformulate Eq. 3.4 to search for these vertex positions instead of the regions:

$$\underset{k_{i,m}}{\arg\min} \left(\sum_{m=0}^{M-1} \sum_{i=1}^{N} \left(K - \left(\sum_{k_1=-I_i}^{k_{i,m}} P_{R_m}(\boldsymbol{f}_i(k_1)) \; + \sum_{k_2=k_{i,m}+1}^{O_i} P_{R_{m+1}}(\boldsymbol{f}_i(k_2)) \right) \right) \right), \tag{3.5}$$

Eq. 3.5 can now be solved using a minimum cut. Given that each graph column is cut only once, we can define $\omega(v^m_{i,k} \rightarrow v^m_{i,k+1})$ as:

$$\omega(v^m_{i,k} \rightarrow v^m_{i,k+1}) = K - \left(\sum_{n=-I_i}^{k} P_{R_m}(\boldsymbol{f}_i(n)) \; + \sum_{l=k+1}^{O_i} P_{R_{m+1}}(\boldsymbol{f}_i(l)) \right). \tag{3.6}$$

Therefore obtaining a minimum cut using the edge costs defined by Eq. 3.6 guarantees an optimal separation of the regions as defined in Eq. 3.1.

3.2.3 Regional Probability Maps

We represent the regional information as a regional probability map (RPM). Accurate RPMs that make use of a large set of image features can be obtained using voxel classification methods. To compute the RPMs, we used a Support Vector Machine (SVM) with a radial basis function kernel. This is a relatively flexible classifier that has proven to be successful in many applications. We performed multi-class classification by combining one-vs-one classifiers. To obtain the RPMs, first pairwise class probabilities are obtained based on the distance to the one-vs-one decision boundary [23]. Subsequently, the pairwise probabilities are combined (as in [117]) to obtain the regional probabilities. Finally, these are normalized to sum to one: $\sum_{t=0}^{M} P_{R_t}(\boldsymbol{x}) = 1$.

3.3 Experiments and Results

We applied the presented coupled OSG approach that maximizes the enclosed regional probabilities to segment the carotid artery bifurcation wall in MRI. We compared the segmentations using the presented method to the segmentations obtained using only edge information as in Chapter 2, and to the solution by voxelwise SVM classification inside a Region Of Interest (ROI).

3.3.1 Image Data and preprocessing

We used MRI of the carotid bifurcation from subjects with diseased arteries (stenosis between 30%-50%) from the Rotterdam study [105]. The method was evaluated on 49 carotid arteries from 30 subjects. From the 60 available arteries, we had to discard 11: four because of manual annotation errors, one was not annotated, and finally six were discarded because of errors in the centerline extraction causing the initialization to be outside the artery. Only for the comparison of the methods experiments we decided to discard the cases with wrong initialization as we wanted to focus on the segmentation part of the methods.
Several MRI sequences were acquired: Proton Density Weighted (PD) Black-Blood MRI (BB), PD Echo Planar Imaging MRI (EPI), 3D T1-weighted gradient echo MRI (T1), T2-weighted EPI MRI (T2), and Phase Contrast MRI (PC). The image resolutions are (in-plane voxel size $\times$ Slice thickness): $0.507 \times 0.507 \times 0.9\,mm$ for BB, $0.703 \times 0.703 \times 1\,mm$ for PC, $0.507 \times 0.507 \times 1.2\,mm$ for EPI, $0.703 \times 0.703 \times 0.5\,mm$ for T1, and $0.507 \times 0.507 \times 1.2\,mm$ for T2. Each sequence provides different information to describe the three regions to segment: lumen, wall, and background. Whereas the PD sequences (BB and EPI) are more commonly used to depict the vessel wall, PC is good to visualize the lumen, and T1 and T2 provide more information on plaque composition in case of disease [105].
The coarse initial segmentation of the innermost surface required to initialize the OSG method was obtained by applying a morphological dilation (using a disk structuring element with radius of 2.5mm) to the vessel lumen centerline, which was obtained by a semi-automatic centerline extraction method using both BB and PC based on minimum shortest cost path presented by [94]. This method requires three marked

seed points per artery. Here PC is rigidly registered to BB, and therefore the initial segmentation is in BB coordinates, resulting in an OSG also in the same coordinate system.
To all image sequences a N4 bias field correction using the default set of parameters [100] was applied. Subsequently, the four other sequences were non-rigidly registered to BB using the registration configuration presented in [111]. Subsequently, we applied a linear intensity normalization to the images such that the 5% intensity percentile $I_{5\%}$ and 95% intensity percentile $I_{95\%}$ were scaled between constant values $\bar{I}_{5\%}$ and $\bar{I}_{95\%}$. $\bar{I}_{5\%}$ and $\bar{I}_{95\%}$ were chosen such that the highest intensity resolution was achieved while preventing data overflow or underflow. Finally, the images were cropped 22.5 mm below and 6.3 mm above the bifurcation point of the carotid artery. A smaller region was used if the marked seed points were defined under this range.
Manually segmented volumes for all 49 arteries were obtained from annotated contours by an expert on the BB images using a similar segmentation framework as described in [46]. These manual volumes were used to optimize the parameters and evaluate the methods in cross-validation experiments.

3.3.2 Experiments

We performed a three-fold cross-validation to train the SVM classifier and to optimize the parameters of the OSG methods. Three folds consisting of 10-11 subjects each were used, where three sets consisting of two folds represented the training sets. Then, we trained the methods on each of these three sets and evaluated on the third held out fold. We compared the following methods: OSG method + BB regional probabilities (OSG-BB), OSG method + BB & EPI regional probabilities (OSG-BBEPI), OSG method + All images regional probabilities (OSG-ALL), OSG using only edge information from BB as in Chapter 2 (OSG-Edge), Voxel classification using BB (SVM-BB), Voxel classification using from BB & EPI (SVM-BBEPI), Voxel classification using using all sequences (SVM-ALL).
As BB has been reported to be the best sequence to detect the artery wall [105], we chose to use it on its own in OSG-BB, SVM-BB and OSG-Edge. Additionally, as we previously reported that BB and EPI combined gives better or similar results than using only BB [6], we also evaluate those two combined in OSG-BBEPI and SVM-BBEPI. Finally, we used all sequences in OSG-ALL and SVM-ALL to evaluate the combined contribution of all the available sequences.
The training consisted of two steps: firstly we optimized the SVM parameters to obtain the RPMs on each training set, and secondly we optimized the parameters of the OSG methods using these RPMs.

3.3.3 Feature set

To compute the RPMs, we extracted features from all five image sequences. As described above, RPMs were computed using three sets of features: from BB alone, from BB and EPI, and from all image sequences. We extracted a set of 16 image features per image (so 80 in total for all 5 images), and 3 spatial features: 1) The image intensity; 2-4) Smoothed image intensities using a 3D Gaussian kernel at three

different scales: 1, 2 and 3 times the in-plane voxel size (0.507 mm); 5-10) The 1st order Gaussian directional derivatives at the same three scales, in radially outward direction from the two obtained artery centerlines; 11-16) The 2nd order Gaussian directional derivatives at the same three scales, in radially outward direction from the two centerlines separately; 17,18) The in-plane Euclidean distance to both centerlines separately; 19) The slice position along the centerline with respect to the bifurcation (negative proximal to the bifurcation and positive distal to the bifurcation).
In each individual experiment the features were normalized by scaling each feature in the training set to zero mean and unit standard deviation. The same transformation (X-mean(Ftrain)) / std(Ftrain), with X the feature value in the testset and Ftrain the set of feature values in the trainset) was then applied to this experiment's test data.

3.3.4 SVM classification

Subsequently, an SVM classifier was trained on the feature vectors of the training set and applied to obtain RPMs in the test images. We used the LIB-SVM toolbox [23] to perform the SVM classification. An example of images and the obtained RPMs are shown in Figure 3.2.
To train the SVM classifier we sampled training data from all arteries in the train set. For each artery we randomly selected the same number of samples for each of the three regions using the manually segmented volumes: 5% of all voxels from the smallest region (lumen or wall depending on the vessel), and the same number of voxels randomly taken from the other two regions. Background samples were taken from a region within six voxels around the outer wall border.
In our parameter optimization experiments we varied the slack parameter C of the SVM between $\{0.001, 0.01, ..., 1000\}$, and the SVM kernel radius γ between $\{0.0001, 0.001, ..., 100\}$.
To optimize these parameters we calculated the classification accuracy for each combination of C and γ for each patient using leave-one-patient-out cross-validation within the training set. Per training set the C and γ yielding the highest average accuracy were selected shown in Table 3.1, and an SVM classifier trained on the full training set using the selected C and γ was applied to generate RPMs for the images in the test fold.
Additionally, RPMs for the training images were generated using the selected C and γ in a leave-one-patient-out fashion within the training set. These RPMs were used to tune the OSG parameters as described in Section 3.3.5.

3.3.5 Graph Parameter Optimization

Using the obtained RPMs in the training images, the parameters to optimize in the graph methods are: the standard deviation σ to smooth the initial segmentation; the sampling interval δ, the smoothing penalization constants p^1 and p^2, and the minimum vertex distance between borders Δ. As in Chapter 2, δ was fixed to 0.35 mm to generate a higher resolution graph than the original images. As the minimum carotid wall thickness is about 0.8mm [89], we fixed $\Delta = 2$ vertices, which

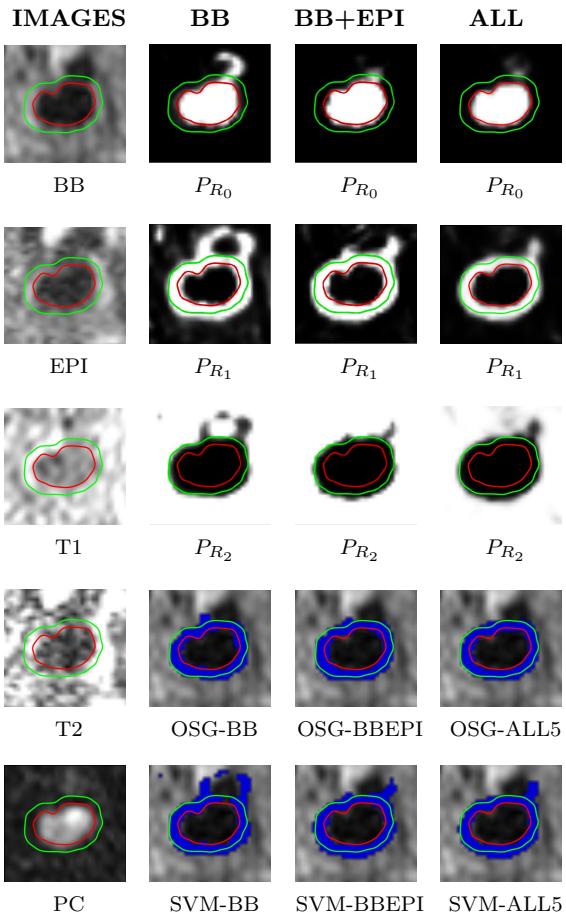

Figure 3.2. Image sequences, RPMs and automatic segmentation examples. First column: image sequences after N4 bias field correction, registration, and intensity normalization. Second column: RPMs of lumen, wall, and background respectively, and the wall automatic segmentations using only BB. Third column: RPMs and segmentations using BB and EPI. Fourth column: RPMs and segmentations using all image sequences. The manually annotated inner borders are represented by red, and the outer borders by green contours. The automatic segmented walls are represented in blue.

represents a distance of 0.7mm between vertices. We performed a grid search to find the optimal values which optimize the mean Dice Similarity Coefficient (DSC) of the segmented wall compared to the manually segmented volumes on each training fold. For the OSG using the RPMs, we searched for p^1 between $\{0, 100, ..., 500\}$, p^2 between $\{0, 100, ..., 1000\}$, and σ between $\{1, 1.1, ..., 1.5\}$, while for OSG-Edge we searched for p^1 between $\{0, 100, ..., 2000\}$, p^2 between $\{0, 100, ..., 2000\}$, and σ between $\{0.8, 0.9, ..., 1.2\}$. The obtained optimal parameters for each method in each training

fold are shown in table 3.1. In most cases, a similar set of parameters was obtained in all three folds for the different methods. This reflects the robustness of the methods using different data sets.

Table 3.1. Optimal parameters for each segmentation method on each training fold.

Method	Train Fold	C	γ	p^1	p^2	σ
OSG-BB	1	100	0.01	100	400	1.2
	2	100	0.01	100	500	1.1
	3	100	0.01	300	600	1.2
OSG-BBEPI	1	10	0.01	0	500	1.2
	2	10	0.01	0	400	1.1
	3	10	0.01	100	400	1.2
OSG-ALL	1	1	0.01	200	200	1.2
	2	100	0.001	200	200	1.0
	3	1	0.01	100	500	1.2
OSG-Edge	1	–	–	900	700	0.9
	2	–	–	800	700	0.9
	3	–	–	900	700	0.9

3.3.6 Methods Comparison Results

Using the optimal parameters determined in the training sets, we applied the segmentation method in the held out subjects for testing.
An example of the image sequences, regional probabilities, and cross-sectional segmentation results is shown for one vessel cross-section in Figure 3.2. Additional segmentation results are shown in Figure 3.3. Better wall segmentations using the presented method that combines the OSG and the regional probabilities are observed. The segmentations using the SVM classifier look more irregular and may include neighboring structures in the segmentation. However, when including more image features, the regional probabilities and the SVM-based segmentations improve. The segmentation using OSG-Edge tends to find the stronger edge, which may not be the artery edge and leads to clear errors in examples 1, 3 and 4 in Figure 3.3. Further, examples 2-6 show a plaque, where the presented method using the RPMs with the OSG obtains fairly good segmentations, indicating that the method performs well in presence of artery disease.
We computed the artery wall, lumen, and complete vessel DSCs for all the 49 arteries using the presented methods. For the segmentations using the SVM only, a ROI of 1.57cm radius around the computed centerline was used. This radius was selected because it was the minimum necessary to cover all manually annotated arteries. The

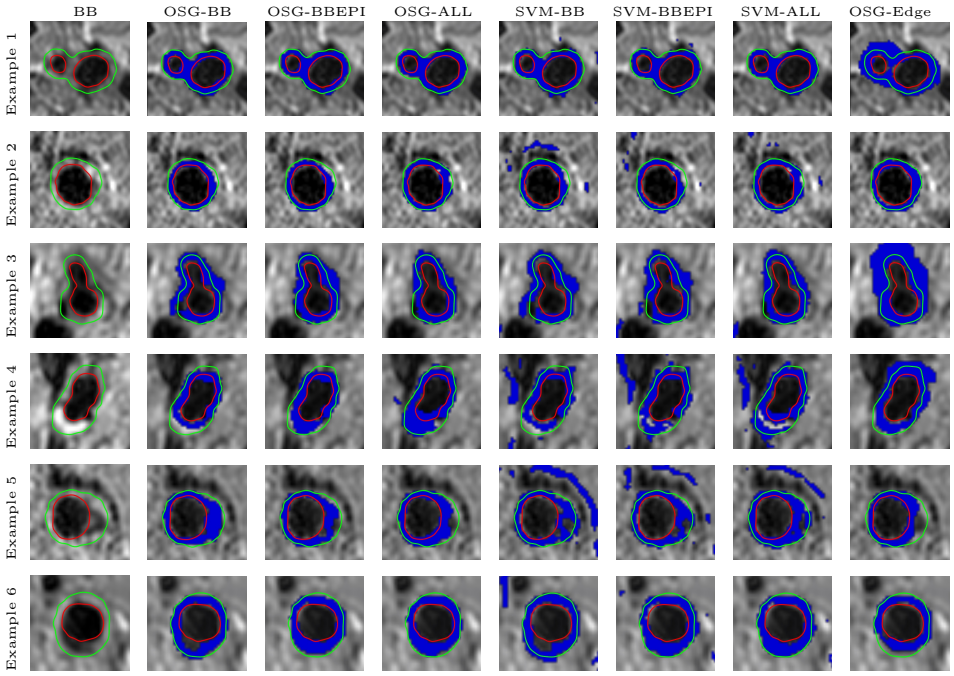

Figure 3.3. Examples of segmentation results (for the SVM methods only results inside the ROI are shown). The manually annotated inner borders are represented by red, and the outer borders by green contours. The automatic segmented walls are represented by blue surfaces overlaying the BB image.

DSCs for the different methods are shown in Table 3.2. We performed Friedman analysis with a post-hoc analysis based on Tukey-Kramer testing for multiple comparisons to determine significant differences based on the statistical test (also shown in Table 3.2). The presented methods that maximize the regional probabilities using the OSG are significantly better than the segmentations based on the classifier alone and OSG-Edge ($p < 0.05$). For the SVM segmentations when increasing the number of features (more image sequences) higher average DSC was obtained. The method OSG-Edge performed better than the SVM segmentations.

3.3.7 Performance Evaluation of the Method

We performed additional tests to check the performance of the presented methods OSG-BB, OSG-BBEPI, and OSG-ALL. We compared these methods with manual segmentations from a second observer, we compared the methods with another method proposed in the literature, and finally we tested the scan-rescan reproducibility of the methods. The following experiments include the six discarded cases with centerline errors, where the graph parameters and classifier set up to segment these six cases were obtained by training the methods on the 49 arteries data set (see Section 3.3.7.3).

Table 3.2. DSC performance for all methods using a data set of 49 arteries, compared with manual annotations from Obs. 1. Values in the same row with the same colors are not significantly different. The orange values are not significantly different from the green and yellow values, and the purple values are not significantly different from the yellow values. All other color changes indicate significant differences ($p < 0.05$).

	OSG-BB	OSG-BBEPI	OSG-ALL	SVM-BB	SVM-BBEPI	SVM-ALL	OSG-Edge
Wall DSC	74.1% ± 4.3%	73.7% ± 5.7%	73.9% ± 5.9%	60.9% ± 6.0%	61.4% ± 8.3%	65.6% ± 9.1%	67.5% ± 6.7%
Lumen DSC	88.3% ± 3.5%	88.6% ± 3.1%	88.7% ± 3.8%	87.6% ± 4.0%	87.2% ± 5.0%	86.6% ± 6.0%	91.9% ± 2.6%
Complete DSC	92.7% ± 1.8%	92.6% ± 2.2%	92.5% ± 2.7%	81.7% ± 5.6%	81.9% ± 7.1%	83.6% ± 7.4%	87.4% ± 4.0%

3.3.7.1 Comparison with a second observer

First, we compared the methods segmentation results to the manual segmentations from a second observer which were available in a subset of 27 arteries from 15 subjects. Segmented volumes were cropped as in the previous section. Not the complete bifurcation was evaluated as the second observer only segmented one of the branches. DSCs for wall, lumen, and complete vessel are listed in Table 3.3. In 5 out of 6 comparisons, the wall overlap between the automatic method and the observer was significantly better than the overlap between the two observers. Additionally, scatter plots showing the wall volume correlation between OSG-BB and manual volumes are depicted in Figure 3.4(a). High correlations between wall volumes are observed.

Table 3.3. DSC performance comparison between OSG-BB, OSG-BBEPI, OSG-ALL and the manually segmented volumes from two observers in a subset of 27 arteries for which two manual annotations are available. Values in the row with the same colors are not significantly different ($p > 0.05$) (purple values are not significantly different to blue and black values).

	OSG-BB Vs. Obs. 1	OSG-BBEPI Vs. Obs. 1	OSG-ALL Vs. Obs. 1	OSG-BB Vs. Obs. 2	OSG-BBEPI Vs. Obs. 2	OSG-ALL Vs. Obs. 2	Obs. 1 Vs. Obs. 2
Wall DSC	73.8% ± 6.7%	73.4% ± 6.6%	74.7% ± 4.8%	70.7% ± 8.7%	69.9% ± 9.2%	71.1% ± 8.8%	65.1% ± 8.9%
Lumen DSC	88.5% ± 4.8%	89.3% ± 3.5%	89.5% ± 3.2%	85.9% ± 5.7%	85.9% ± 4.9%	86.6% ± 5.0%	81.9% ± 5.1%
Complete DSC	93.2% ± 2.7%	93.3% ± 2.2%	93.5% ± 1.9%	88.9% ± 3.7%	89.3% ± 3.6%	89.1% ± 3.9%	90.3% ± 3.2%

3.3.7.2 Comparison with [45]

Additionally, we compared the presented methods to the best method presented by [45], which is a method based on a cylindrical deformable surface model with a learning-based postprocessing. We used the publicly available dataset of [45] for this comparison, which consists of 41 arteries from 22 subjects which are a subset of the data presented in the rest of this chapter. As the method proposed by [45] cannot segment the complete bifurcation, only the common and internal carotid arteries were

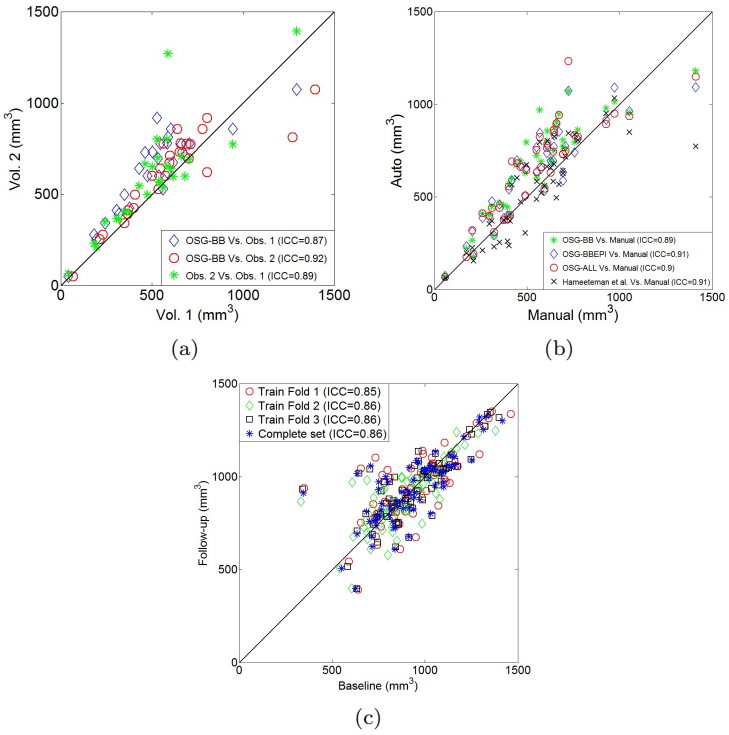

Figure 3.4. Scatter plots (Vol. 2 Vs. Vol. 1) between: (a) the automatic and the two observer segmentations in a subset of 27 arteries for which two manual annotations are available, (b) OSG-BB, OSG-BBEPI, OSG-ALL and the method presented by [45] and the manual segmentations using a subset of 41 arteries, and (c) follow-up wall volumes vs. Baseline wall volumes using a scan-rescan data set of 71 arteries, for the method OSG-BB trained on a complete data set of 49 arteries and its 3 training folds (see Section 3.3.2)

evaluated. DSCs values for the different methods are shown in Table 3.4. Significantly better results ($p > 0.05$) were obtained using the presented method for OSG-ALL. A scatter plot showing the wall volume correlations is depicted in Figure 3.4(b). Here, similar intra-class correlations were obtained.

3.3.7.3 Reproducibility analysis:

Scan-rescan reproducibility was assessed on a different set of 71 arteries from 36 patients (one artery was discarded because the seed points were placed wrongly) who were imaged twice within a short time interval (15 ± 9 days), so significant wall volume changes are not expected. For these experiments, we retrained and optimized the SVM and graph parameters for OSG-BB, OSG-BBEPI, OSG-ALL using the full set of 49 manually segmented arteries. The resulting optimal parameters

Table 3.4. DSC performance comparison between OSG-BB, OSG-BBEPI, OSG-ALL and the method presented by [45] with respected to the manual segmented volumes from observer 1 using a subset of 41 arteries. Values in the row with the same colors are not significantly different ($p > 0.05$) (purple values are not significantly different to blue and black values).

	OSG-BB	OSG-BBEPI	OSG-ALL	[45]
Wall DSC	$74.1\% \pm 6.3\%$	$73.7\% \pm 6.6\%$	$74.1\% \pm 6.2\%$	$67.0\% \pm 13.4\%$
Lumen DSC	$88.8\% \pm 4.4\%$	$89.0\% \pm 3.5\%$	$89.1\% \pm 4.1\%$	$86.6\% \pm 7.7\%$
Complete DSC	$92.8\% \pm 2.7\%$	$93.0\% \pm 2.4\%$	$92.9\% \pm 2.9\%$	$89.3\% \pm 6.8\%$

were: for OSG-BB: C=100, $\gamma = 0.01$, $p^1 = 100$, $p^2 = 500$, $\sigma = 1.2$; for OSG-BBEPI: C=10, $\gamma = 0.01$, $p^1 = 0$, $p^2 = 500$, $\sigma = 1.2$; and for OSG-ALL: C=1, $\gamma = 0.01$, $p^1 = 200$, $p^2 = 400$, $\sigma = 1.2$. Additionally, to evaluate the effect of changes in the training data, we also used the trained SVM and optimized parameters from each of the three training folds (see Table 3.1). Using these settings, we segmented all 71 arteries. All segmented volumes were cropped from 18 mm below up to 2.7 mm above a manually indicated carotid bifurcation point in order to compare similar regions between baseline and follow-up. Scatter plot showing the correlations between vessel wall volumes at baseline and follow-up using the optimal parameters for each training set of OSG-BB is shown in Figure 3.4(c). Similar intra-class correlations are shown using each set of parameters indicating good robustness of the method. Higher correlations were obtained using OSG-BB, with absolute volume differences (for the methods trained on the complete set) of $12\% \pm 21\%$ for OSG-BB, $14\% \pm 24\%$ for OSG-BBEPI, and $14\% \pm 24\%$ for OSG-ALL.

3.4 Discussion

In this chapter, we proposed a new segmentation method for coupled surfaces that maximizes the regional probabilities within each segmented region using a coupled OSG method. This method was applied to segment the carotid artery wall in MRI. This method is especially useful for this application as the used graph structure allows the segmentation of high curvature surfaces at the carotid bifurcation. Similar methods for multi-region coupled surfaces segmentation as the one presented in [44] are suitable to segment terrain-like and cylindrical surfaces. However, they are difficult to implement on high curvature surfaces as the carotid artery. Other segmentation methods that use regional information which are not based on OSG models [30, 103] do not introduce an initialization shape prior in their model, which in our specific application proved to be useful. In addition, our regional information based on SVM classifier using as many features as desired showed very robust results for this application, while in the other methods only a limited set of regional features is considered. We argue that our method is suitable for any coupled multi-surface segmentation problem for which it is possible to obtain a coarse initial segmentation of any of the

surfaces to segment.

Our results showed that an OSG approach combined with classifier-based regional probabilities improved segmentations over both an OSG method using only edge information as presented in Chapter 2, and a pure voxel classification-based method inside a ROI. Our explanation for this is that the method that only uses edge information tends to find the stronger edge in the image which may not be the artery edge, and that the classifier alone does not have any geometrical constraints which leads to more irregular surfaces and leakage into other structures that resemble the arterial wall.

Additionally, we showed that combining information from multiple image sequences does not have a big impact in the presented application. Although better voxel-wise segmentation results were obtained when including more image sequences, inaccuracies in the RPMs are easily corrected using OSG.

The OSG method is not very sensitive to changes in the model parameters, as similar performances were obtained with different parameters in the reproducibility results. However, if different data will be used (for instance images from a different scanner or using a different MRI protocol), re-training the SVM classifiers is likely to be necessary. On a different application OSG parameters naturally require retraining as well.

Using the proposed method we obtained higher wall DSC results compared to two different observers. Reproducibility experiments showed good correlations between scan and re-scan segmented volumes. This correlation is similar to between observers, which shows that the method is highly reproducible even between scan sessions. The observed scan and re-scan segmented volume differences are significantly lower than what has been reported in clinical time intervals (59% volume change in 18.9 months interval, see [86]), which suggest that this method can be reliably applied in longitudinal studies. We expect this method could be used in more diseased patients, as we observed fairly good segmentations in the diseased sections.

Although we obtained good overlap with manual segmentations, the obtained surfaces were not always smooth, as during the training of the method, we were aiming to get the highest wall overlapping without considering the smoothness of the segmented surfaces. A parameter training also targeting smoother results could help to get more visually appealing segmentations.

Lastly, we compared with a previously presented method for carotid wall segmentation [45], which already performed better than another previously published method [110]. We obtained similar wall volume correlations, and better and more robust DSC overlaps. Additionally, our method is more suitable for segmenting the bifurcation, since it incorporates this geometry into the method, while in [45] it is necessary to combine two tubular segmentations. There are other methods to segment the artery wall, e.g. [103], which presented average lumen DSCs above 86% and complete vessel DSCs above 87%. These results are similar to the presented results by our method, however it is difficult to compare with these as the data is different. Additionally our method requires less user interaction compared to [103].

3.5 Conclusion

In conclusion, we formulated a novel cost function to maximize regional probabilities using the coupled OSG model presented in [76]. With our proposed method the maximum sum of enclosed class-conditional probabilities in each region is achieved while ensuring smooth surfaces and topologically correct segmentations. We applied this method to segment the carotid artery wall in MRI. The method outperformed a voxel-wise segmentation approach using the regional probability maps only, as well as an OSG segmentation using only edge information, and a recently published method. Obtained automatic segmentation results were of similar quality as manual segmentations by experienced observers and showed good scan-rescan reproducibility.

Chapter Four

Carotid artery lumen segmentation on 3D free-hand ultrasound images using surface graph cuts

Abstract — We present a new approach for automated segmentation of the carotid lumen bifurcation from 3D free-hand ultrasound using a 3D surface graph cut method. The method requires only the manual selection of single seed points in the internal, external, and common carotid arteries. Subsequently, the centerline between these points is automatically traced, and the optimal lumen surface is found around the centerline using graph cuts. To refine the result, the latter process was iterated. The method was tested on twelve carotid arteries from six subjects including three patients with a moderate carotid artery stenosis. Our method successfully segmented the lumen in all cases. We obtained an average dice overlap with respect to a manual segmentation of 84% for healthy volunteers. For the patient data, we obtained a dice overlap of 66.7%.

Based upon: Andrs M. Arias-Lorza, Diego D.B. Carvalho, Jens Petersen, Anouk C. van Dijk, Aad van der Lugt, Wiro J. Niessen, Stefan Klein, and Marleen de Bruijne, "Carotid artery lumen segmentation on 3D free-hand ultrasound images using surface graph cuts", *published* in MICCAI, 2013.

4.1 Introduction

Ultrasound (US) enables low cost non-invasive imaging of the carotid arteries for identifying carotid atherosclerotic plaque [107] and investigating the carotid artery geometry, which are associated with vascular events. Carotid arteries are most frequently imaged using a 2D free-hand US probe; using a tracking device it is possible to compound a series of 2D US images into a 3D volume [37]. Methods for automated lumen segmentation of 3D US data would enable the investigation of carotid artery geometry and the narrowing of the vessel caused by the presence of plaque [2]. However, segmenting the lumen in US is a difficult task, due to image noise, shadows and speckle inside the lumen. Another problem is that in US images the vessel boundary parallel to the US beam is not visible.
Ukwatta et al. [102] proposed a semiautomatic carotid segmentation method on 3D US data using a level set based method. Although their segmentation results are good, this method requires considerable user interaction, as anchor points on transverse slices where the evolving curve must pass through need to be indicated. In addition, they only segment the common carotid artery. A complete segmentation of the carotid artery based on level sets is proposed by Hossain et al. [50]. However, the user has to initialize boundary points for every slice.
Graph-based methods have been used for vessel segmentation in CTA and MRI obtaining promising results [5, 36]. Surface-based graph methods such as [5] as opposed to voxel based methods [36] make it possible to enforce topology constraints and incorporate a shape prior of the arteries. In this chapter we propose a method based on surface graph cuts to segment the complete carotid artery lumen in 3D free-hand US images with minimal user interaction. Following the method presented in Chapter 2 for segmenting the carotid artery wall on MRI, we define the graph columns traced from a coarse initial segmentation, which is approximated by a morphological dilation of the lumen centerline. Each graph column is associated with a point on the sought surface and represents the set of possible solutions. As such graph columns do not intersect each other, this enables accurate, non self-intersecting segmentation across high curvature areas such as the carotid bifurcation [5]. Finally, to deal with errors or variability induced by the initialization, this procedure is iterated several times.

4.2 Method

4.2.0.1 Centerline Extraction and Initial Segmentation

The graph is constructed from a coarse initial segmentation of the carotid vessel lumen, obtained from its centerline. We adapted the US centerline extraction algorithm presented in [19]. This method tracks lumen centerlines in US through ellipse fitting in transversal 2D cross-sections of the artery. The input of the algorithm are three user defined seed points in the lumen, positioned at the beginning of the internal, external and common carotid artery (ICA, ECA and CCA) respectively. From each seed point, rays are traced in all directions of the cross-section checking the pixel intensity at each position. In [19], the ray stops when an intensity above a certain threshold is found, indicating that the border of the vessel has probably been reached.

We modified this criterion in order to make it more robust against pixel intensity variations in the lumen. In our approach, directional derivatives are calculated along each ray. The third quartile of all the directional derivatives for all rays is selected as the threshold y_{th}. This is represented as $\sum_{x \leq y_{th}} P_y(x) = 0.75$ where P_y represents the estimated probability distribution of the directional derivatives $y : \Omega_r \rightarrow \mathbb{R}$ given by $y(\boldsymbol{x}) = \frac{\partial I(\boldsymbol{r_x}(t))}{\partial t}$, Ω_r is the set of image positions indicated by the rays in the cross-section, I is the image intensity, and $\boldsymbol{r_x} : \mathbb{R} \rightarrow \mathbb{R}^2$ is the ray trajectory at position $\boldsymbol{x}$. Thereafter, all steps are similar to [19] but considering the directional derivatives instead of the intensities.
The centerline is subsequently smoothed to reduce the influence of noise. The centerline in the CCA is then connected to the centerline in the ICA and the ECA. Finally, the centerline is dilated with a 2mm diameter spherical structuring element to obtain a coarse approximation of the lumen. This rough segmentation acts as an input for the segmentation method.

4.2.0.2 Graph Construction

Based on this initial rough segmentation, a graph is constructed. The surface graph approach proposed in this chapter is an adaptation of the method presented in Chapter 2. To construct the graph, first the graph columns have to be traced in the image. Each graph column represents a set of possible solutions for a point in the sought surface. Hereto, the coarse initial segmentation is converted to a surface mesh with vertices V_B at the centers of each face on the surface of the voxelized initial segmentation. These graph vertices V_B represent the starting points of the columns. A schematic of a coarse initial segmentation of the carotid vessel lumen and its mesh conversion is shown in Figures 4.1(a) and 4.1(b), respectively.
The graph columns are traced from all V_B, and follow the direction of the flow lines $\boldsymbol{f}$: $\mathbb{R} \rightarrow \mathbb{R}^3$ of the gradient vector field obtained by Gaussian smoothing of the initial segmentation ϕ: $\mathbb{R}^3 \rightarrow \mathbb{R}$ [5,77], this is represented by the equation $\frac{\partial \boldsymbol{f}}{\partial t}(t) = \nabla\phi(\boldsymbol{f}(t))$ with initial value given by $\boldsymbol{f}(0) \in V_B$. An example of a gradient vector field of a smoothed segmentation ϕ is shown in Figure 4.1(c). The flow lines traced along this gradient vector field, starting from the graph vertices located at the mesh surface are indicated by the red lines in Figure 4.1(d). From the figure it can be seen that the graph columns defined by flow lines traced along the gradient of ϕ are smooth and non-intersecting. Because in a graph cut method each column is cut once, this results in non-self-intersecting surfaces [77].
The remaining column vertices V of the graph, which represent all possible lumen surface segmentation points, are sampled at regular intervals δ along the flow-lines. The length of each column varies, and is defined by the position where the smoothed segmentation ϕ vanishes. Finally, source s and sink t vertices are added to the graph, representing the innermost and outermost vertices respectively. A representation of the vertices in the graph is given in Figure 4.2(a) by the black dots.
Next, the edges E of the surface graph $G = (V, E)$ need to be defined. The edge set consists of intra-column edges E_{intra} and edges between columns E_{inter} [5, 77]. The intra-column edges are associated to the likelihood that a vertex in a column is part of the lumen surface, while the edges between columns E_{inter} penalize irregularities

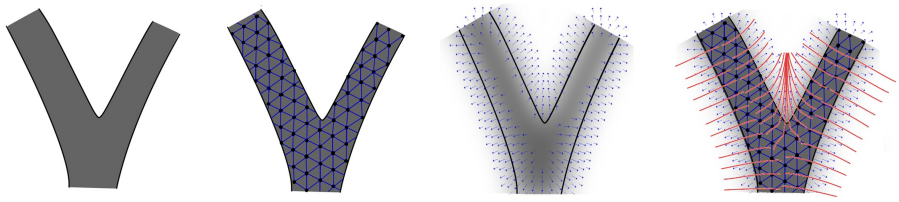

(a) (b) (c) (d)

Figure 4.1. Graph columns construction based on flow lines. Graph columns are generated from an initial coarse segmentation as shown in (a). This initial segmentation is converted to a surface mesh, where vertices of the graph columns are at the center of each surface voxel face as depicted in (b) by black dots. Subsequently, the coarse initial segmentation is smoothed and a gradient vector field is computed, see (c). Finally, (d) shows the graph columns represented by red lines which trace this gradient field from the vertices located at the mesh surface.

on the final segmentation, ensuring smooth surfaces. To model this behavior on the surface graph G, the intra-column edges E_{intra} associated with a cost $w \in \mathbb{R}$ are represented by directed edges connecting each vertex to the next vertex in an outward direction in the same column [5]. In addition, the source vertex s is connected to all innermost vertices in the graph, and all outermost vertices are connected to the sink vertex t. A representation of the intra-column edges is provided in Figure 4.2(a). In our surface graph cut method, the main aim is to find a cut that minimizes the cost of the edges that are being cut. Therefore, the cost w is associated to the inverse of the likelihood that the edge being cut belongs to the sought surface. As in [5], this cost is inversely proportional to the first order derivative along the graph column given by $\frac{\partial I(\boldsymbol{f}(t))}{\partial t}$, where I is the image intensity. This leads to low costs for strong dark to bright transitions that are typically present at the lumen border in US. The true vessel surface may be slightly inward or outward of the image intensity edge position along the column. Therefore, we adjust the position of the lowest value of w along the graph column by adding the second order derivative to the first order derivative. This linear combination is represented by $L(t) = \alpha \frac{\partial^2 I(\boldsymbol{f}(t))}{\partial t^2}(t) + (1 - |\alpha|) \frac{\partial I(\boldsymbol{f}(t))}{\partial t}$ where α is a parameter representing the contribution of the second order derivative.

In many columns, the position of the lumen boundary will not be clear due to image noise or shadows caused by nearby vessels. To determine the position of the surface in these columns, information from neighboring columns with better contrast in the intensity profiles must be used. Therefore, we add edges between neighboring columns E_{inter}, which linearly penalize jumps between the columns. This way, the local image information associated to the intra-column edges is integrated into a global and smooth segmentation solution. An example of these inter-column edges is depicted in Figure 4.2(b). In the figure, the edges between columns are depicted by blue arrows. The cut cost associated to the edges between columns is linearly proportional to the number of edges that are being cut.

Finally, a 3D segmentation is obtained by solving the graph cut minimization problem. The vertices located directly inside of the optimal cut represent the sought surface.

This minimization is solved by applying a min-cut/max-flow optimization algorithm [17].

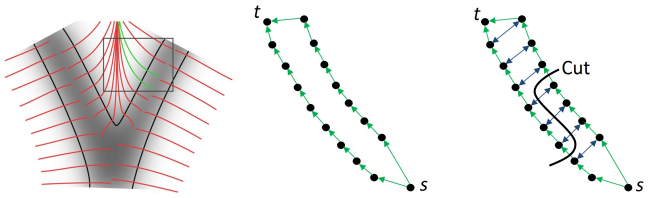

Figure 4.2. Description of graph edges. The intra-column edges are depicted by green arrows in (a). The edges between neighbor columns are depicted by blue arrows in (b). Additionally, an example of a graph cut is shown in (b).

4.2.0.3 Iterative approach

Owing to the presence of noise in the image, the extracted initial centerline may present irregularities. Therefore, the coarse initial segmentation may still deviate from the sought lumen surface. Examples of a coarse initial segmentation and the segmentation result after one iteration of the method in image slices are shown in Figure 4.3. From the figure, we can observe that in some sections the initial segmentation contour is far from the lumen contour. With standard column lengths defined by the smoothing scale σ of the initial segmentation, the graph columns may not reach the lumen border resulting in an under segmentation, as is the case in Figure 4.3. To obtain a correct segmentation in the cases that the initialization is far from the lumen surface, we proposed and evaluated two possible solutions. First, the length of the graph columns can be extended. This is achieved by smoothing the initial segmentation with a higher scale σ, such that the gradient vector field can be traced further, resulting in longer columns. However, these longer columns may intersect edges of other vessels close to the carotid artery possibly resulting in a wrong segmentation. A second option is to apply an iterative approach. Here, the computed segmentation is used as initialization for a new graph. This may work in cases with wrong initialization because if some sections are segmented correctly then the optimal graph cut solution approaches the lumen surface thanks to the smoothness constraint. Example results of the iterative approach are shown in Figure 4.3, indicating that after every iteration the segmentation results were improved.

4.3 Experiments and Results

To validate our method, we segment the carotid lumen in 20 carotid arteries of ten subjects, six healthy volunteers and four patients with a moderate carotid artery stenosis. Each image was acquired using free-hand US on the carotid section of the neck of the subject. A 3D volumetric representation was obtained with the help

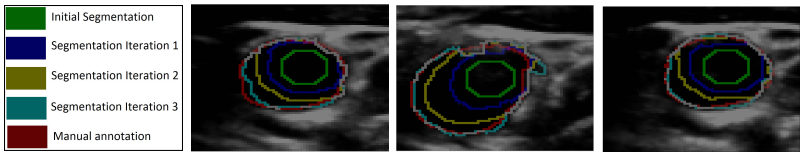

Figure 4.3. Segmentation results after several graph cut iterations for different volume slices.

of an external software, which correlates the position of a magnetic tracking sensor attached to the US probe and the US machine coordinates [37]. We used a Philips iU-22 US scanner with a L9-3 US probe, acquiring signals of 4cm depth on one patient and of 3cm depth on the remaining subjects. After exporting the data to a volumetric representation, the voxels dimension have 0.16mm^3 for probe depth of 3cm, and 0.21mm^3 for probe depth of 4cm. After, we obtain the centerline with the proposed method, to standardize the data, we cropped centerline points that are outside a 2cm radius from the bifurcation point. The proposed centerline extraction method was able to track the centerline in all cases and estimate the bifurcation point. All images were manually annotated. The manual segmentation was performed by annotating the lumen at each five to ten 2D slices. Thereafter, the lumen surface was interpolated based on these contours. We used eight carotid arteries from four subjects (three healthy volunteers and one patient) to optimize the parameters of the method: the smoothing scale σ, the weighting parameter α that weights the influence of the first and second order derivatives of the edge cost w, the edge cost between columns p, and the number of iterations N. The sampling vertex distance δ was fixed to the voxel spacing 0.16mm. We performed an exhaustive joint parameter search to find the optimal set of parameters, which optimizes the Dice Segmentation Coefficient (DSC). We obtained the highest DSC using $\sigma = 10$, $\alpha = 0.5$, $p = 10,000$, and $N = 4$. Figure 4.4 show the effect of variations in the four parameters. The smoothing scale σ has little effect on the end results, while iterating the method clearly improves results.

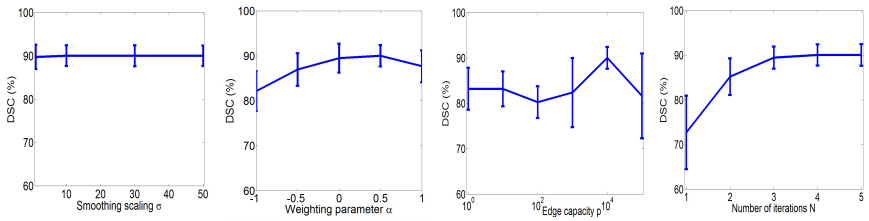

Figure 4.4. Effect of the segmentation parameters on segmentation overlap, when varying a single parameter while the other parameters are fixed at their optimum value. The error bars denote the standard deviation. From left to right: the smoothing scaling σ, the weighting parameter α, the edge capacity p, and the number of iterations N.

We tested our method using 3D US images of twelve carotid arteries of three healthy volunteers and three patients. A 3D visualization of the segmentations compared

with the manual annotations for a volunteer and a patient are shown in Figure 4.5(a) and 4.5(b). A good agreement can be observed from the figures. Figure 4.5(c) shows the DSC values for the volunteers carotid arteries per iteration. The average DSC after applying four iterations is $84\% \pm 4.9\%$. The DSC values for the patients arteries are shown in figure 4.5(d). Here, the obtained average DSC for four iterations is $66.7\% \pm 8.3\%$.

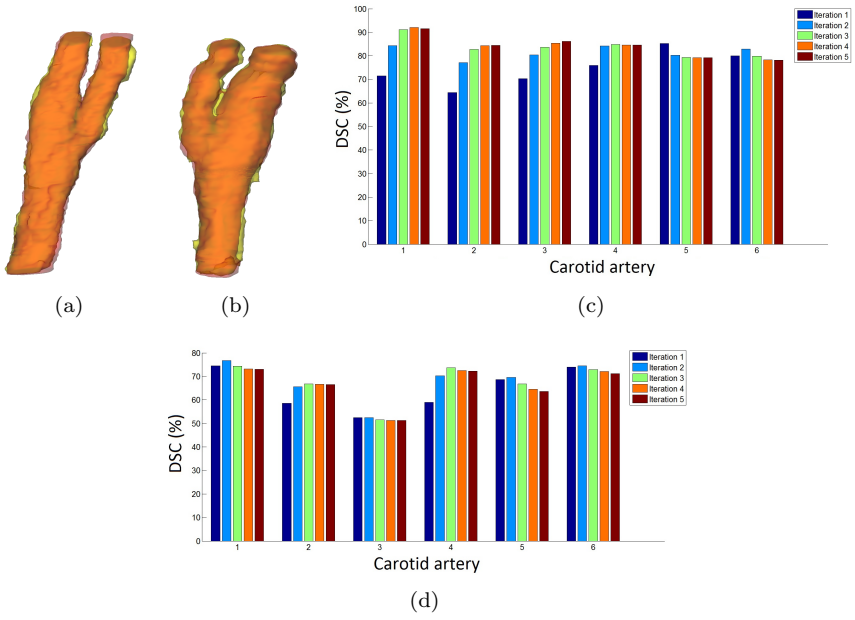

Figure 4.5. Segmentation results. Figures (a) and (b) show the manual annotated lumen (red) and the automated segmentation result (yellow) for a volunteer and patient artery respectively. Bar plots with the DSC for volunteer and patient carotid arteries in the testing set per iteration are shown in (c) and (d) respectively.

4.4 Discussion and Conclusion

In this chapter, we propose a new method to segment the carotid artery lumen, including the bifurcation area, in 3D free-hand US images using little user interaction. The obtained results showed good agreement with manual segmentation for healthy arteries, obtaining a DSC of 84% for healthy volunteers. However, the segmentation was less good in patient arteries, with a DSC of an average 66.7%. In this chapter, only two diseased arteries were included during the parameter tuning. We expect that including more patient data in the parameter tuning set would lead to a graph model that can describe plaque sections better, resulting in improved performance for these cases.

We proposed an improved centerline extraction method for US image based on [19] which was able to track the centerline and estimate the bifurcation point in all images

described in [19], while the method proposed by Carvalho et al. [19] failed in three cases. We also proposed a novel iterative surface graph cut approach based on [5]. As observed in Figures 4.5(c) and 4.5(d) in most of the cases the iterations improve the results.
Compared to the method proposed by Ukwatta et al. [102], who obtained an average DSC of 92%, we obtained lower DSC. However, in contrast to [102], our method can segment the lumen bifurcation, which may be relevant to predict vascular events. In addition, our method requires less user interaction, which makes it more suitable for large scale studies and for use in clinical practice. Hossain et al. [50] reported a method that can segment the complete carotid artery, including the bifurcation area. However, this method also requires substantial user interaction; the user has to locate initialization points on the boundary for every slice. In addition, they reported a processing time of about 40min, whereas our method computes a segmentation in under 3min using an Intel core 2 duo processor with 8 GB of RAM. In summary, the main advantages of our method are the ability to segment the complete carotid artery, fast and with little user interaction.

Chapter Five

Automated Registration of Free-hand B-mode Ultrasound and MRI of the Carotid Arteries Based on Geometrical Features

Abstract — In this chapter an automated method to register B-mode Ultrasound (US) and Magnetic Resonance Imaging (MRI) of the carotid arteries is proposed. The registration uses geometrical features, namely lumen centerlines and lumen segmentations, which are extracted fully automatically from the images after manual annotation of three seed points in US and MRI. The registration procedure starts with aligning the lumen centerlines using a point-based registration algorithm. The resulting rigid transformation is used to initialize a rigid and subsequent nonrigid registration procedure that jointly aligns centerlines and segmentations by minimizing a weighted sum of the Euclidean distance between centerlines and the dissimilarity between segmentations. The method was evaluated in 28 carotid arteries, from 8 patients and 6 healthy volunteers. We first validated and optimized the automated US lumen segmentation method in a cross-validation experiment. Next, we evaluated the effect of the weighting parameter of the proposed registration dissimilarity metric, and the control point spacing in the nonrigid registration. Finally, the proposed registration method was evaluated in comparison to an existing intensity-and-point based method, a registration using only the centerlines, and a registration using manual US lumen segmentations. Registration accuracy was measured in terms of the Mean Surface Distance (MSD) between manual US segmentations and the registered MRI segmentations. The average MSD was $0.78 \pm 0.34mm$ for all subjects, $0.65 \pm 0.09mm$ for healthy volunteers, and $0.87 \pm 0.42mm$ for patients. The results on the complete set were significantly better (Wilcoxon test, $p < 0.01$) than the results of the intensity-and-point based method, and the centerline based registration method. We conclude that the proposed method can robustly and accurately register US and MR images of the carotid artery, allowing multimodal analysis of the carotid plaque in order to improve plaque assessment.

Based upon: Diego D.B. Carvalho, Andrs M. Arias-Lorza, Wiro J. Niessen, Marleen de Bruijne, and Stefan Klein, "Automated Registration of Free-hand B-mode Ultrasound and MRI of the Carotid Arteries Based on Geometrical Features", *published* in Ultrasound in Medicine & Biology, 2016.

5.1 Introduction

Cerebrovascular disease ranks as the third worldwide leading cause of death [67]. The brain and muscles of the face are supplied with blood by a pair of vessels called the carotid arteries which are located in the neck. Atherosclerosis in the carotid arteries is one of the conditions that can cause cerebrovascular disease. Atherosclerosis is a process of inflammation in the arterial wall, leading to the formation of a plaque. Rupture of atherosclerotic plaques in the carotid artery can cause vessel obstruction and distal propagation of a thrombus [38] which may result in an ischemic stroke [18]. The risk of plaque rupture is associated with plaque composition and morphology [84]. Different imaging modalities supply complementary information on the carotid artery wall and plaque therein, leading to interest in multimodal imaging studies on the assessment of atherosclerosis and plaque vulnerability [22, 39, 97]. Even though most imaging modalities show the lumen and artery wall, each one emphasizes different properties: angiography is especially useful to visualize the stenosis severity; Computed Tomography (CT) visualizes plaque calcifications well; Magnetic Resonance (MR) shows intra-plaque haemorrhage, and necrotic cores; Ultrasound (US) shows echolucency and ulceration. US and MRI modalities are of special interest, since they do not involve any ionizing radiation, and US is a relatively low-cost modality. Figure 5.1 shows example slices of a free-hand transversal B-mode US scan and an MRI scan from the same patient.

Comprehensive multi-modal image analysis and side-by-side visualization of different imaging modalities is hampered by the lack of spatial correspondence between images from different modalities, as depicted in Figure 5.1. Besides global differences due to different image resolution, field-of-view, and orientation, there may even be changes in the artery geometry due to bending and twisting of the neck (as is typically required for US acquisition). Differences in the patient's neck position in US and MRI can be appreciated from Figure 5.2. Image registration is therefore required, to align the carotid arteries and compensate for deformations. Since US and MRI have very different image appearance, the registration of these images is a highly challenging problem.

MRI-US registration of the carotid artery has been addressed in previous works [20, 24, 43, 72, 91]. [91] presented the registration of 3D reconstruction of free-hand power doppler US (3D-US) and Magnetic Resonance Angiography (MRA) images. The vessel lumen is clearly visible in both modalities, and therefore it was used to drive the registration. The method uses a rigid transformation model, and is based on maximization of mutual information. The method was evaluated on data of six patients. [72] used a constrained nonrigid transformation model to register 3D-US and MRI. First an initial registration was performed based on geometrical landmarks; subsequently the images were registered using normalized mutual information as the registration metric [92]. 3D-US acquisition was performed with a motorized device attached to the probe, which generated a sequence of 2D B-Mode US images. They evaluated the registration method on images from six patients. [24] performed registration using points on the arterial outer wall. These points were extracted from a manual segmentation in MRI and a semi-automated segmentation in US. The artery bifurcation point was used to obtain an initial alignment, which was followed by a

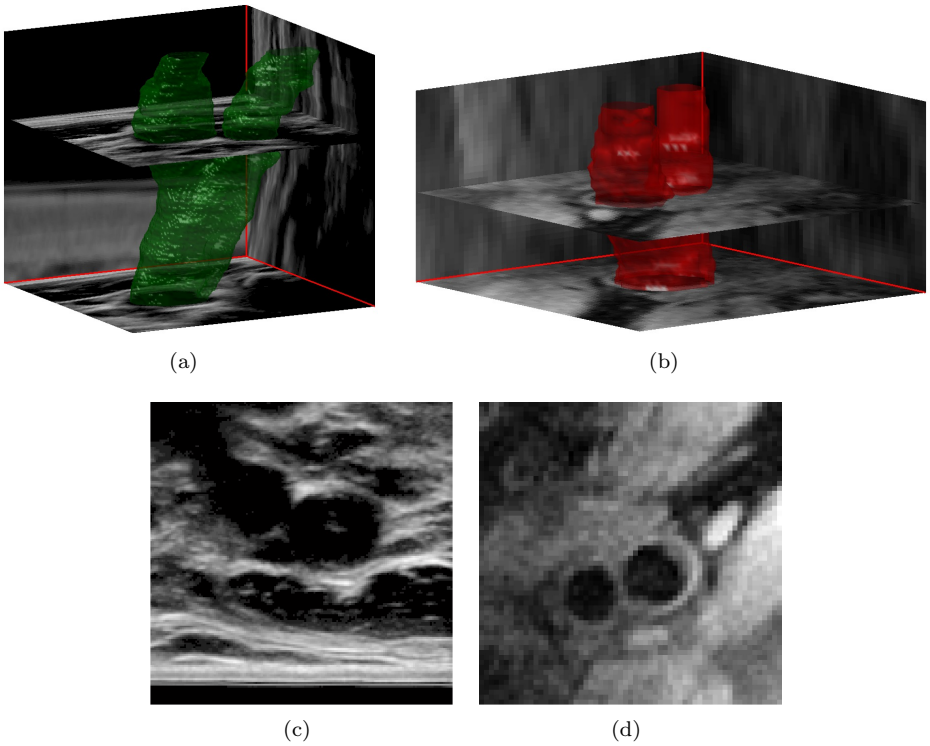

(a) (b)

(c) (d)

Figure 5.1. Multimodal carotid artery imaging. A 3D reconstruction of a free-hand transversal B-mode US scan (a), and an MRI scan of the carotid artery of the same patient (b). The green and red volumes represent the artery in both modalities. 2D slices intersecting the arteries taken at similar position close to the bifurcation on both modalities are shown in (c) and (d).

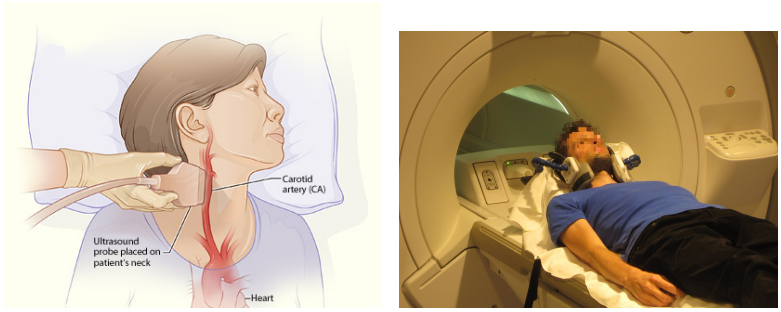

(a) source: Adapted from Wikimedia. Author: National Heart Lung and Blood Insitute (NIH).

(b) source: Wikimedia. Author: Blausen Medical Communications, Inc.

Figure 5.2. Position of the patient's neck during US (left) and MR (right) scanning.

rigid registration of the outer wall point sets using the Iterative Closest Point (ICP) algorithm [14]. Subsequently, a slice-by-slice manual registration refinement was performed. The method was evaluated on 3D-US acquired using a volumetric linear transducer and MRI data of three patients. [43] developed a method to register 3D-US and MRI using only geometrical features extracted from 2D manually annotated contours on both modalities. First, a rigid registration using a labeled ICP from the extracted centerlines is performed, followed by a non-rigid registration using 3D reconstructed surfaces. In our previous work [20], a framework was introduced to perform US-MRI registration using a joint intensity-and-point based registration of free-hand B-mode ultrasound and MRI data of the carotid artery. Since in MRI the tissues have an almost uniform image intensity [115], whereas in US mainly the border between tissues is highlighted [113], there is not a clear correlation between voxel intensities on both modalities, making it difficult to obtain good registration results based only on intensity information. Therefore, we proposed to combine intensity information with geometrical information. An initial registration using geometrical landmarks on the lumen centerlines was performed. Subsequently, a joint intensity-and-point based dissimilarity measure was minimized, solving both for rigid and nonrigid transformations. We showed that this registration approach combining geometrical information (lumen centerlines) and image information (US and MRI intensities) resulted in better registrations compared to intensity-only or point-only approaches. However, we also observed that even better registrations could be achieved if more geometrical information, such as carotid artery lumen segmentations, would be exploited.

In this work, we propose a novel automated method for registering US and MRI images of the carotid artery. The method is an extension of [20] and adds geometric information in the form of lumen segmentations, to improve registration performance. To this end, a novel customized dissimilarity measure that serves as an optimization objective during the registration is proposed. This dissimilarity measure is based on the difference between centerlines and lumen segmentations in 3D-US and MRI. Main advantages of our method compared to previous works are that it requires low user interaction (only three seed points per artery on each image modality), and our registration method does not rely directly on intensity information.

Our approach thus requires segmentation of the lumen both in 3D-US and MRI. Manual segmentation of the carotid lumen in 3D-US and MRI images is a time consuming and difficult process. US image segmentation is challenging owing to characteristics such as noise, shadows and speckles inside the lumen. Moreover, in situations where the US beam is parallel to the vessel wall, the wall is not clearly visible. This makes it difficult to differentiate the carotid artery lumen from other structures. To facilitate carotid lumen segmentation in 3D-US, several automatic and semi-automatic methods have been proposed [50, 63, 66, 101]. A semiautomatic method for carotid segmentation in 3D-US using level sets was presented by [101]. The segmentation results were good, however the method requires substantial user interaction as anchor points on transverse slices need to be selected which are intercepted by an evolving curve. Additionally, the method is limited to the segmentation of the common carotid artery. Another method that uses a level-set based approach for carotid artery segmentation was presented by [49]. This method also requires considerable user interaction to initialize boundary points for every slice. [63] proposed a very robust method to track

the arteries, however it is limited to generating circles per slice. In Chapter 4, we applied an optimal-surface graph method to segment the lumen in 3D-US. Good results were obtained on volunteer data, and fair results on patient data. Segmenting the lumen in MRI is easier compared to US because lumen contrast in MRI is generally good. However, it is also a time consuming process if performed manually. Several automatic methods to segment the lumen in MRI that achieved good results have been presented, e.g. [6, 45, 94]. In [94] a level-set evolution approach starting from an automatically detected centerline was used. [6] proposed an optimal-surface graph segmentation method which requires a coarse approximation of the lumen as initialization. Finally, in [45] a 3D deformable vessel model approach with a learning-based post-processing step was used.
In our US-MRI registration method, we choose to use lumen segmentation based on optimal surface graphs as presented for US in Chapter 4, and for MRI in Chapter 2. The method is described in detail in the Method section. For MRI, the segmentation method was already extensively evaluated in Chapter 2. For US, only a preliminary evaluation was presented in Chapter 4. In this work, we include a thorough evaluation of the US segmentation method, to assess its feasibility to use it as a reliable geometrical marker for image registration. The complete registration method is subsequently evaluated on 28 carotid artery data sets composed by volunteer and patient data.
To summarize, the contribution of this work is fourfold:

1. We present a complete framework for automated registration of 3D-US and MRI of the carotid arteries based on geometrical features.

2. A novel and customized dissimilarity measure that serves as optimization objective during image registration is proposed.

3. Quantitative results for the accuracy of automated lumen segmentation in US are reported.

4. The US-MRI registration method is evaluated on both volunteer and patient data, studying the effect of important design parameters, and comparing with several alternative methods.

5.2 Method

First, we describe the registration framework using centerlines and segmentations. Subsequently, we describe the automated lumen segmentation method which is used in our registration approach.

5.2.1 US-MRI Registration Framework

Multimodal image registration is performed using geometrical features extracted from the US image $I_U : \mathbb{Z}^3 \to \mathbb{R}$ and MRI $I_M : \mathbb{Z}^3 \to \mathbb{R}$. The registration aligns the features of a moving image to the features of a fixed image by applying geometrical transformations. These transformations can be rigid and/or nonrigid and are determined by

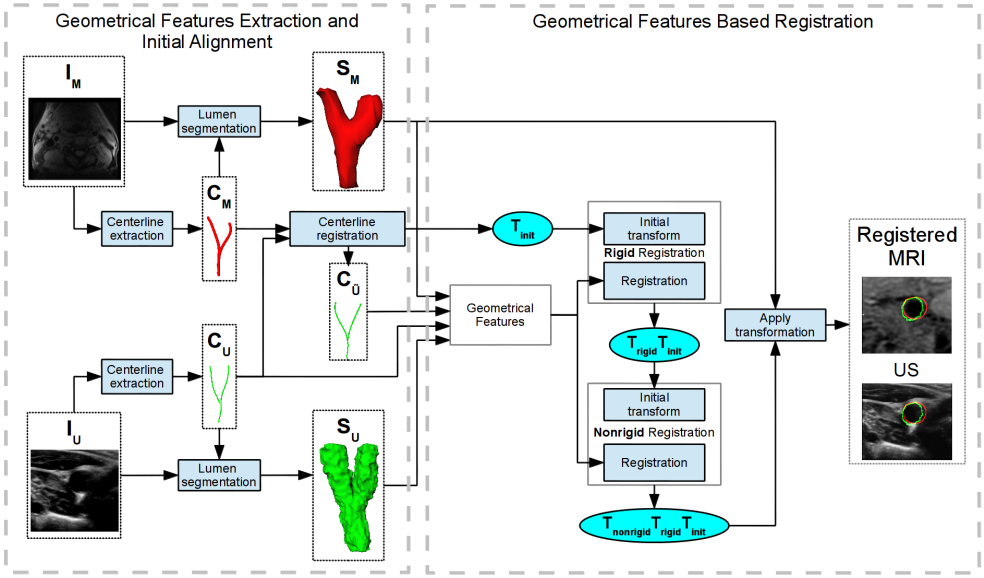

Figure 5.3. Flowchart with a schematic overview of the US and MRI registration steps.

optimizing a cost function, which estimates the dissimilarity between the features of the fixed image and the transformed moving image. In this work we choose I_U as the fixed image because of its higher resolution.
The lumen centerlines and the segmentations are extracted from each modality and serve as input features for the registration. In the first stage of the registration procedure, the centerlines are used to obtain an initial transformation ($\boldsymbol{T}_{init}$) to align the images. Subsequently, both the centerlines and the segmentations are employed in finding the optimal transformation. An overview of the method's steps is shown in Figure 5.3.

5.2.1.1 *Centerline Extraction*

The centerline in US is extracted with the method of [19, 20] and the centerline of MRI is extracted with the method of [95].
In the centerline extraction on US data, we assume that planar cross-sections of the lumen have elliptical shapes. The union of the center points of the ellipses in each cross-section results in the centerline. The ellipses are fitted to points on the lumen border. These border points are automatically detected by analyzing the intensity gradient magnitude in rays traced from a given seed point inside the lumen. The initial inputs of the algorithm are three seed points located at the Common Carotid Artery (CCA), External Carotid Artery (ECA), and Internal Carotid Artery (ICA). The algorithm seed point for the next planar cross-session is the center of the ellipse extracted from the previous planar cross-section.

The centerline in MRI is extracted by finding the minimum cost path between a seed point in the CCA and seed points in the ECA and ICA. This cost is computed based on a combination of a local intensity similarity metric and a medialness filter [41]. To avoid large deviations of the true vessel centerline in curved regions, a multi-planar reformatting is performed and the minimum cost path algorithm is iteratively applied. We denote the obtained centerlines as $C_U \subset \mathbb{R}^3$ (US centerline) and $C_M \subset \mathbb{R}^3$ (MRI centerline). The centerlines are used both for centerline registration and to initialize the lumen segmentations in US and MRI.

5.2.1.2 *Centerline Registration*

To obtain a robust initial alignment, first the centerlines C_U and C_M are registered. The steps for the centerline registration are the same as in [20] and are briefly summarized here for completeness.
Initially, the MRI and US centerlines are smoothed and resampled to a resolution of $0.1\,mm$ (slightly smaller than the voxel spacing of the US image data). Subsequently, reference points around the centerline bifurcation point are automatically selected in each centerline. A point-based rigid registration is performed with these pairs of corresponding landmarks. This point-based registration minimizes the root sum of squared Euclidean distances between corresponding points. The output transformation is called $\boldsymbol{T}_0$ and is applied to C_U. Following this registration, the point sets C_U and C_M are cropped automatically such that the maximum distances before/after the bifurcation in both sets are equal. This registration is followed by a rigid ICP registration between the centerlines, resulting in a second rigid transformation $\boldsymbol{T}_1$. Next, the centerlines are registered with a nonrigid registration. The nonrigid transformation is applied to the US centerline, yielding a deformed centerline $C_{\tilde{U}}$ which matches the original MRI centerline C_M.
The composition of transformations $\boldsymbol{T}_0$ and $\boldsymbol{T}_1$ is used to globally initialize the geometrical features based registration: $\boldsymbol{T}_{init} = \boldsymbol{T}_1(\boldsymbol{T}_0)$. The deformed centerline $C_{\tilde{U}}$ is used as a constraint in the registration.

5.2.1.3 *Geometrical Features Based Registration*

In this stage of the registration, alignment is performed using both centerlines and segmentations. For the lumen segmentations $S_U : \mathbb{R}^3 \to \{0,1\}$ and $S_M : \mathbb{R}^3 \to \{0,1\}$, we assume that some interpolation method is used to make this function valid for all $\mathbf{x} \in \mathbb{R}^3$, and not just at voxel center locations. The registration is performed by estimating a transformation $\boldsymbol{T}$, which minimizes a cost function. The geometrical features are registered with a rigid transformation $\boldsymbol{T}_{rigid}$ and/or a subsequent nonrigid transformation $\boldsymbol{T}_{nonrigid}$. The cost function $\mathcal{C}$ is a dissimilarity measure between (S_U) and (S_M), and between centerlines $C_{\tilde{U}}$ and C_U:

$$\mathcal{C}(\boldsymbol{T}) = \omega\mathcal{D}(S_U, W_{\boldsymbol{T}}(S_M)) + \mathcal{E}(\boldsymbol{T}(C_U), C_{\tilde{U}}). \tag{5.1}$$

This function is a weighted sum of the segmentation dissimilarity $\mathcal{D}$ and the Euclidean distance between centerlines C_U and $C_{\tilde{U}}$, denoted by $\mathcal{E}$. The term $W_{\boldsymbol{T}}$

represents an operator that warps S_M using coordinate transformation $\boldsymbol{T}$, i.e., $W_{\boldsymbol{T}}(S_M)(\mathbf{x}) = S_M(\boldsymbol{T}(\mathbf{x}))$. The chosen metric $\mathcal{D}$ is the sum of square differences. The Euclidean distance $\mathcal{E}$ between C_U and $C_{\tilde{U}}$ is used as a penalizer to prevent unfeasible transformations that may occur due to inconsistencies in the automated segmentations S_U and S_M. The term ω is a weighting factor.
To minimize $\mathcal{C}$, an adaptive stochastic gradient descent method was applied using 2000 image coordinates randomly selected in every iteration, as proposed by [54]. To model the nonrigid transformation, a B-spline parametrization [83] was used, with a control point spacing of β. In order to avoid local minima, a 3-level hierarchical strategy was employed: the amount of image Gaussian smoothing and β are gradually decreased by factors of 2. The geometrical features based registration was implemented using the open source Elastix software [55].

5.2.2 Optimal Surface Graph Method for Lumen Segmentation

The optimal surface graph method as proposed by [118] allows segmentation of multiple surfaces, while incorporating topology constraints and prior information on shape. The optimal-surface graph method aims to minimize a cost function defined as the sum of graph edge costs, which is achieved using a minimum cut. The graph $G = (V, E)$ is composed of vertices V and edges E. V includes the vertices associated with positions in the image, and the vertices s and t which denote the source and sink points of the graph. The edges E connect the vertices of the graph, and represent the association strength between vertices. Edges that connect vertices from the same region are associated with high costs, whereas vertices connecting different regions are associated with low costs. The segmentation solution is defined by the minimum cut that separates the graph in two parts: source part $V_s \subseteq V$ (foreground region) and sink part $V_t \subseteq V$ (background region), such that $V_t = V \backslash V_s, s \in V_s, t \in V_t$. The minimum cut minimizes the total cost of the edges that are being cut [52], and is found by applying a min-cut/max-flow optimization algorithm [17].
We use the graph construction approach as presented in Chapter 4 and Chapter 2 to segment the lumen in 3D-US and MRI. The graph is constructed starting from a coarse initial segmentation of the lumen as depicted in Figure 5.4. The coarse initial segmentation is obtained by a $2\,mm$ radius spherical dilation of the automatically extracted centerline. The vertices are grouped by non-intersecting graph columns starting from this initial segmentation. These non-intersecting graph columns enable the segmentation of high curvature areas [76]. Non-intersecting graph columns are guaranteed if these are defined on the trajectory of flow lines obtained by Gaussian smoothing (with scale σ) the coarse initial segmentation, see Figure 5.4. Given the flow lines $\boldsymbol{f}_i : \mathbb{Z} \rightarrow \mathbb{R}^3$ where $i \in \{1, ..., Q\}$ with Q the number of voxels on the initial segmentation's surface, the graph vertex $v_{i,k} \in V$ is associated with the image position $\boldsymbol{f}_i(k)$. The graph columns are defined by the set of vertices $V_i = \{\, v_{i,k} |\, k = -I_i, -I_i + 1, \ldots, O_i - 1, O_i\}$ where the uniform separation distance between vertices is given by $\delta = \|\boldsymbol{f}_i(k+1) - \boldsymbol{f}_i(k)\|$. Here $v_{i,-I_i}$ and v_{i,O_i} represent the innermost and outermost vertices of column V_i, and $v_{i,0}$ is at the initialization

surface. Several edges are defined in the graph. First, the edges $v_{i,k} \overset{w_{i,k}}{\rightarrow} v_{i,k+1}$ within a graph column indicate the relation between foreground and background such that $w_{i,k}$ should be as low as possible at the position of the surface. Second, the smoothing penalty edges between neighboring graph columns, $v_{i,k} \overset{p}{\leftrightarrow} v_{j,k}$, penalize each vertex displacement in the graph cut by a value p. Third, the topological constraint edges within a graph column, $v_{i,k+1} \overset{\infty}{\rightarrow} v_{i,k}$, guarantee that the graph columns are cut only once. Finally, the vertex s is connected to all innermost vertices, and t to all outermost vertices. The graph construction approach is illustrated in Figure 5.4.

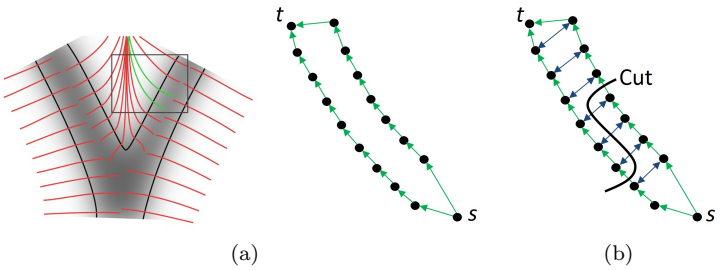

Figure 5.4. Graph construction method [66]. The non-intersecting graph columns starting from the coarse initial segmentation (gray sketch) are depicted by red curves in (a). Two graph columns are selected, depicted by green curves, to show their vertices (black dots) and intra-column edges (green arrows) in (a). The smoothing penalty edges between neighboring columns are depicted by blue arrows in (b). Additionally, an example of a graph cut is shown in (b).

To achieve a minimum value for $w_{i,k}$ at likely positions of the lumen boundary, this cost is inversely proportional to the first order derivative of the image intensity along the graph column trajectory $\boldsymbol{f}_i$. To make small adjustments to the position of the minimum (mainly caused by partial volume effects), the second order derivative is added. Thus, the edge cost $w_{i,k}$ is defined by:

$$w_{i,k} \propto \left| \alpha \frac{\partial^2 I(\boldsymbol{f}(k))}{\partial k^2} + (1 - |\alpha|) \frac{\partial I(\boldsymbol{f}_i(k))}{\partial k} \right|^{-1}, \tag{5.2}$$

where $I(\boldsymbol{f}_i(k))$ is the image intensity at the position $\boldsymbol{f}_i(k)$, and $\alpha \in [-1, 1]$ is a parameter that weights the contribution of the second derivative term.

Since the initial coarse segmentation may contain irregularities, and may be too far from the true lumen boundary, the estimated optimal surface may contain errors. To address this, the optimal surface graph method is iterated N times. The result of iteration n is used to create a new graph in iteration $n + 1$.

This segmentation method is applied to both US and MRI. C_U and C_M are the centerlines used for initialization, and S_U and S_M are the final outputs. These automatic segmentations are used jointly with the centerlines in the registration framework as explained in Section Geometrical Features Based Registration.

5.3 Experiments

5.3.1 Data

We evaluated our method on data from 8 patients and 6 healthy volunteers. The patients were selected within the scope of the Plaque At Risk (PARISK) study [97]. The PARISK study is a prospective multicenter cohort study of patients with recent neurological symptoms due to ischemia in the carotid artery with ipsilateral carotid artery stenosis ($< 70\%$) who are not scheduled for carotid endarterectomy or stenting [97]. Volunteers were healthy and had no plaque. Left and right carotid were scanned in all subjects.

The US images were acquired with the Philips probe L9-3 and a Philips iU22 system (Philips Medical Systems, Bothell, WA, USA). The probe signal was adjusted to $4cm$ depth for 4 patients and to $3cm$ depth for 4 patients and 6 volunteers. Each US examination generates a stack of transversal 2D images. To obtain the 3D-US images, we used the Stradwin software [37] that correlates the 2D images to the position of a magnetic sensor attached to the US probe. After exporting the data to a volumetric representation, the voxels dimensions are $0.16 \times 0.16 \times 0.16\,mm^3$ for a probe depth of 3cm, and $0.21 \times 0.21 \times 0.21\,mm^3$ for a depth of 4cm.

The patient MRI data were acquired on a $3.0T$ GE Medical Systems Discovery MR750 (GE Healthcare, Milwaukee, Wisconsin, USA), using a T2-weighted double inversion recovery fast spin echo (T2w-DIR-FSE) black-blood sequence. The original voxel spacing of MRI on the patient data was $0.55 \times 0.55 \times 2.0\,mm^3$. Initial experiments indicated that the lumen centerline extraction method failed in these images due to the anisotropic voxels. Therefore, we resampled the MRI with a cubic B-spline interpolation leading to isotropic voxels with spacing $0.55 \times 0.55 \times 0.55\,mm^3$. For the volunteer data, the images were acquired using a $1.5T$ GE Medical System Signa Excite MRI machine (GE Healthcare, Milwaukee, Wisconsin, USA) with a proton-density-weighted fast spin echo (PDw-FSE) black-blood sequence with voxel spacing of $0.5 \times 0.5 \times 0.9\,mm^3$. Since these voxels were almost isotropic already, no resampling was necessary.

The Institutional Ethics Committee approved the study protocol, and all study participants provided informed consent.

5.3.2 Evaluation of MRI Lumen Segmentation

Lumen segmentation in MRI using the optimal-surface graph cut method was already extensively evaluated in Chapter 2 on similar MRI data as used in the current study. Therefore, we used the optimized segmentation parameters from Chapter 2. Prior to segmentation, the N4 bias field correction method [100] was employed to correct for MRI intensity inhomogeneities within the neck area.

The software tool for lumen segmentations was implemented in C++ using Linux operative system.

5.3.3 Evaluation of US Lumen Segmentation

Since in Chapter 4 only a preliminary evaluation of the US segmentation method was presented, we performed a cross-validation experiment to establish the optimum parameter settings on data independent of the test set. Since left and right carotids of a single subject may have similar characteristics, a leave-two-out cross-validation design was used, in which we left both vessels of a subject out of the training set. On the training set, the optimum parameter settings were determined by exhaustive grid search. As an evaluation criterion, we used the Mean Surface Distances (MSD) (averaged over all carotids in the training set) between the resulting segmentations and the manual segmentations. The manual segmentations were performed by annotating the lumen at each five to ten 2D slices of each US image sequence. Thereafter, the lumen surface was interpolated based on these contours. The evaluated parameters of the method were: σ, α, p, and N. The vertex distance δ was fixed to the minimum voxel spacing. In the optimization step, we considered the following range of parameters: $\sigma \in \{20, 30, 40\}$, $\alpha \in \{-1.0, -0.5, 0.0, 0.5, 1.0\}$, $p \in \{1000, 10000, 25000, 50000, 75000, 100000\}$,
and $N \in \{1, 2, 3, 4, 5\}$.
The entire 4D search space was evaluated and the selected optimum parameter configuration in each leave-two-out fold was used to segment the left subject. The resulting segmentations S_U were used in further registration experiments.
In order to visualize the impact of each parameter on the segmentation results, we chose the most frequently selected parameter configuration as a base configuration and individually varied one of the parameters while computing the MSD on the entire dataset. Thus obtained MSD values are slightly overtrained, but are useful to gain insight in the effect of each parameter.

5.3.4 Evaluation of Registration Accuracy

On these experiments we evaluated the registration accuracy and compared the results with existing methods. First, the effect of important registration parameters were investigated. We tested both rigid, and the combination of rigid and nonrigid registration (in the rest of the chapter we call this combination only as nonrigid registration). As in [20], for the B-spline transformation model in the nonrigid registration, we tested isotropic grid spacings (mm) $\beta \in \{8, 16, 32\}$. For the weighting value that balances the $\mathcal{D}$ and $\mathcal{E}$ cost function terms, we tested $\omega \in \{1, 2, 4, 8, 16\}$. The MSD between the manual US segmentation and the transformed automatic MRI segmentation was used as a measure of registration accuracy. The combination of β and ω that yielded highest accuracy was used in all further evaluations. Second, we compared the proposed registration to three other methods. We adopt the acronym GEO to refer to our registration method based on geometrical features. The other methods were:

- Initial: Registration obtained with the transformation T_{init} which uses only the centerlines.

- IP: Intensity-and-point based registration [20].

- MAX: Registrations performed between the manual US segmentation and the automated MRI segmentation. Since exactly these segmentations are used to compute the MSD for evaluation, this "overtrained" method will indicate what is the maximum achievable accuracy of any registration method [20].

The parameters β used in the methods IP and MAX were selected according to their best values defined in [20]. As IP only use centerlines as geometrical features and MAX the lumen segmentations, a weighting parameter ω in the dissimilarity cost is not required. For IP we used $\beta = 32\,mm$ and on MAX $\beta = 8\,mm$.
All registration methods were implemented using the open source Elastix software [55].

5.4 Results

5.4.1 US Lumen Segmentation Results

Table 5.1 shows the result of the leave-two-out evaluation for the US segmentation experiments. In this table, it can be observed that the most frequent best configuration was $\sigma = 40, \alpha = 0.0, p = 50000, N = 3$, since the best MSD was obtained with this configuration in 11 out of the 14 subjects. Figure 5.5 summarizes the segmentation results from the leave-two-out evaluation for the 28 carotids. The median error is around $0.6\,mm$.

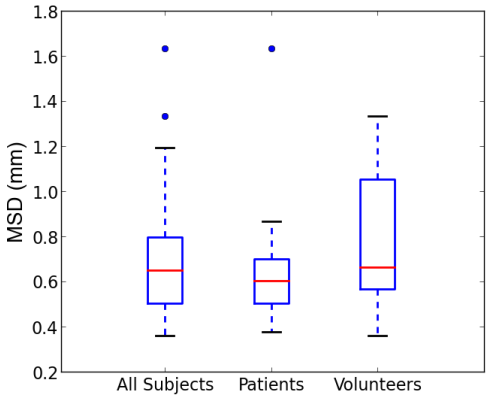

Figure 5.5. Segmentation results obtained in leave-two-out cross-validation. Results are reported for the entire test set, and separately for the patient and volunteer subsets.

To visualize the impact of each parameter on the segmentation results, we chose the most frequently selected parameter configuration as a base configuration and individually varied one of the parameters while computing the MSD on the entire dataset. The effect of each parameter on the segmentation accuracy can be seen in

Subject	σ	α	p	N	Train MSD (mm)	Test MSD (mm) Left	Right
P1	40	0	50000	3	0.68 ± 0.24	0.38	0.87
P2	30	0	50000	3	0.69 ± 0.24	0.69	0.49
P3	40	0	50000	3	0.69 ± 0.24	0.51	0.65
P4	40	0	50000	3	0.68 ± 0.25	0.60	0.79
P5	40	0	50000	3	0.69 ± 0.24	0.44	0.71
P6	40	0	50000	3	0.69 ± 0.24	0.55	0.61
P7	40	0	50000	3	0.69 ± 0.24	0.52	0.50
P8	20	0	50000	2	0.66 ± 0.19	0.81	1.63
V1	40	0	50000	3	0.70 ± 0.23	0.49	0.36
V2	40	0	50000	3	0.64 ± 0.19	1.34	1.05
V3	40	0	50000	3	0.69 ± 0.24	0.46	0.67
V4	40	0	50000	3	0.68 ± 0.25	0.65	0.67
V5	30	0	50000	3	0.65 ± 0.21	1.06	1.19
V6	40	0	50000	3	0.67 ± 0.25	0.72	0.78

Table 5.1. Results of leave-two-out cross-validation of the US lumen segmentation provided for each held-out subject. The optimum parameters based on the training set are provided for each patient (P#) and volunteer (V#). MSD (average±std.dev.) on the training set, and the MSD on the left and right carotid of the left-out subject are listed.

Figure 5.6. The smoothness parameter σ had a small effect on the end results. The parameters p and α showed a clear minimum within the selected range. A value of $\alpha = 0$ means that the edge is sharp so only the first derivative suffices to localize it. The improvement caused by the number of iterations N peaked at 3 iterations (see Figure 5.7 for an illustration).

5.4.2 Registration Results

Figure 5.8 shows the registration accuracy on the 28 carotids for different values of β and ω. Nonrigid registrations using higher β always improved the registrations accuracy, so more freedom of deformation did not result in better registrations. Additionally, $\beta = 32mm$ generally outperformed rigid registration, except for $\omega = 1$. For higher ω, we observed more accurate nonrigid registrations, which stabilized after $\omega = 4$. This means that giving more weight to the segmentations results in better registrations. However, this behavior was not observed using rigid registration. The best parameter configuration for the registration using geometrical features was $\beta = 32mm$ and $\omega = 16$.

The results for all subjects obtained with Initial, MAX, IP and GEO are shown in Figure 5.9. The results of MAX, IP, and GEO are shown both after the rigid and after the nonrigid registration stage. The figure shows that the complete GEO considerably improves the results compared to Initial; also a improvement compared

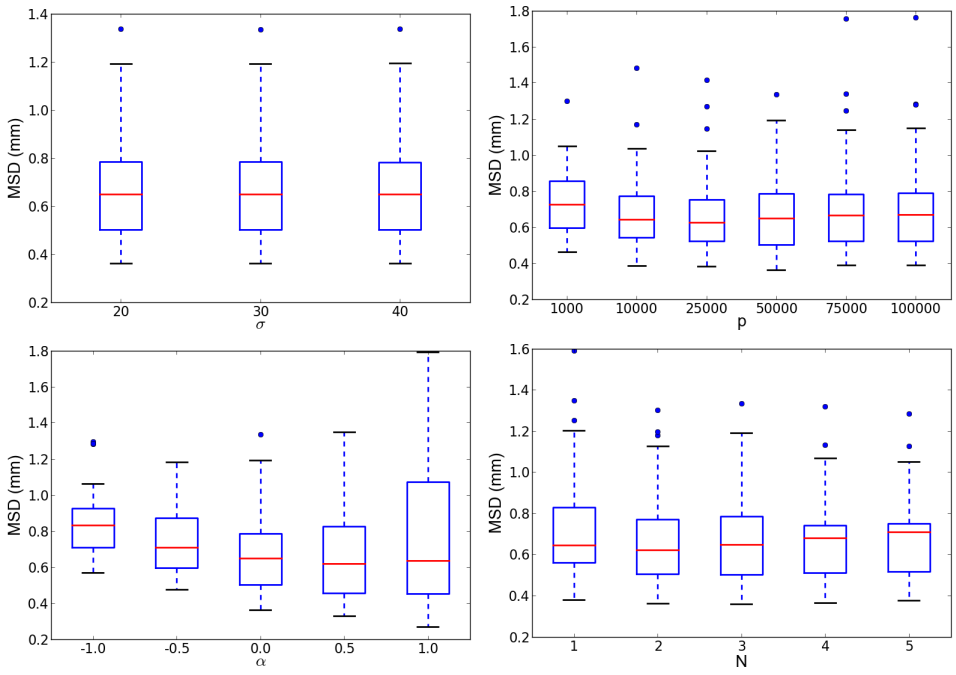

Figure 5.6. Effect of the segmentation parameters on segmentation MSD, when varying a single parameter while the other parameters are fixed at the most frequent configuration during training ($\sigma = 40, \alpha = 0.0, p = 50000, N = 3$). The tested parameters were: the smoothing scaling σ, the weighting parameter α, the edge capacity p, and the number of iterations N.

to IP is observed. As expected the nonrigid MAX method outperforms all other methods. The rigid MAX method (which is less prone to overfitting than nonrigid MAX) scored similar MSD as the proposed nonrigid GEO method.

Table 5.2 shows the numerical results corresponding to Figure 5.9 for the complete data set, and for the volunteer and patient sets separately. For MAX, IP, and GEO, the results of nonrigid registration are shown. The table confirms that GEO outperforms IP on the entire test set, and shows that this is also the case when considering the volunteer set and patient set separately. Using a Wilcoxon test on the entire test set, it was confirmed that the difference in MSD values between GEO and IP was statistically significant ($p < 0.01$).

Figure 5.10 shows comparison between manual segmented volumes in US, and the registered MRI segmented volumes. In Figure 5.11 planar sections of US and the registered MRI with overlaying segmentation contours are shown.

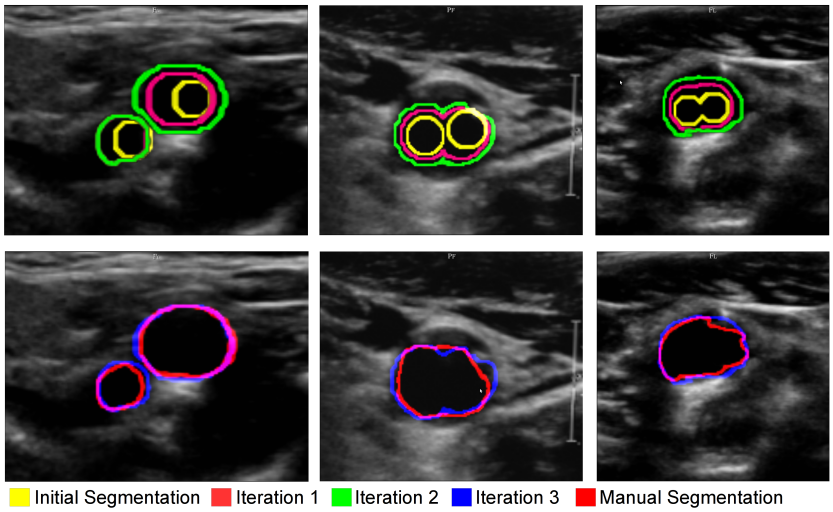

Figure 5.7. Segmentation results using the presented method on US for iterations $n = 1...3$. Left to right: three example slices.

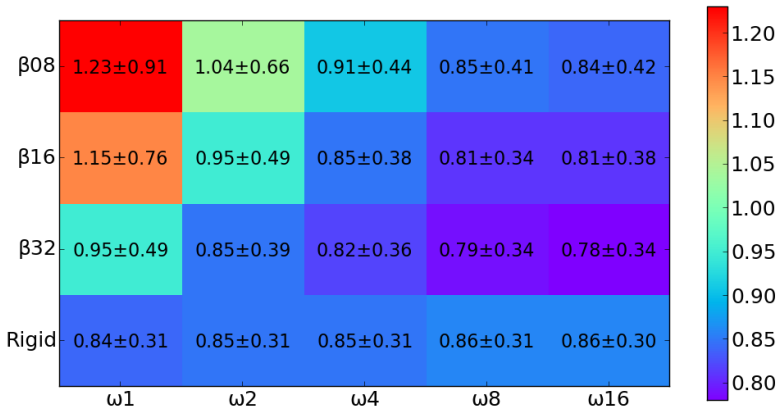

Figure 5.8. Registration MSD errors (mm) for various settings.

5.5 Discussion

In this work, we presented a method to register US and MRI of the carotid artery using geometrical features. As features, semi-automatically extracted lumen centerlines and

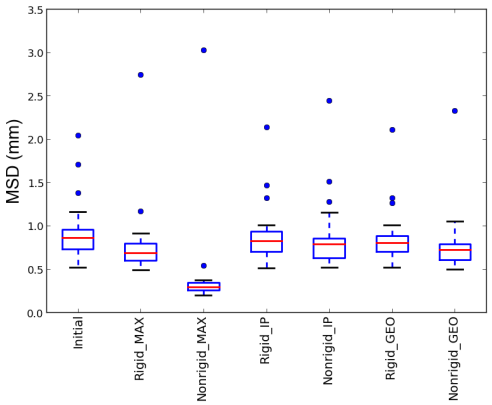

Figure 5.9. Registration MSD errors (mm) using the methods: Initial, GEO, IP, and MAX. Results are reported both for rigid and nonrigid registrations.

Method	All subjects	Volunteers	Patients
Initial	0.92±0.32	0.80±0.17	1.02±0.38
GEO	0.78±0.34	0.65±0.09	0.87±0.42
IP	0.85±0.39	0.72±0.20	0.95±0.46
MAX	0.39±0.53	0.28±0.05	0.48±0.68

Table 5.2. MSD (mm) between manual US segmentations and MRI registered segmentations for four different registration methods. The results are reported for volunteers, patients and all subjects combined.

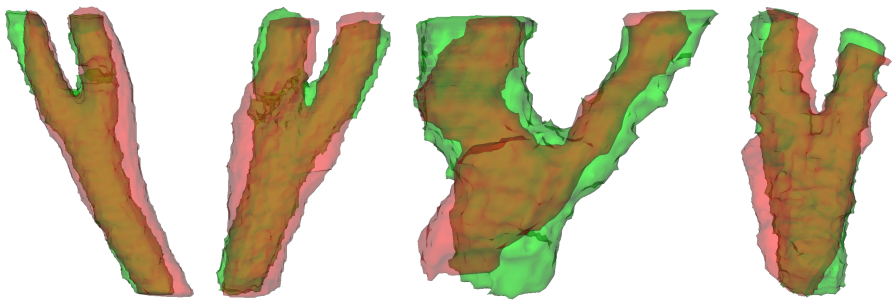

Figure 5.10. Comparison between manual US segmentations (red) and registered MRI segmentations (green), for registration based on geometrical features.

automatic lumen segmentations are used. The method was evaluated in a dataset composed of volunteer and patient data yielding good and robust results. The average MSD of the presented method was significantly lower than the results obtained by the

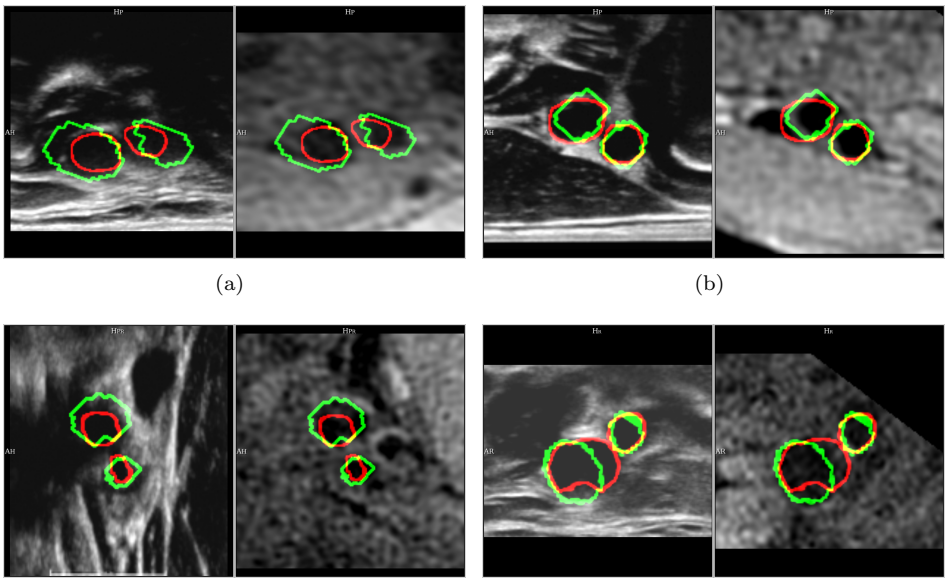

(a) (b)

(c) (d)

Figure 5.11. Side-by-side visualization US image (left) and registered MRI using geometrical features registration (right). MRI registered segmentations and manual US segmentations are depicted by green and red contours respectively. Figures (a) and (b) represent carotid arteries of volunteers and figures (c) and (d) carotid arteries of patients.

intensity-and-point based registration method presented in [20], and the registration using only the centerlines.

Although the automated US lumen segmentation method was extensively evaluated and proved to be an important input to the registration framework, the MSD was in the order of $0.6\,mm$. This suggests that there is still room for improvement in segmentation accuracy. In the segmentation results, we observed that the median MSD was slightly lower for patients than volunteers, which can be explained because the number of patients used for training was larger in the cross-validation experiments, so the parameters of the segmentation method are biased to the patient lumen geometry. Furthermore, the registration results show the importance of the segmentations in the registration framework, as we observed better registrations when giving higher weight to the dissimilarity between US and MRI segmentations. However, we also observed that this weight reached a peak where further increase did not improve the registrations. This could suggest that this weight is bounded by the quality of the segmentations. In addition, we also observed better registrations using the manual segmentations in MAX. Therefore, an improvement in the automatic lumen segmentation will further increase the registration accuracy. However, it is important to notice that the same manual segmentation used for the registration in MAX was used for evaluation, leading to a bias.

Apart from [20], other methods to register the carotid artery between MRI and US [24,43,72,91] present higher or similar errors to the reported in the presented method, although the data is different and the registration error metric implementation may slightly differ. Additionally, most of these methods require more user interaction. First, [91], which presented a fully automatic registration method based on a rigid registration model using mutual information, reported an average of $0.32 \pm 0.3\,mm$ displacement for four points in five arteries from five patients. Although this result seems promising, the data set and the number of points for evaluation are small, which makes it difficult to assess the quality of the method. [72] presented a semi-automatic non-rigid registration model where the twisting and bending of the neck is introduced in the model. They obtained $1.5 \pm 0.4\,mm$ surface distance error based on manual annotated contours from twelve arteries from six patients using a similar MRI protocol. This surface distance error is higher to the MSD we obtained for patients ($0.87 \pm 0.42mm$). Subsequently, [24] presented a method which requires a considerable amount of user interaction based on surface registration. They reported about $1\,mm$ MSD error, which is comparable to our results although we require less user interaction. Finally, [43] presented a similar method to our work based on the registration of the centerlines and segmentations. They reported surface errors around 1.2mm on a data set composed of six healthy volunteers and five patients. This error is slightly higher than our result. Additionally, our method segments both 3D-US and MRI automatically, while in [43] this is not the case.
The proposed method is largely automated but still demands minimal user interaction. For the lumen centerline detection, the user must select a point in each of three branches of the carotid artery in US and MRI data. The difficulty in implementing a fully automated method for identifying the carotid branches is related to the presence of structures with a similar shape and intensity, such as the jugular vein. In future work, it would be interesting to develop a robust algorithm able to automatically identify the carotid branches in US and MRI; this would fully automate the registration framework.

5.6 Conclusion

We proposed a method to automatically register US and MR images of the carotid artery. The registration framework is based on geometrical features, namely the artery centerlines and lumen segmentations, which are semi-automatically extracted from the US and MR images. The method requires minimal user interaction. Experiments on 28 carotids from 8 patients and 6 volunteers demonstrate good and robust performance. Compared to our previous intensity-and-point based registration method [20], registration accuracy was improved significantly. The use of automated segmentations combined with centerlines leads to a high registration accuracy, thus paving the way for comprehensive multimodal analysis of atherosclerotic plaque in the carotid artery.

Chapter Six

Cooperative Carotid Artery Centerline Extraction in MRI

Abstract — Centerline extraction of the carotid artery in MRI is important to analyze the artery geometry and as an input for further processing including registration and segmentation. The centerline of the artery bifurcation is often extracted as two independent minimum cost paths leading from the common to the internal and the external carotid artery. Often the cost is not well defined at the artery bifurcation, leading to centerline errors. To solve this problem, we developed a method to cooperatively extract both centerlines, where in the cost to extract each, we integrate a constraint region derived from the estimated position of the neighbor centerline. This method avoids both centerlines following the same cheapest path after the bifurcation, which is a common error when these are extracted independently. We show that this method results in less error compared to extracting them independently: 10 failed centerlines vs. 3 failures in a data set of 161 arteries with manual annotations. Additionally, we show the new method to improve the non-cooperative approach in 28 cases ($p < 0.0001$) in a data set of 3,904 arteries.

Based upon: Andrs M. Arias-Lorza, Daniel Bos, Aad van der Lugt, and Marleen de Bruijne, "Cooperative Carotid Artery Centerline Extraction in MRI", *submitted*.

6.1 Introduction

Centerline detection of the carotid artery in MRI is important to analyze its geometry [94], and as input for segmentation [6, 45, 94] and registration methods of the carotid artery [21, 111].

There are two main type of approaches to extract vessel centerlines using different image modalities: global optimization methods based on minimum cost paths, and local approaches [85]. Local methods include tracing medial axis from inscribed disks or spheres [4, 19], finding the centers of intensity ridge traversals [7, 10], and localizing local maxima from filter outputs [41, 79].

As minimum cost paths methods are based on global optimizations, they could result in robust centerlines [27, 28, 42, 94, 116]. Often the carotid artery centerline is detected as two independent paths [19, 46, 94], one for each of the two arteries that separate from the Common Carotid Artery (CCA) at the bifurcation. These two arteries are the Internal Carotid Artery (ICA) and the External Carotid Artery (ECA). Using minimum cost path approaches, each path is defined as the minimum cost path between two points, where the cost is the output of a function that should be low at the center of the artery and high elsewhere. In this chapter, the centerlines are represented as minimum cost paths. There are two main techniques to find the minimum cost paths: graph approaches (Dijkstra algorithm [32], A* and F* algorithms [34]) and continuum approach (fast marching [88]). In this work we use fast marching as it suffers less from metrication errors [25], and it is possible to consider the anisotropic characteristic of the MRI images [12, 88].

Defining a good cost function is a difficult task especially at the bifurcation. Generally, this cost at each image position is a function of the intensity and/or the surrounding shape [27, 28, 42, 85, 94, 116], where the surrounding shape is estimated using Hessian eigen-analysis or medialness filters [35, 41]. However the intensity inside the artery presents a complex distribution along the vessel which is affected by artifacts, also surrounding structures may have similar intensity. Additionally vessel detector filters based on Hessian or medialness filters mainly work well on cylindrical shape structures. This can cause the centerline to present errors especially at the bifurcation, where the shape is not cylindrical. A common problem in carotid centerline extraction from MRI is that the centerline traced from either ICA or ECA jumps to the more clearly visible artery. An example is given in Figure 6.1.

To solve this problem, better cost functions that make use of features that describe well the artery shape and the intensities distribution inside the artery could be defined. Another solution can be to define a cost function that takes the anatomy and geometry of both arteries (ICA and ECA) into account. This could potentially prevent errors as shown in Figure 6.1. In this chapter, we propose a method to cooperatively extract both ICA and ECA centerlines where the cost at each path considers the geometry of the neighbor artery.

The problem of jointly extracting multiple centerlines has been addressed before in medical imaging. In [122] a method to track the centerlines of abdominal vessels in 3D ultrasound is presented. They use several manually annotated points at the common, bifurcation, and at the bifurcated vessels; then the points are connected by straight lines which start an active contour evolution (snake) leading to the centerlines. This

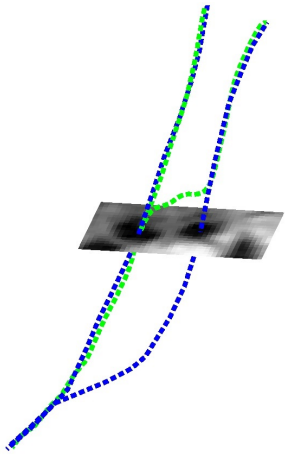

Figure 6.1. Centerline detection at the carotid artery by finding two independent minimum cost paths. The blue curves represent the manually annotated centerlines, and the green curves are the automatically detected centerlines. The centerlines are overlaying an MRI cross-section.

is an interesting approach and may work well if the initialization represented by the connected straight lines is inside the artery. However in many curved vessels the straight lines could be outside the artery. Other methods find rough segmentations of all the vessels of interest, and subsequently a skeletonization results in the centerlines [112]. This method may work if the segmentation is relatively accurate. However, the segmentation of the carotid artery in MRI is difficult and generally requires elaborated methods that use initializations based on centerlines [6, 45, 94]. Another method is [121], which obtains a complete tree of vessel centerlines by matching appearance models based on fitting cylindrical patterns. This is an interesting method as it is fully automatic; however they reported errors at the bifurcation for complex shapes.

Joint extraction of several minimum cost paths has been addressed before for multiple path planning where interaction and constraints in the paths are considered [9,13,96]. We find especially interesting the method presented in [96] where the cost of each path is defined by the path distance to the target and a constraint around the neighbor paths. This principle could be used to find multiple centerlines where the cost of the paths is a combination of the traditional cost based on intensity and shape features, and a constraint around the neighbor centerline. This should prevent the centerlines following the same paths either at the ICA or ECA as described in Figure 6.1 leading to more accurate centerlines at the bifurcation.

In this chapter, we use a similar approach to find carotid artery centerlines as in [96]. We define the centerlines as minimum cost paths where a constraint around the neighbor path is included. The cost is defined similarly to [94]. Further we solve the minimum cost paths using anisotropic fast marching as in [12] to consider the inherent anisotropic characteristics of MRI. Smoothness is also enforced by constraining the length of the path as in [25]. To evaluate the method, we compare the automatically

extracted centerlines to manually annotated centerlines in a data set of 161 arteries. In a large data set of 3904 arteries where manually annotated centerlines are not available, visual inspection of the results were performed in all cases where the conventional and proposed approach yield different results.

6.2 Method

First we describe how to obtain a representative cost image using only image information. Subsequently, we describe the anisotropic fast marching to extract minimum cost paths. Finally, we present the cooperative centerline extraction method which includes in the cost a constraint region derived from the likely position of the neighbor centerline.

6.2.1 Method overview

1. Obtain cost image which is low at the center of the artery and high elsewhere.
2. From seed points at CCA, ICA, ECA, and the bifurcation, apply anisotropic fast marching to get minimum cost paths between points.
3. As the paths may coincide after the artery bifurcation, we apply the new cooperative centerline extraction method to force the centerlines to follow different paths beyond the bifurcation.

6.2.2 Cost image

In [94] the cost is defined by a combination of the inverse of a multi-scale medialness filtering $m : \mathbb{R}^3 \to [0, 1]$ [41] and inverse of artery lumen intensity similarity $s : \mathbb{R}^3 \to [0, 1]$ [94]. The medialness filter gives a high output at the center of circular shapes, while the lumen intensity similarity metric is high when the intensity is similar to the mean intensity inside a Region Of Interest (ROI) around the set of seed points. These ROIs are spheres centered at the seed points with radius of $3.5\,mm$ for the CCA, and $2.5\,mm$ for ICA and ECA. As in [94] the cost function at voxel position $\mathbf{x}$ is given by:

$$p(\mathbf{x}) = \frac{1}{\epsilon + m(\mathbf{x})^{\alpha} s(\mathbf{x})^{\beta}}, \tag{6.1}$$

where ϵ is a small positive value to prevent singularities, and the parameters α and β control the contribution of the medialness filter and the lumen similarity metric. In the case of multispectral MRI, the maximum output of the medialness and the intensity similarity terms over the different MR sequences is taken to compute p.

6.2.3 Minimum cost path using anisotropic fast marching

Given the cost image p, the minimum cost path $C^* : \mathbb{R} \to \mathbb{R}^3$ between two points is defined as the path C minimizing the total accumulated cost. In the continuous space the total accumulated cost by the path is defined by:

$$\int_C (p(C(s)) + \omega)\, ds = \int_C \tilde{p}(C(s))ds, \tag{6.2}$$

where s is the arc-length parameter. As in [25] to enforce smoothness in the path, a constant ω is added to p. By this, the maximum path curvature is inversely proportional to ω [25].
To minimize Eq. 6.2, first the minimal action map $U : \mathbb{R}^3 \rightarrow \mathbb{R}$ associated to the starting point $\mathbf{p}_0 \in \mathbb{R}^3$ has to be defined. This minimal action map is defined as the minimum total cost to reach each point in the map, which satisfies the Eikonal equation represented by:

$$\|\nabla U(\mathbf{x})\| = \tilde{p}(\mathbf{x}), \tag{6.3}$$

where $U(\mathbf{p}_0) = 0$. Subsequently, after having the minimal action map U, the minimum cost path C^* between $\mathbf{p}_0$ and the end point $\mathbf{p}_1 \in \mathbb{R}^3$ is obtained by backtracking the vector field $\nabla U(\mathbf{x})$ from $\mathbf{p}_1$ to $\mathbf{p}_0$.
Fast marching [88] is a numerical method to efficiently solve Eq. 6.3 in the image space. As the images we use are 3D anisotropic MRI images, we use the 3D anisotropic fast marching algorithm based on [12]. Here $U(\mathbf{x})$ is the solution to the quadratic numerical approximation of Eq. 6.3 given by:

$$\sum_{i=\{x,y,z\}} \left(\frac{\max\{(U(\mathbf{x}) - U(\mathbf{x}^{-d_i})), (U(\mathbf{x}) - U(\mathbf{x}^{+d_i})), 0\}}{h_i} \right)^2 = \tilde{p}(\mathbf{x})^2, \tag{6.4}$$

where $\mathbf{x}^{d_i}$ is the displacement of position $\mathbf{x}$ by one voxel in the i-direction, and h_i is the voxel size in dimension i. U is approximated using Eq. 6.4 starting from $\mathbf{p}_0$ to $\mathbf{p}_1$ using a front propagation. To achieve this front propagation a controlled marching approach is used where every voxel position $\mathbf{x}$ is moving from three different sets: ALIVE: point for which U has been computed and frozen; TRIAL: point for which U has been estimated but not frozen; and FAR: point for which U is unknown. The method starts by including $\mathbf{p}_0$ in ALIVE, and assigning FAR the rest of points in the image. Then, in TRIAL are assigned the neighbor points of ALIVE belonging to FAR. In our case we use a 6-connected neighborhood. Then, U is estimated for the points in TRIAL. Further, in ALIVE is assigned the point in TRIAL with the lowest value of U. These steps are iterated until $\mathbf{p}_1 \in ALIVE$.
Subsequently, the minimum cost path is obtained by backtracking $\nabla U(\mathbf{x})$. To make the procedure more stable to noise, the vector field is normalized by: $\nabla U(\mathbf{x})_N = \nabla U(\mathbf{x})/\|\nabla U(\mathbf{x})\|$. $\nabla U(\mathbf{x})_N$ is set to zero in non-alive positions, then they do not affect the tracking. This backtracking is done by approximating the differential equation: $\partial C^*/\partial s = -\nabla U(C^*)_N$, where $C^*(0) = \mathbf{p}_1$. This approximation is obtained using the fourth order Runge-Kutta method with a step size δ resulting in the optimal path $C_{\mathbf{p}_0,\mathbf{p}_1} : \mathbb{R} \rightarrow \mathbb{R}^3$. In the rest of the chapter we call the resulting centerline after applying Anisotropic Fast Marching (AFM) from $\mathbf{p}_0$ to $\mathbf{p}_1$ using cost $\tilde{p}$ as the result of the function AFM: $C_{\mathbf{p}_0,\mathbf{p}_1} = AFM(\tilde{p}, \mathbf{p}_0, \mathbf{p}_1)$.

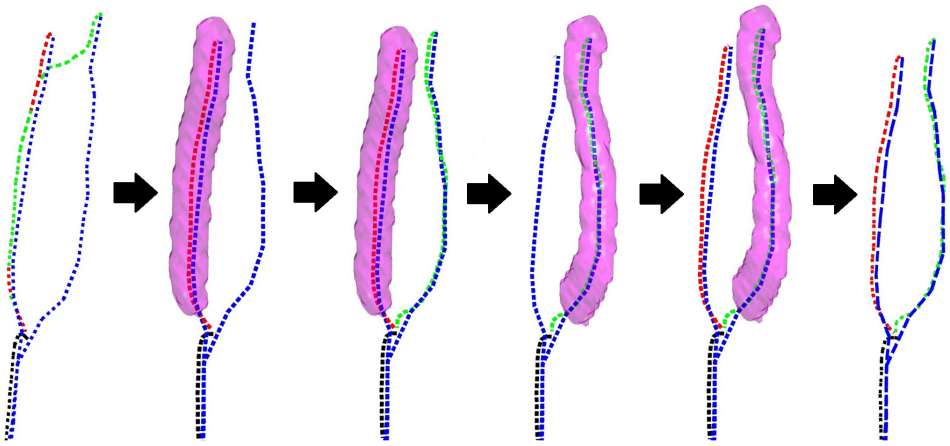

Figure 6.2. Schematic showing the cooperative centerline extraction method. Blue curves are the manually annotated centerlines; while black, red, and green curves are the automatic paths at CCA, ICA, and ECA respectively. First, the automatic paths are obtained using anisotropic fast marching, however the ICA and ECA erroneously follow the same path after the bifurcation. To fix this, a constraint region, shown by the purple surface, is constructed around the best path given by the red curve. Using this constraint, a new path is computed for ECA. Subsequently, a new constraint region is built around this new path. Then the path at ICA is computed again. Finally, both paths at ICA and ECA do not intersect and are close to the manually annotated ones.

6.2.4 Cooperative centerline extraction

From three seed points $\mathbf{A}$, $\mathbf{B}$, and $\mathbf{C}$, we get two minimum cost paths on $\tilde{p}$ using $AFM : \mathbf{A} \rightarrow \mathbf{B}$ ($C_{\mathbf{A},\mathbf{B}} = AFM(\tilde{p}, \mathbf{A}, \mathbf{B})$) and $\mathbf{A} \rightarrow \mathbf{C}$ ($C_{\mathbf{A},\mathbf{C}} = AFM(\tilde{p}, \mathbf{A}, \mathbf{C})$), where we would like to avoid intersections at some parts of the paths.

Inspired by [96], we propose a cooperative extraction of the paths $\mathbf{A} \rightarrow \mathbf{B}$ and $\mathbf{A} \rightarrow \mathbf{C}$. The idea of this new method is to add to the cost $\tilde{p}$ a constraint around the neighbor centerline at the locations we do not want them to intersect, so the current path is influenced by the position of its neighbor. Ideally, we want to avoid overlap between the centerline and the neighbor artery; therefore the constraint region should cover this neighboring artery.

We start including the constraint region $\kappa \subseteq \mathbb{Z}^3$ around the best path $C^{Best} \in \{C_{\mathbf{A},\mathbf{B}}, C_{\mathbf{A},\mathbf{C}}\}$, as we assume this path is not going to change much its position during the cooperative correction process. We define the best path as the one with the lowest average cost, where the total cost is given by the minimal action map U at the end point, which is divided by the path length to get the average cost. To constrain the neighbor path C^N to be at least a distance ρ from C^{Best}, we include in $\tilde{p}$ a constraining region defined by a spherical dilation with radius ρ in all points of C^{Best} where we want to set the constraint. As we want to set the constraint after the artery bifurcation, the constraint region κ starts after this position where the artery starts

bifurcating. Then after defining the constrain region κ, the new cost p_N is given by:

$$p_N(\mathbf{x}) = \begin{cases} \tilde{p}(\mathbf{x}), & if \quad \mathbf{x} \notin \kappa \\ K, & if \quad \mathbf{x} \in \kappa \end{cases}, \tag{6.5}$$

where K is a high constant value. Therefore, the correction of path C^N is given by $\tilde{C}^N = AFM(p_N, \mathbf{A}, \{\mathbf{B}, \mathbf{C}\})$.
Subsequently, a new constraint region around the corrected path $\tilde{C}^N$ is included in $\tilde{p}$ to correct C^{Best}. This whole process is illustrated in Figure 6.2.

6.3 Experiments and Results

From three marked seed points at CCA, ICA, and ECA; we cooperatively extract two paths between CCA-ICA and CCA-ECA. Here κ starts at the closest points of the initially estimated centerlines to an extra marked point at the artery bifurcation where the two arteries ICA and ECA separate. We call this Cooperative method from the Common to Internal and External CCIE. We also evaluated another cooperative approach where a centerline bifurcation point (BIF) is used as a seed point. BIF is a shifting of the artery bifurcation point (see Section 6.3.2). Using BIF as a seed point, we force the centerlines to pass through this point. Therefore, in this approach we extract three paths: between CCA-BIF, and cooperatively we extract two paths between BIF-ICA and BIF-ECA. We call this Cooperative approach between Common to Bifurcation to Internal and External CCBIE.
We compare the cooperative centerline approaches to the traditional approach to extract the centerlines independently. In one approach, two Separated independent centerlines are extracted from the Common to Internal and External (SCIE). And in other approach we use BIF as a seed point where three separated independent centerlines are extracted (SCBIE).

6.3.1 Image Data

We used MRI of the carotid bifurcation from subjects with carotid artery plaque (at least one artery with a maximum wall thickness $\geq 2.5\,mm$ measured in ultrasound) from the Rotterdam study [105]. The method was initially evaluated in a data set with manually annotated centerlines composed of 161 carotid arteries from 83 subjects. Five arteries had to be discarded due to manual annotation errors. Further, the method was evaluated in a data set of 3,904 arteries from 2,018 subjects where seed points were available but no manually annotated centerlines. Several MRI sequences were acquired: Proton Density Weighted Black-Blood MRI (BB), Proton Density Echo Planar Imaging MRI, 3D T1-weighted gradient echo MRI, T2-weighted Echo Planar Imaging MRI, and Phase Contrast MRI (PC). As in [94], BB and PC were used together to get the cost image p as described in Section 6.2.2, which are the sequences that provide a better description of the artery lumen [105]. The image resolutions are (in-plane voxel size $\times$ Slice thickness): $0.507 \times 0.507 \times 0.9\,mm$ for BB, and $0.703 \times 0.703 \times 1\,mm$ for PC.

6.3.2 Manual annotations

Manually annotated centerlines were obtained by an expert on the BB images using a similar annotation framework as described in [46]. Per artery, several points are annotated between CCA-ICA and between CCA-ECA to obtain two centerlines. These are further up-sampled using a cubic spline interpolation of resolution equal to the step size δ to get two higher resolution centerlines between CCA-ICA (C^M_{ICA}) and CCA-ECA (C^M_{ECA}). The seed points located at CCA ($\mathbf{x}_C$), ECA ($\mathbf{x}_E$), and ICA ($\mathbf{x}_I$) were obtained from the starting and end points of the manual centerlines, where $\mathbf{x}_C$ is the mean point between the two centerline starting points. In the experiments where manual centerlines are not available, the three seed points were manually placed in the BB images by an expert.

Bifurcation point:

Another point located at the artery bifurcation ($\mathbf{x}_{BIF}$) is manually annotated. This point is located at the gap between the two artery branches at the first slice starting from CCA where these two are visible. As for SCBIE and CCBIE require the bifurcation seed point at the centerline bifurcation, we had to shift $\mathbf{x}_{BIF}$ to be inside the vessel at the centerline bifurcation. To shift $\mathbf{x}_{BIF}$, we move it a certain distance through the path between $\mathbf{x}_C$- $\mathbf{x}_{BIF}$ ($C_{\mathbf{x}_C,\mathbf{x}_{BIF}}$).
First, we define the estimated bifurcation $\mathbf{x}^e_{BIF}$, which serves as ground truth of the centerline bifurcation in the images with manually annotated centerlines. This is obtained as the mean point between the first positions in C^M_{ICA} and C^M_{ECA} starting from $\mathbf{x}_I$ and $\mathbf{x}_E$ where the distance from these point positions to the neighbor centerline is below $1\,mm$. We define the distance D from a point $\mathbf{x}$ to a path C by the L_2 norm between the point and the closest point in the path:

$$D\left(\mathbf{x}, C\right) = \min_{\mathbf{y}\in C} \|\mathbf{x} - \mathbf{y}\|. \tag{6.6}$$

We verified by visual inspection that the resulting $\mathbf{x}^e_{BIF}$ using this approach is close to the manual centerline bifurcation in most cases.
Subsequently, we define the path between the common point $\mathbf{x}_C$ and the annotated bifurcation $\mathbf{x}_{BIF}$ by $C_{\mathbf{x}_C,\mathbf{x}_{BIF}} = AFM\left(\tilde{p}, \mathbf{x}_C, \mathbf{x}_{BIF}\right)$. Then we find the closest point in the path to the estimated bifurcation $\mathbf{x}^e_{BIF}$. This point represents the shifted bifurcation $\mathbf{x}^s_{BIF} \in C_{\mathbf{x}_C,\mathbf{x}_{BIF}}$. The distance between $\mathbf{x}_{BIF}$ and $\mathbf{x}^s_{BIF}$ is the optimal shifting using this approach. The found optimal shifting for all 161 arteries was $5.1\,mm \pm 1.6\,mm$; therefore, we used $t = 5.1\,mm$ to obtain $\mathbf{x}^s_{BIF}$ in all cases.

6.3.3 Preprocessing

The BB images suffer from intensity inhomogeneity [45]. This was corrected using N4 bias field correction [100], which is one of the most popular methods to correct intensity non-uniformity in MRI data. We used the default parameters of the method on the complete image as described in [100]. Further as in [94], PC images are registered to the BB images. However, by only using an affine registration as in [94], we observed several registrations errors that resulted in erroneous cost images p.

We could obtain p using only one sequence, however as in [94] we also observed that it is useful to include both BB and PC to obtain p. Therefore, instead we used a different approach to perform the registration and include both sequences to get p. Similar to [111], we apply a rigid then a non-rigid registration using a registration mask. For the rigid registration, we use Euler transform, and for non-rigid a 3D B-spline transformation with 15 mm grid spacing, using in both mutual information as similarity metric. The registration mask must cover the artery in BB. For this a 10 mm diameter circular mask obtained by dilating the centerlines with a spherical structuring element with a radius of 5 mm is used. As this mask must roughly cover the artery, an accurate centerline is not needed. Therefore, to compute these centerlines we get two minimum cost paths between CCA($\mathbf{x}_C$)-ICA($\mathbf{x}_I$) and between CCA($\mathbf{x}_C$)-ECA($\mathbf{x}_E$) on a cost obtained from BB only (p_{BB}). Then after registering PC to BB, we obtain the combined cost p. In Figure 6.3, the registered PC look well aligned, and the cost is low at the artery locations.

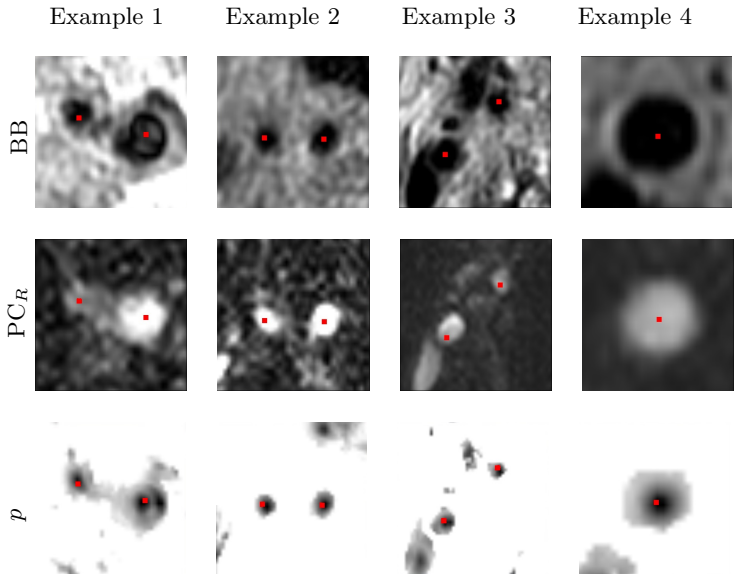

Figure 6.3. Examples of the registration and cost extraction results. BB images, registered PC to BB using the presented approach (PC$_R$), and cost images (p) from three different arteries are shown. Manual centerlines overlaying the images are depicted in red.

6.3.4 Parameter selection and Configuration

As in [94], we choose the contribution of the medialness filter and lumen intensity similarity equal in Eq. 6.1 ($\alpha = \beta$). We evaluated several smoothing values $\omega \in \{0, 1, 2, ... 10\}$ to get $\tilde{p}$, where the selected value for each artery was obtained by leave-one-artery-out cross-validation. To make a faster computation of U and ΔU, the cost image $\tilde{p}$ is cropped in a minimum bounding box ± 20 voxels in the x-y plane

and ± 3 voxels in the axial direction around the seed points. This bounding box size was enough to cover the artery in all cases. The step size δ is set to $0.1\,mm$, which is significantly smaller than the voxel size.
The diameter $2 \times \rho$ of the constraint region κ is set to $3.5mm$. We observed this value was enough to cover the ICA and ECA artery lumen [56]. In CCIE and CCBIE, κ starts at the closest point of the initially estimated centerline to the artery bifurcation point.

6.3.5 Evaluation Metric

To compare the automatically extracted centerlines to the manually annotated centerlines we compute the Hausdorff distance between centerlines. The H distance between two centerlines C^A and C^B is defined as:

$$H(C^A, C^B) = \max \left\{ \max_{\mathbf{x} \in C^A} D(\mathbf{x}, C^B),\ \max_{\mathbf{y} \in C^B} D(\mathbf{y}, C^A) \right\}. \tag{6.7}$$

For each carotid artery two centerlines are defined. Thus the Centerline Artery Distance (CAD) between automatic (C^A_{ICA}, C^A_{ECA}) and manual artery centerlines (C^M_{ICA}, C^M_{ECA}) is given by the maximum distance between centerlines by:

$$\max \left\{ H(C^M_{ICA}, C^A_{ICA}),\ H(C^M_{ECA}, C^A_{ECA}) \right\}. \tag{6.8}$$

We consider a centerline detection failed if the CAD between automatic and manual centerlines is above $3.5\,mm$, as the mean artery radius is about this value [56].

6.3.6 Comparison with manual annotations

Initially, we observed the effect of the smoothing parameter ω in the different approaches. For each value of ω, we obtained CAD for all 161 vessels for each approach. Median values and number of failures for each ω are shown in Figure 6.4. Better results were observed by enforcing some amount of smoothness in the centerlines. In all ω values, the cooperative centerline extraction methods (CCBIE and CCIE) showed better results than obtaining the centerlines independently (SCBIE and SCIE) in number of failures. A reduction in failures was obtained by including the bifurcation as an extra seed point (CCBIE Vs. CCIE and SCBIE Vs. SCIE), however this increases the median CAD slightly.
The optimal smoothing value ω per artery and for each method was selected by leave-one-artery-out cross-validation. From the training set of 160 arteries, we aimed to select the value for ω that resulted in least failures; in case several ω resulted in the same number of failures, the value resulting in the lowest mean CAD is selected. The number of failures per method are: SCIE: 10 failures, SCBIE: 8, CCIE: 5, and CCBIE: 3. A box plot describing the CAD results is shown in Figure 6.5. Significant results (McNemar test) for differences in the number of failures between methods is shown in Table 6.1. CCBIE is significantly better ($p < 0.05$) than SCIE. Other differences are not significant. Several centerlines examples using all methods are shown in Figure 6.6.

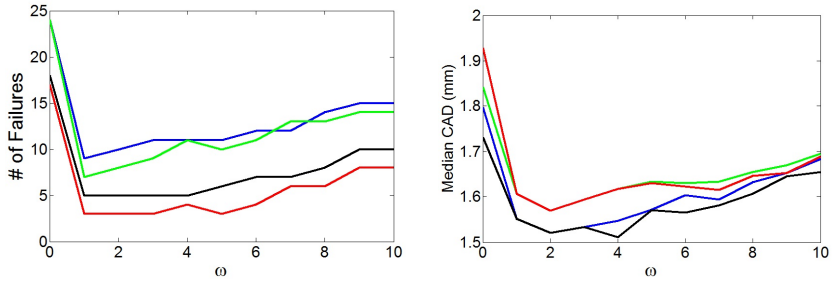

Figure 6.4. Number of failures and median CAD depending on the smoothing parameter ω for each method. SCIE is represented in blue, SCBIE green, CCIE black, and CCBIE red.

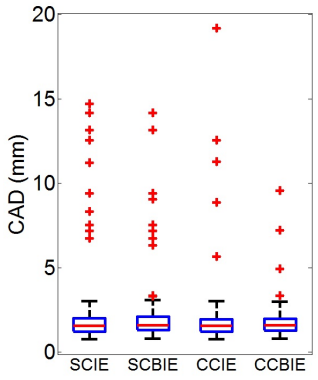

Figure 6.5. Box plot showing the CAD errors per method.

6.3.7 Results in a large population data set

We also obtained the centerlines in a large data set from a population study composed of 3,904 arteries from 2,018 patients. We compare the best method to extract the centerlines independently (SCBIE) to the best method to extract them cooperatively (CCBIE). However, for this data set we do not have manually annotated centerlines, but only the seed points at CCA, ICA, ECA, and the bifurcation. Therefore, to compare the two methods, we first compute CAD between the two centerlines. Then, arteries with CAD above 3.5 mm are the cases of interest. From the 3,904 arteries, we found 42 to have CAD between SCBIE and CCBIE above 3.5 mm. A visual inspection of these 42 cases revealed that in 28 cases CCBIE is correct while SCBIE fail, 4 SCBIE are correct while CCBIE fail, in 7 cases both fail, and in no case both are correct. One case was discarded due to wrong seed point locations, and due to occlusion of arteries, the centerline could not be reliably assessed in two arteries. Applying McNemar test, we obtain that CCBIE is significantly better than SCBIE ($p < 0.0001$) resulting in fewer centerline failures.

Table 6.1. Statistical significance of differences in number of failures between methods according to McNemar's test. p-values are shown for each method comparison for the 161 arteries experiments described in Section 6.3.6 and for the 3,904 arteries experiment described in Section 6.3.7 (in parenthesis).

	SCIE	SCBIE	CCIE	CCBIE
SCIE	–	0.5	0.06	0.02
SCBIE	–	–	0.45	0.06 (0.0001)
CCIE	–	–	–	0.5

6.4 Discussion

In this work we presented a method to better extract the carotid artery centerlines which results in fewer failures. In this method both artery centerlines from CCA to ICA and ECA are extracted cooperatively by integrating geometrical information of the artery bifurcation in the cost. Inspired by [96], geometrical information is integrated as constraint sections around the paths to prevent path intersections. We demonstrated the presented method to be better than the traditional approach to extract the centerlines independently.

Commonly the centerlines in the carotid artery bifurcation are extracted as two minimum cost paths [27, 28, 42, 94, 116], however if the cost image is not well defined everywhere failures may arise. In this work, we showed that these inaccuracies in the cost which may lead to centerline errors could be overcome using the presented cooperative centerline extraction approach. Another possible solution to get better centerlines would be to improve the cost image. In [47, 94], a refined cost is generated using the extracted centerline, where the medialness is calculated at planes sampled perpendicular to the centerline, which may result in a better cost image. However, this approach is likely to fail if the centerline used to reformat the image is outside the vessel lumen. Therefore, failure cases would not be prevented using this approach.

There are other methods to jointly or cooperatively extract the centerlines based on evolution approaches [122], skeletonization of the segmentation [112], and matching appearance models [121]. Evolution approaches require an initialization, where if this is outside the artery an incorrect centerline would be likely obtained, as these methods may get stuck in a local minimum. Skeletonization of the segmentation may work well in cases of relatively correct segmentations, however segmentation of the carotid artery from MRI is not an easy task and most methods require a centerline as initialization. Skeletonization of segmentations using the method presented in [103] may be a good option, as it does not require the centerline as initialization and presents good results. The matching appearance model based on fitting cylindrical patterns presented in [121] is an interesting method as it is fully automatic, however they reported failures for what they call complex cases which may be the case for some carotid arteries. In any of these methods it is not guaranteed that the vessels

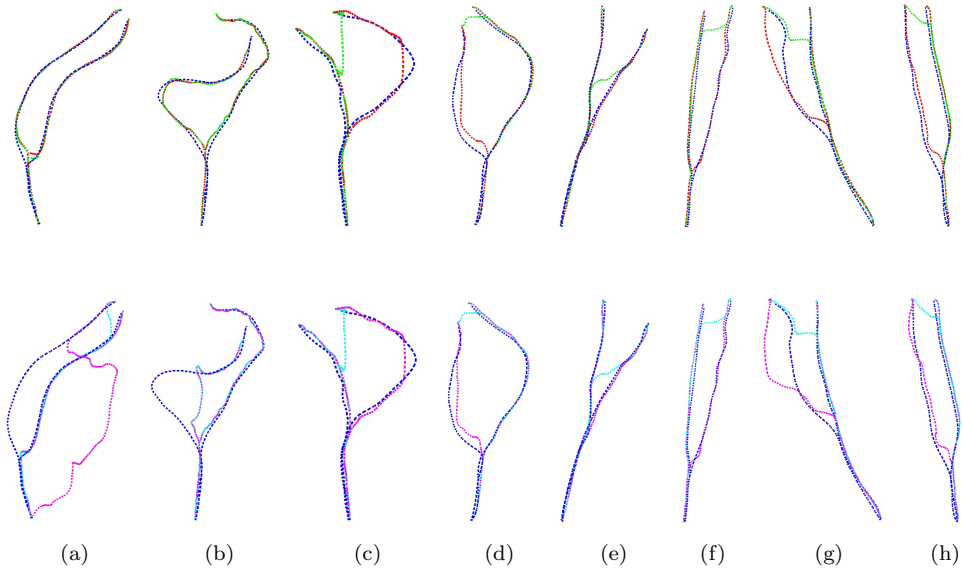

Figure 6.6. Examples of centerline results where failures are present. Manual centerlines are represented in blue, SCIE in cyan, SCBIE in green, CCIE in purple, and CCBIE red. Methods that use the bifurcation as a seed point are shown at the top row. SCIE fails in all cases (CAD error $\geq 3.5\,mm$); SCBIE fails in cases c-h; CCIE fails in a, b, g; and CCBIE fails in g.

do not intersect after the bifurcation which is a common source of centerline failures, while in the presented method we guarantee both centerlines will not follow the same path after the bifurcation.

Another possible solution to get more accurate centerlines is applying smoothing to the path, as the path intersection errors are often accompanied by high curvature paths. We explored this solution in Section 6.3.6 by adding a constant ω to the cost image similar to [25], which penalizes long paths, and therefore reduce curvature. We proved the smoothing to be useful as fewer failures and more accurate centerlines were obtained when applying certain level of smoothing. We also observed that high smoothing values affected the results negatively. Even though overall the smoothing improves the centerlines, still several failures were obtained in SCIE. Therefore, smoothing only is not enough to significantly reduce centerline failures.

Using the cooperative approaches (CCIE and CCBIE) we showed better results in terms of number of failures than using the approaches without interaction between paths (SCIE and SCBIE). Additionally, we observed that only including the bifurcation point as an extra seed point in SCBIE seemed to have already a small positive effect in terms of number of failures compared to SCIE, this effect was not significant in the 161 arteries set. Therefore, we think that adding the bifurcation point without using interaction between centerlines is not sufficient to get significant improvements. Using the cooperative centerline extraction methods, we also showed a slight reduction of number of failures by using the bifurcation as an extra seed point in CCBIE

instead of a reference point to build the constraint regions as in CCIE. Figure 6.6 showed that the centerlines in CCIE may fail before the artery bifurcation, so adding the extra seed point helps to prevents these failures.
However, Figure 6.4 seems to indicate that adding the bifurcation as extra seed point also reduces the accuracy of the centerlines in non-failure cases. This can be explained partly by the fact that the centerline bifurcation in a bifurcating structure is poorly defined and difficult to assess manually. In addition, the annotated bifurcation point is located at the artery bifurcation which is easy to visualize, this point had to be shifted to be used as a seed point, which may introduce small inaccuracies in the centerlines. Although the accuracy reduction in non-failure cases, we believe CCBIE to be the preferred method because it results in the least number of failures.
Even though, the cooperative approach leads to fewer failures, a disadvantage is that it requires one additional annotated point. However, we think one point is not too much work to annotate. Additionally, there are methods to automatically extract bifurcation points which could potentially be used in the carotid artery [80]. Therefore, we think using an extra annotated point at the bifurcation results in a positive trade-off.
Another disadvantage of the proposed cooperative method compared to the approach to extract the centerlines independently is the need to perform two extra minimum cost path computations. However, algorithms with logarithmic complexity for fast AFM computation are available [88], so the computations of extra paths should not represent a big issue in most current processing machines.
The best method CCBIE, still resulted in three failures out of 161 arteries and 11 of 42 difficult cases in the larger study. We observed the cost images to be poorly defined in some cases due to registration errors, and in other cases neighbor structures close to the artery had a low cost. We think adding more constraints in the cooperative extraction will not fix such cases. An improved registration, and cost extraction which discriminate neighbor structures could be investigated.
The main reason to extract the carotid artery centerline is to define a ROI for further processing such as registration [111], or to initialize a segmentation method [6,45,94], where reducing the centerline failures is very important. If the centerlines follow a wrong path outside the vessel, a registration or segmentation will likely fail [6, 21]. Therefore, we think the presented method to extract the centerlines is highly suitable for further processing, as it considerably reduces the number of failures. Additionally, this method might be applicable in other applications as neuron tracking, pulmonary tree extraction, coronary centerlines; as this method could be easily extended to extract more than two centerlines.

6.5 Conclusion

In conclusion, we present a simple, yet effective approach to improve centerline extraction in the carotid artery bifurcation. This method significantly reduced the number of centerline tracking failures.

Chapter Seven

Comparison of CT and MRI for detection and quantification of carotid artery calcification: The Rotterdam Study

Abstract — Carotid artery atherosclerosis is an important risk factor for stroke. As such, quantitative imaging of carotid artery calcification, as a proxy of atherosclerosis, has become a cornerstone of current stroke research. Yet, population-based data comparing the main imaging modalities (computed tomography and magnetic resonance imaging) for the detection and quantification of calcification remain scarce. A total of 684 participants from the population-based Rotterdam Study underwent both a CT-examination and an MRI-examination of the carotid artery bifurcation to quantify the amount of carotid artery calcification (mean interscan interval: 4.9 ± 1.2 years). We investigated the correlation between the amount of calcification measured on CT and an MRI using Spearmans correlation coefficient, Bland-Altman plots, and linear regression. In addition, using logistic regression modeling, we assessed the association of CT- and MRI-based calcification volumes with a history of stroke. We found a strong correlation between CT- and MRI-based calcification volumes (Spearmans correlation coefficient: 0.86, p-value ≤ 0.01). Bland-Altman analyses showed a good agreement, though CT-based calcification volumes were systematically larger. Finally, calcification volume assessed with either imaging modality was associated with a history of stroke with similar effect estimates (odds ratio (OR) per 1-SD increase in calcification volume: 1.52 ($95\%CI : 1.00; 2.30$) for CT, and 1.47 ($95\%CI : 1.01; 2.14$) for MRI. CT-based and MRI-based volumes of carotid artery calcification are highly correlated, but MRI-based calcification is systematically smaller than those obtained with CT. Despite this difference, both provide comparable information with regard to a history of stroke.

Based upon: Blerim Mujaj, Andres M. Arias Lorza, Arna van Engelen, Marleen de Bruijne, Oscar H. Franco, Aad van der Lugt, Meike W. Vernooij, Daniel Bos, "Comparison of CT and MRI for detection and quantification of carotid artery calcification: The Rotterdam Study", *published* in Journal of Cardiovascular Magnetic Resonance, 2017.

7.1 Background

Atherosclerosis located at the bifurcation of the carotid artery is an important risk factor for stroke [33, 57, 62, 68, 70]. As such, quantification of the severity of carotid atherosclerosis has become an increasingly important topic in stroke research. Multiple non-invasive imaging techniques, including ultrasound, Computed Tomography (CT), and Magnetic Resonance Imaging (MRI), are currently available to obtain measures of the extent of atherosclerosis [75]. An important advantage of CT and MRI is that both modalities offer possibilities for detailed characterization and quantification of the atherosclerotic plaque [39]. The mostly studied characteristic of the atherosclerotic plaque is calcification, given that it is one of the most prominent plaque characteristics and represents a reliable marker of the underlying plaque burden [73]. For the visualization of calcification, non-contrast CT is acknowledged to be superior to any other imaging modality [22]. Yet, thanks to rapid technological advances, non-contrast MRI now also allows for the detection and quantification of calcification in the atherosclerotic plaque [97] and has the major advantage over CT that it does not involve radiation exposure. Moreover, with MRI it is possible to visualize additional plaque characteristics such as intraplaque hemorrhage or lipid-rich necrotic core which provide unique additional information on the disease. Despite these potential advantages of MRI, it remains unclear whether calcification volumes obtained with MRI are comparable to those measured with CT. Against this background, we set out to quantify and compare CT-based and MRI-based carotid artery calcification in terms of absolute volumes and with respect to the history of stroke as a relevant clinical outcome, in participants from the population-based Rotterdam Study.

7.2 Material And Methods

7.2.1 Setting

This study was carried out within the framework of the Rotterdam Study, a prospective population-based study among middle-aged and elderly persons [48]. Between 2003 and 2006, all participants that visited the research center were invited to undergo Multi-Detector Computed Tomography (MDCT) to quantify vascular calcification in multiple vessels, including the carotid artery bifurcation [74]. In total 2,524 participants were scanned.

From October 2007 onwards, carotid MRI was incorporated in the Rotterdam Study. Between 2007 and 2012, we invited 2,666 participants to undergo an MRI examination of the carotid arteries to study atherosclerotic disease. These participants were selected on the basis of the presence of atherosclerosis in at least one carotid artery on ultrasound examination (defined as intima-media thickness $> 2.0\,mm$ in one or both carotid arteries), which is regularly performed in all Rotterdam Study participants. In total 1,982 participants underwent carotid MRI. From these 1,982, 808 participants had also undergone a CT-examination. Due to image artifacts or low image quality (n=31), or errors in the MRI registration process needed for analysis

(n=93) 124 participants were excluded, leaving 684 participants with usable CT and MRI data for the current study. The mean time interval between CT scan and MRI scan was 4.9 years (standard deviation 1.2 years).

7.2.2 Assessment of CT-based calcification

We performed a non-enhanced CT-examination (16-or 64-slice MDCT Somatom Sensation, Siemens, Forchheim, Germany) that reached from the aortic arch to the intracranial vasculature, to visualize calcification in the extracranial carotid arteries. The detailed information regarding the scan protocol is described elsewhere [74]. In short, the following scan parameters were used: 16 x 0.75 mm collimation, 120 kVp, 100 effective mAs, and 0.5s rotation time, with a normalized pitch of 1. Images were reconstructed with an effective slice width of 1 mm, a reconstruction interval of 0.5 mm, and a medium sharp convolution kernel [74]. Calcification in the extra-cranial carotid artery was measured bilaterally within three centimeters proximal and distal of the bifurcation and was automatically quantified with dedicated commercially available software (syngo calcium scoring, Siemens, Germany) [74]. Calcification volumes in both carotid arteries were expressed in cubic millimeters (mm^3) [104] (Figure 7.1).

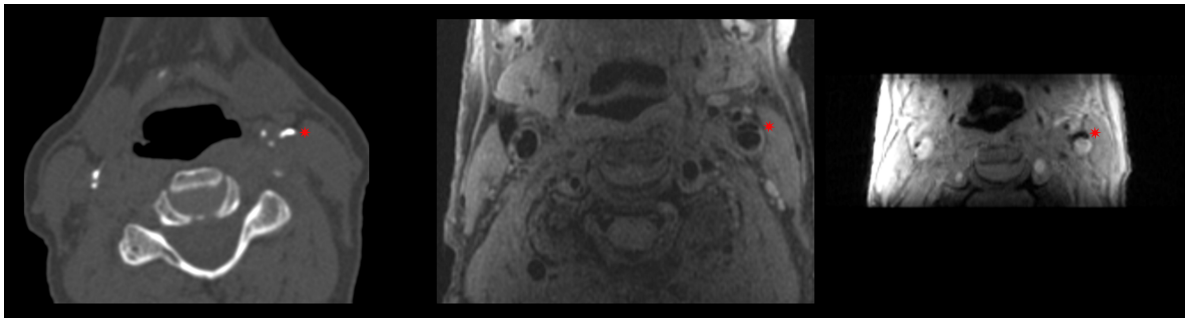

Figure 7.1. Example of calcification in the left carotid artery bifurcation (indicated by the red star) on CT (left image) and on MRI (middle image; PDw-FSE-BB sequence, and right image; magnitude image of the 3D-phase contrast sequence).

7.2.3 Assessment of MRI-based calcification

MRI imaging of the carotid arteries was performed on a single 1.5-T scanner (GE Healthcare, Milwaukee, WI, USA) with a dedicated bilateral phased-array surface coil (Machnet, Eelde, The Netherlands). The high-resolution images were obtained using a standardized protocol [105]. First, both carotids were identified by means of two-dimensional (2D) time-of-flight MR angiography. Second, high-resolution MRI sequences were planned to image the carotid bifurcations on both sides. These sequences consisted of four 2D sequences in the axial plane, namely a Proton Density weighted (PDw)-Fast Spin Echo (FSE)-Black Blood (BB) sequence (in-plane resolution 130/160 x 130/128 = 0.8 x 1 cm); a PDw-FSE-BB with an increased in-plane

resolution (in-plane resolution 130/224 x 130/160 = 0.5 x 0.8 cm); a PDw-Echo Planar Image (EPI) sequence (in-plane resolution 130/160 x 70/160 = 0.8 x 0.4 cm); and a T2w-EPI sequence (in-plane resolution 130/160 x 70/160 = 0.8 x 0.4 cm). Additionally, we performed two 3D sequences, namely a 3D-T1w-Gradient Echo (GRE) sequence (in-plane resolution 180/192 x 180/180 = 0.9 x 1 cm), and a 3D phased-contrast MR angiography (in-plane resolution 180/256 x 180/128 = 0.7 x 1.4 cm). The total scanning time was approximately 30 min [105]. Calcification was evaluated bilaterally within three centimeters proximal and distal of the bifurcation [74]. All calcification measurements on MRI were performed by one trained physician under the supervision of an experienced neuroradiologist. We performed an intra- and inter-observer reproducibility analysis on a random set of 30 MRI examinations. The intra- and inter-agreement was very good [Cohens Kappa : 0.91 ($95\%CI 0.82 - 0.99$) and 0.94 ($95\%CI 0.86 - 0.99$)], respectively. We defined calcification as a hypointense region in the plaque on all sequences. We manually annotated and segmented calcification in all plaques using a standardized approach. First, we pre-processed all images using a method that has been described extensively before [15]. This starts with a bias correction to reduce the intensity inhomogeneity characteristic in MRI [6]. Subsequently, the carotid artery in all images was rigidly registered to the black-blood image space using the Elastix tool [6]. For the registration of the sequences, a Region Of Interest (ROI) around the artery in black-blood was used. This ROI was obtained semi-automatically by uniformly growing an extracted carotid artery centerline, which requires three marked seed points at the common, internal and external parts of the artery [6]. Then calcification was manually delineated in every consecutive slice using an annotation tool developed in Mevislab (MeVisLab, MeVis Medical Solutions AG). Fourth, the total volume of calcification was calculated by counting the number of voxels within the annotated areas and multiplying this by the voxel volume (Figure 7.1). This provided volumes of calcification in cubic millimeters.

7.2.4 Assessment of history of stroke

At study entry, all participants were interviewed and a history of stroke was assessed. Moreover, after enrollment, all participants are continuously followed for the occurrence of stroke [16]. All potential stroke events were reviewed by research physicians and verified by an experienced stroke neurologist [114]. At the time of CT scan, 38 participants had suffered a prior stroke [16].

7.2.5 Statistical analysis

Due to skewed distributions of the calcification data, we used natural log (Ln) transformed values after we added 1.0 mm^3 to the non-transformed data in order to deal with calcification scores of zero (Ln (calcification volume +1.0 mm^3)) [16]. Our analysis strategy consisted of four steps. First, we investigated the correlation of CT-based calcification volumes with MRI-based calcification volumes using Spearmans correlation coefficient. Second, we used linear regression to assess the relation between CT-based and MRI-based calcification volumes while adjusting for the time interval between the scans. Given the substantial time interval between the CT and MRI

examinations, we furthermore performed a sensitivity analysis in which we analyzed the correlation between CT-based and MRI-based calcification volumes only for those persons with an interval equal or less than 3 years (n = 128). We performed post-hoc sensitivity analysis while adjusting for CT-scanner type also.

Third, we assessed the agreement between CT-based and MRI-based calcification volumes using a Bland-Altman analysis. Fourth, as a proof-of-principle, we investigated the association of CT-based and MRI-based calcification volumes (per 1-SD increase) related with a history of stroke using logistic regression while adjusting for age, sex and the time interval between CT and MRI, and studied whether the results were comparable for both modalities All analyses were carried out using IBM SPSS Statistics version 21 (International Business Machines Corporation, Armonk, New York).

7.3 Results

Table 7.1 shows the baseline characteristics of the study population. The mean age of participants at the time of CT examination was 68.1 years (SD: 6.1 years). There were 41.5% female participants. We found no calcification in 60 participants (8.8%). There were no instances in which calcification was found on either CT or MRI and not on the other modality. The mean Ln-transformed calcification volume for CT was 3.98 mm^3 (SD: 1.86 mm^3), and 2.70 mm^3 (SD: 1.36 mm^3) for MRI.

We found a strong correlation between CT and MRI calcification volumes (Spearmans correlation coefficient:0.86) (Figure 7.2, supplementary table 7.1, and supplementary table 7.2). This correlation was similar when we investigated the left and right side separately (supplementary table 7.1). After performing linear regression with adjustment for the time interval between the CT and MRI scan, the prominent relation between CT-based and MRI-based calcification volumes remained present [beta per 1-SD increase in CT-based calcification volume: 0.65 (95% confidence interval (CI): 0.63;0.68)]. After performing the analyses in those persons with a time interval between the scans of less or equal to 3 years, the association between CT-based and MRI-based calcification volumes was similar [beta per 1-SD increase in CT-based calcification volume: 0.65 ($95\%CI : 0.58; 0.72$)]. Adjustment for CT-scanner type did not influence the results (data not shown).

Figure 7.3 shows the Bland-Altman plot for the relation between the absolute differences in Ln-transformed calcification volumes and the mean of the two measurements of 1.27 mm^3 (standard deviation: 0.92). We found that the CT-based calcification volumes were consistently larger than those obtained from MRI.

When investigating the relationship between calcification and a history of stroke, we found that both CT-based and MRI-based calcification volumes were associated with a history of stroke [CT - odds ratio per 1-SD increase: 1.52 ($95\%CI : 1.00; 2.30$), MRI odds ratio per 1-SD increase: 1.47 ($95\%CI : 1.01; 2.14$)] (Table 7.2).

Table 7.1. Baseline characteristics of study participants. Values are means with standard deviations for continuous variables and percentages for dichotomous or categorical variables. * Ln-transformed volumes (Ln(calcification volume+1mm^3)). Abbreviation: CT = computed tomography, HDL = high-density lipoprotein, MRI = magnetic resonance imaging.

Sample size	684
Woman	41.5%
Age, years at CT scan	68.8 ± 6.1
Age, years at MRI scan	74.2 ± 6.1
CT calcification volumes, mm^3*	3.98 ± 1.87*
MRI calcification volumes, mm^3*	2.70 ± 1.37*
Smoking (current)	40.2%
Systolic blood pressure (mm/Hg)	146.81 ± 19.46
Diastolic blood pressure (mm/Hg)	79.84 ± 10.85
Diabetes Mellitus	13.3%
Serum total cholesterol (mmol/L)	5.6 ± 0.9
HDL cholesterol (mmol/L)	1.4 ± 0.3
Antihypertensive medication use	37.7%
Statin medication use	31.1%
Stroke events	5.6%

7.4 Discussion

In this large population-based sample of persons with subclinical atherosclerosis, we found that CT-based and MRI-based volumes of carotid artery calcification are highly correlated, but MRI-based calcification is systematically smaller than those obtained with CT. Despite this difference, both provide comparable information with regard to a history of stroke.

We found that CT-based and MRI-based calcification volumes were highly correlated. Yet, we also found that the volumes measured with MRI were systematically

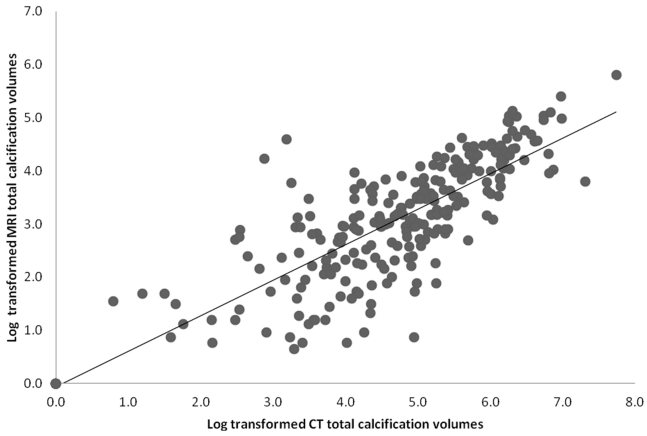

Figure 7.2. Scatter plot of Ln-transformed CT-based and MRI-based calcification volumes, indicating a positive correlation between both detected and quantified calcification volumes.

Table 7.2. Association of calcification volumes with stroke. Model 1 - scan time difference. Model 2 adjusted for age, sex and scan time difference. Values represent odd ratios with 95% CI per 1 standard deviation increase in calcification volumes. Abbreviation: CT = computed tomography, MRI = magnetic resonance imaging.

	Odds ratio (95%CI)	p-value
Model 1		
CT calcification volumes	1.63 (1.09-2.46)	0.01
MRI calcification volumes	1.55 (1.07-2.24)	0.01
Model 2		
CT calcification volumes	1.52 (1.00-2.30)	0.04
MRI calcification volumes	1.47 (1.01-2.14)	0.04

smaller than those measured on CT. This was especially interesting in light of the fact that the MRI was performed on average 4 years later than the CT. Given that our scanning protocol on CT was specifically designed for the visualization of vascular calcification combined with that CT is currently the gold standard for the assessment

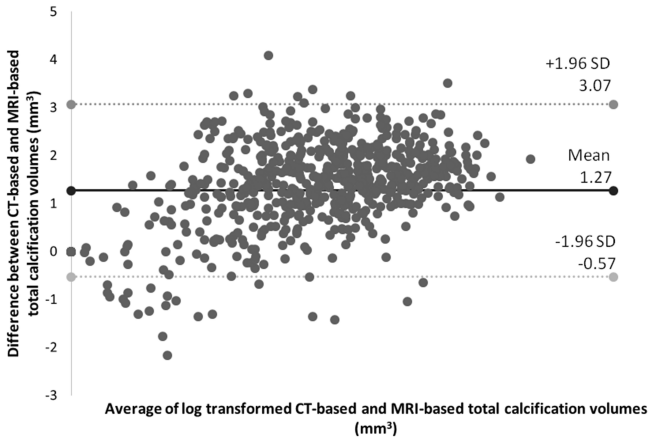

Figure 7.3. Bland-Altman plot of the difference of CT-based and MRI-based Ln-transformed total calcification volumes, with a mean absolute difference (bold continues line) and 95% confidence interval of mean differences (dashed lines).

calcification, it is likely that with MRI the amount of calcification is systematically underestimated [75]. The reason for this could the differences between CT-based and MRI-based calcification volume may be explained by differences in image analysis to a certain extent. Additionally, differences in spatial resolution between CT and MRI might be a potential explanation for this difference. In this light, it is important to note that CT images were analyzed automatically using dedicated commercially available software, while MRI images were analyzed manually for the presence and amount of calcification. To our knowledge, there are no studies that have compared CT and MRI on the detection and quantification of carotid artery using a non-invasive population-based approach. Previous research performed on the comparison between CT and MRI in 50 patients with recent TIA or minor stroke, demonstrated a correlation between CT-based and MRI-based calcification volumes of the only p: 0.55 [58]. We demonstrate that with the use of dedicated MRI-multi-sequences for the detection of calcification the correlation between CT-based and MRI-based calcification volume is substantially improved. Finally, another important topic to consider with regard to the difference between CT and MRI is the blooming effect of calcifications which is known to occur on CT [29]. Especially for calcifications with very high Hounsfield units, a gradient over multiple adjacent pixels is necessary to reach a low Hounsfield unit. This effect may lead to slight overestimation of the calcification area. On the other hand, MRI is known to underestimate the amount of calcification, because a certain amount of calcification is required before the MR-signal disappears. In this context, it is important to acknowledge that possible micro-calcifications in the atherosclerotic plaque may be missed [8].
As a proof of principle, we investigated the association of CT-based and MRI-based calcification with a history of stroke and found that both related to this outcome with comparable effect estimates. We chose history of stroke because the relationship

between carotid artery calcification and stroke has been well-established [15, 16, 81]. Importantly, despite the fact that MRI systematically underestimates the amount of calcification compared to CT, we found comparable risk estimates for CT-based and MRI-based calcification volumes with respect to a history of stroke. This suggests that when assessing clinical outcomes, the value of MRI-based calcification is similar to that of CT.

Our findings have implications that should be considered in the choice for MRI or CT for the assessment of vascular calcification. First, while assessing atherosclerosis with MRI it is directly possible to visualize other plaque characteristics in addition to calcification, including intra-plaque hemorrhage and lipid-rich necrotic core which provide unique additional information on the disease. Second, MRI has the major advantage over CT that it does not involve harmful radiation exposure. Third, the systematic underestimation of calcification on MRI may pose a problem, specifically in situations where one is particularly interested in the exact amount of calcification. Fourth, drawbacks of MRI, in general, are its absolute contraindications (i.e. metal objects in the body), and the fact that MRI is more time-consuming, more expensive and less widely available than CT. Taken together, the pros and cons of both imaging modalities should be carefully considered for all research and clinical applications involving the assessment of vascular calcification.

The strengths of our study include the relatively large sample size of community-dwelling individuals, all with varying degrees of carotid atherosclerosis, and the standardized assessment of calcification volumes on both modalities. Yet, some limitations should also be taken into account of which the first is the time interval between the CT scan and the MRI scan, with a mean interval of 4.9 years. We acknowledge that the interscan interval represents a potential limitation of the current study and that during this interval there may have been slight changes in plaque composition. Yet, we would like to emphasize that in all instances the CT-scan was made before the MRI-scan and that calcification is a plaque component that generally remains present and shows only very slow progression over time [108, 109]. Therefore, it seems unlikely that the amount of calcification at the time of MRI would differ substantially from that at the time of the CT. This is further supported by the fact that adjustment for the time interval did not change the results; and secondly by our finding that MRI volumes were consistently estimated somewhat smaller than CT volumes, whereas a large influence of the time interval would induce an opposite difference. Another potential limitation is that we used two types of MDCT scanners (16-slice and 64-slice) to assess calcification. Yet, adjustment for scanner-type did not change the association.

7.5 Conclusion

In summary, CT-based and MRI-based volumes of carotid artery calcification are highly correlated, but MRI-based calcification is systematically smaller than those obtained with CT. Despite this difference, both provide comparable information with regard to a history of stroke.

Chapter Eight

Summary and Discussion

In this thesis we presented several (semi-)automatic image processing techniques for analyzing the carotid artery wall and carotid artery plaque in MRI and US. The presented methods include image segmentation, registration, centerline extraction, and quantification. First we present a summary of the contribution of this thesis, and then we further discuss them.

8.1 Summary

8.1.1 Segmentation

In Chapter 2 we presented a new method to segment the carotid artery wall in MRI. Segmentation of the artery wall is an important step towards the detection and analysis of the composition of atherosclerotic plaques. The segmentation method simultaneously finds both the inner and outer wall borders based on a graph-cut approach which guarantees an optimal solution. Local image information is used in the form of directional derivatives as edge descriptors. The method also allows the integration of multiple MRI sequences, which enables using complementary information from the different images. We observed good inner border segmentations with 0.89 dice overlap, and differences between automatic results and manual annotations were comparable to the inter-observer variability. Also the inner border volumes were highly reproducible for scanning-re-scanning in a short time interval. For the outer border, the segmentation results were moderate (0.86 dice), showing a lower agreement than between observers, and lower reproducibility than for the inner border. Performance of both inner and outer border segmentation was comparable to other recently published carotid artery wall segmentation methods [45, 103, 110]. The advantage of the presented method is that it requires little user interaction, three marked points in the artery, and it segments the complete bifurcation.

In Chapter 3 we presented an extension of the method described in Chapter 2, aiming to get more accurate segmentations. As the method presented in Chapter 2 only used directional derivatives as local image information, this is relatively sensitive to noise and lack of contrast in the image. Therefore some errors were obtained specially at the outer border of the artery wall, which generally has worse contrast than the inner border. Therefore, we extended the method presented in Chapter 2 by including more features next to edge information. Here several descriptive features are represented

as probability maps using a classifier, and the graph cut maximizes the probabilities per region for segmentation. We demonstrated that this method is better than the one presented in Chapter 2, resulting in good segmentations of both inner (0.88 dice) and outer border (0.92 dice) which were comparable to inter-observer agreement. Additionally, the wall volumes could be determined with high reproducibility in a scan-re-scan study.

In Chapter 4, we presented a method to segment the carotid artery lumen in 3D US. Carotid arteries are frequently imaged with US. Lumen segmentation of US data would enable the investigation of carotid artery geometry and the narrowing of the vessel caused by the presence of plaque [2]. To segment the artery lumen in US, we used a similar graph approach as described in Chapter 2 to only segment the inner border of the wall. However, in US the borders of the arteries look more irregular compared to MRI. Therefore, the graph segmentation approach was applied iteratively to compensate for cases where the graph initialization is very far from the artery border. Applying this segmentation method good results were obtained in healthy volunteers (0.84 dice), and fair results in patients (0.67 dice).

8.1.2 MRI-US Registration

In Chapter 5, we presented a method to register arteries in MRI and US using geometrical features. Centerlines and lumen segmentations were used as features. Registration was necessary to facilitate a comprehensive analysis and visualization of the complementary information of both imaging modalities. However, current methods to register MRI and US yield high errors when correlating intensity information or require high amount of user interaction. We used the methods described and presented in Chapters 2 and 4 to extract the centerlines and obtain the lumen segmentations in MRI and US respectively. The registration procedure finds a transformation that minimizes a dissimilarity metric using these geometrical features. Good registrations were obtained with errors in the order of the MRI and US voxel sizes ($\sim 0.8\,mm$). Additionally, the presented method outperformed an image intensity and point based registration approach, and registration when using only the centerlines.

8.1.3 Vessel Centerline Extraction

In Chapter 6 we presented a new method to extract the carotid artery centerlines cooperatively. The artery centerline is important to analyze its geometry, and as an input for segmentation and registration methods. Generally, both centerlines from CCA to ICA and from CCA to ECA are detected separately without considering any interaction. Applying this approach using minimum cost paths may result in errors in cases where the cost is not well defined, so low at the center of the artery and high elsewhere. The presented method considers the geometry of both arteries (ICA and ECA) in a minimum cost path approach, which results in significantly less failure cases ($p < 0.0001$) than the approach obtaining the centerlines without any interaction between paths.

8.1.4 Population Studies

In Chapter 7 we presented a comparison between the quantified calcium volumes in CT and MRI to evaluate whether MRI can replace CT to detect and quantify calcified plaque. As several MRI sequences are necessary for a proper plaque detection and quantification, registration of the plaque components in the different images is necessary. Therefore, we used a registration approach to register the different MRI sequences to further annotate plaque calcifications. This registration approach is similar to the one used in [111], which employs mutual information as similarity metric in a ROI around the artery. Subsequently, the calcification volumes were compared to those obtained with CT, which resulted in a strong correlation ($r = 0.86$). Therefore, MRI could potentially be used to detect calcifications instead of using CT, thus avoiding the use of ionizing radiation.

8.2 Discussion

This thesis contributed to better segmenting the carotid artery lumen and wall. Chapters 2 and 3 presented approaches to segment the carotid artery wall in MRI, while in Chapter 4 a segmentation method of the lumen in US is presented. All methods are based on optimal surface graph models. The approach in Chapter 2 showed good lumen segmentations in MRI, while in Chapter 3 a good wall segmentation was achieved. The results show that the automated measurement can approach the precision of the manual measurements. Additionally, these results were better or in line with previous studies on similar data as [45, 103].

Lumen segmentations in US were fair in Chapter 4. However using these segmentations, good MRI-US registrations could be obtained in Chapter 5. More user interaction as in [51, 102], or the use of probability maps as described in Chapter 3 could be considered to improve the lumen segmentation results.

Using the optimal surface graph method the surfaces were not always smooth, as we were optimizing overlap without considering the smoothness of the segmented surfaces. A parameter tuning also targeting smoother results could help to obtain more visually appealing segmentations.

We obtained good MRI-US registrations in Chapter 5 with an average error of $\sim 0.8\,mm$. Using manual annotations to perform the registration resulted in a registration error of $\sim 0.4\,mm$ which suggests that improved segmentations should lead to better registrations. However, we consider an error of $\sim 0.8\,mm$, which is around the voxel size, sufficient for a side-by-side visualization. Other methods such as [24, 43, 72] reported higher errors, while in [91] better results were reported on a very small data set.

The cooperative approach to extract the centerlines in MRI presented in Chapter 6 resulted in significantly fewer centerline failure cases compared to the traditional approach to extract the centerlines separately, at the expense of an extra seed point

at the bifurcation. We think that better segmentation and registration results should be expected using the centerlines obtained by this method.

The limited amount of user interaction makes the methods that were developed in this thesis suitable for large scale analysis. In [98] the artery segmentations were used to relate wall shear stress measures to plaque regions, resulting in strong correlations. Additionally, in Chapter 7, calcium volumes extracted from CT and MRI were compared using a similar registration framework as described in Chapters 3 to register multiple MRI sequences from the same patient at the same time point. However, to use these methods in clinical practice, we recommend to validate the techniques further in the setting of a multi-center, multi-vendor study, and also including highly diseased patients.

For improving the chance of adopting in clinical research and practices, techniques to make the methods fully automatic could be explored. To automatically detect the seed points, methods as pixel-wise classification techniques which has been used with success to detect the carotid artery in MRI [78], or template matching methods [64] could be considered.

In conclusion, in this thesis we presented several (semi-)automatic tools to analyze the carotid artery in MRI and US. Most methods present good and robust results, so they can be used to support large scale analysis in population and clinical research and have the potential to be used to clinical practice.

Bibliography

[1] Reza Alizadeh Dehnavi, Joost Doornbos, Jouke T. Tamsma, Matthias Stuber, Hein Putter, Rob J. van der Geest, Hildo J. Lamb, Albert de Roos, "Assessment of the carotid artery by MRI at 3T: A study on reproducibility", *Journal of Magnetic Resonance Imaging*, vol. 25, no. 5, pp. 1035–1043, 2007.

[2] C P Allott, C D Barry, R Pickford, J C Waterton, "Volumetric assessment of carotid artery bifurcation using freehand-acquired, compound 3D ultrasound.", *British Journal of Radiology*, vol. 72, no. 855, pp. 289–92, 1999.

[3] A. Alwan & World Health Organization, *Global status report on noncommunicable diseases 2010.*, World Health Organization, Geneva, Switzerland, 2011.

[4] L. Antiga & D. A. Steinman, "Robust and Objective Decomposition and Mapping of Bifurcating Vessels", *IEEE Transactions on Medical Imaging*, vol. 23, no. 6, pp. 704–713, June 2004.

[5] Andres Arias, Jens Petersen, Arna van Engelen, Hui Tang, Mariana Selwaness, JacquelineC.M. Witteman, Aad Lugt, Wiro Niessen, Marleen Bruijne, "Carotid Artery Wall Segmentation by Coupled Surface Graph Cuts", in *Medical Computer Vision. Recognition Techniques and Applications in Medical Imaging*, vol. 7766 of *Lecture Notes in Computer Science*, Springer Berlin Heidelberg, pp. 38–47, 2013.

[6] A. M. Arias-Lorza, J. Petersen, A. van Engelen, M. Selwaness, A. van der Lugt, W. J. Niessen, M. de Bruijne, "Carotid Artery Wall Segmentation in Multispectral MRI by Coupled Optimal Surface Graph Cuts", *IEEE Transactions on Medical Imaging*, vol. 35, no. 3, pp. 901–911, March 2016.

[7] S. R. Aylward & E. Bullitt, "Initialization, noise, singularities, and scale in height ridge traversal for tubular object centerline extraction", *IEEE Transactions on Medical Imaging*, vol. 21, no. 2, pp. 61–75, Feb. 2002.

[8] Richard A Baheza, E Brian Welch, Daniel F Gochberg, Melinda Sanders, Sara Harvey, John C Gore, Thomas E Yankeelov, "Detection of microcalcifications by characteristic magnetic susceptibility effects using MR phase image cross-correlation analysis", *Medical physics*, vol. 42, no. 3, pp. 1436–1452, 2015.

[9] Hannah Bast, Daniel Delling, Andrew Goldberg, Matthias Müller-Hannemann, Thomas Pajor, Peter Sanders, Dorothea Wagner, Renato Werneck, "Route Planning in Transportation Networks", Tech. Rep. MSR-TR-2014-4, January 2014.

[10] Christian Bauer & Horst Bischof, *A Novel Approach for Detection of Tubular Objects and Its Application to Medical Image Analysis*, Springer Berlin Heidelberg, Berlin, Heidelberg, 2008, pp. 163–172.

[11] Christian Bauer, Thomas Pock, Erich Sorantin, Horst Bischof, Reinhard Beichel, "Segmentation of interwoven 3d tubular tree structures utilizing shape priors and graph cuts", *Medical Image Analysis*, Nov. 2009.

[12] Fethallah Benmansour & Laurent D. Cohen, "Fast Object Segmentation by Growing Minimal Paths from a Single Point on 2D or 3D Images", *Journal of Mathematical Imaging and Vision*, vol. 33, no. 2, pp. 209–221, 2008.

[13] Maren Bennewitz & Wolfram Burgard, "Finding solvable priority schemes for decoupled path planning techniques for teams of mobile robots", in *Proc. of the International Symposium on Intelligent Robotic Systems (SIRS)*, Citeseer, 2001.

[14] P. J. Besl & N. D. McKay, "A Method for Registration of 3-D Shapes", *IEEE Transactions on Pattern Analysis and Machine Intelligence*, vol. 14, pp. 239–256, 1992.

[15] Daniel Bos, M Arfan Ikram, Suzette E Elias-Smale, Gabriel P Krestin, Albert Hofman, Jacqueline CM Witteman, Aad van der Lugt, Meike W Vernooij, "Calcification in major vessel beds relates to vascular brain disease", *Arteriosclerosis, thrombosis, and vascular biology*, vol. 31, no. 10, pp. 2331–2337, 2011.

[16] Daniel Bos, Marileen LP Portegies, Aad van der Lugt, Michiel J Bos, Peter J Koudstaal, Albert Hofman, Gabriel P Krestin, Oscar H Franco, Meike W Vernooij, M Arfan Ikram, "Intracranial carotid artery atherosclerosis and the risk of stroke in whites: the Rotterdam Study", *JAMA neurology*, vol. 71, no. 4, pp. 405–411, 2014.

[17] Y. Boykov & V. Kolmogorov, "An experimental comparison of min-cut/max-flow algorithms for energy minimization in vision", *IEEE Transactions on Pattern Analysis and Machine Intelligence*, vol. 26, no. 9, pp. 1124–1137, 2004.

[18] S. Carr, A. Farb, W.H. Pearce, R. Virmani, J.S. Yao, "Atherosclerotic plaque rupture in symptomatic carotid artery stenosis", *Journal of Vascular Surgery*, vol. 23, no. 5, p. 755, 1996.

[19] D.D.B. Carvalho, S. Klein, Z. Akkus, G. L. ten Kate, A.F.L. Schinkel, J.G. Bosch, A van der Lugt, W.J. Niessen, "Estimating 3D lumen centerlines of carotid arteries in free-hand acquisition ultrasound", *International Journal of Computer Assisted Radiology and Surgery*, vol. 7, pp. 207–215, 3 2012.

[20] D.D.B. Carvalho, S. Klein, Z. Akkus, A. C van Dijk, H. Tang, M. Selwaness, A.F.L. Schinkel, J.G. Bosch, A. van der Lugt, W.J. Niessen, "Joint intensity-and-point based registration of free-hand B-mode ultrasound and MRI of the carotid artery", *Medical physics*, vol. 41, no. 5, p. 052904, 2014.

[21] Diego D.B. Carvalho, Andres Mauricio Arias Lorza, Wiro J. Niessen, Marleen de Bruijne, Stefan Klein, "Automated Registration of Freehand B-Mode Ultrasound and Magnetic Resonance Imaging of the Carotid Arteries Based on Geometric Features", *Ultrasound in Medicine & Biology*, vol. 43, no. 1, pp. 273 – 285, 2017.

[22] J.A. Chalela, "Evaluating the carotid plaque: going beyond stenosis", *Cerebrovascular Diseases*, vol. 27, no. Suppl. 1, pp. 19–24, 2009.

[23] Chih-Chung Chang & Chih-Jen Lin, "LIBSVM: A library for support vector machines", *ACM Transactions on Intelligent Systems and Technology*, vol. 2, no. 3, pp. 27:1–27:27, 2011.

[24] B. Chiu, V. Shamdasani, R. Entrekin, C. Yuan, W.S. Kerwin, "Characterization of Carotid Plaques on 3-Dimensional Ultrasound Imaging by Registration With Multicontrast Magnetic Resonance Imaging", *Journal of Ultrasound in Medicine*, vol. 31, no. 10, pp. 1567–1580, 2012.

[25] Laurent D. Cohen & Ron Kimmel, "Global Minimum for Active Contour Models: A Minimal Path Approach", *International Journal of Computer Vision*, vol. 24, no. 1, pp. 57–78.

[26] Cholesterol Treatment Trialists' (CTT) Collaborators, "Efficacy and safety of cholesterol-lowering treatment: prospective meta-analysis of data from 90056 participants in 14 randomised trials of statins", *The Lancet*, vol. 366, no. 9493, pp. 1267 – 1278, 2005.

[27] Olivier Cuisenaire, "Fully automated segmentation of carotid and vertebral arteries from CTA", in *Carotid Lumen Segmentation and Stenosis Grading Challenge (part of the MICCAI 2009 Grand Challenge III workshop)*, Kitware Inc., pp. http–hdl, 2009.

[28] P. J. de Koning, J. A. Schaap, J. P. Janssen, J. J. Westenberg, R. J. van der Geest, J. H. Reiber, "Automated segmentation and analysis of vascular structures in magnetic resonance angiographic images", *Magn Reson Med*, vol. 50, no. 6, pp. 1189–1198, Dec 2003.

[29] Thomas T de Weert, Mohamed Ouhlous, Erik Meijering, Pieter E Zondervan, Johanna M Hendriks, Marc RHM van Sambeek, Diederik WJ Dippel, Aad van der Lugt, "In vivo characterization and quantification of atherosclerotic carotid plaque components with multidetector computed tomography and histopathological correlation", *Arteriosclerosis, thrombosis, and vascular biology*, vol. 26, no. 10, pp. 2366–2372, 2006.

[30] A. Delong & Y. Boykov, "Globally optimal segmentation of multi-region objects", in *Computer Vision, 2009 IEEE 12th International Conference on*, pp. 285–292, Sept 2009.

[31] Lee R. Dice, "Measures of the amount of ecologic association between species", *Ecology*, vol. 26(3), pp. 297–302, 1945.

[32] E. W. Dijkstra, "A Note on Two Problems in Connexion with Graphs", *NUMERISCHE MATHEMATIK*, vol. 1, no. 1, pp. 269–271, 1959.

[33] GA Donnan, M Fisher, M Macleod, SM Davis, "Stroke", *Lancet*, 2008.

[34] M.A Fischler, J.M Tenenbaum, H.C Wolf, "Detection of roads and linear structures in low-resolution aerial imagery using a multisource knowledge integration technique", *Computer Graphics and Image Processing*, vol. 15, no. 3, pp. 201 – 223, 1981.

[35] Alejandro F. Frangi, Wiro J. Niessen, Koen L. Vincken, Max A. Viergever, *Multiscale vessel enhancement filtering*, Springer Berlin Heidelberg, Berlin, Heidelberg, 1998, pp. 130–137.

[36] Moti Freiman, Noah Broide, Miriam Natanzon, Einav Nammer, Ofek Shilon, Lior Weizman, Leo Joskowicz, Jacob Sosna, "Vessels-Cut: a graph based approach to patient-specific carotid arteries modeling", in *Proceedings of the 2009 international conference on Modelling the Physiological Human*, 3DPH'09, Springer-Verlag, Berlin, Heidelberg, pp. 1–12, 2009.

[37] A. Gee, R. Prager, G. Treece, C. Cash, L. Berman, "Processing and visualizing three-dimensional ultrasound data", *Br J Radiol*, vol. 77, no. suppl_2, pp. S186–193, 2004.

[38] J. Golledge, R.M. Greenhalgh, A.H. Davies, "The symptomatic carotid plaque", *Stroke*, vol. 31, no. 3, pp. 774–781, 2000.

[39] J. Golledge & D.A. Siew, "Identifying the carotid 'high risk' plaque: is it still a riddle wrapped up in an enigma?", *European Journal of Vascular and Endovascular Surgery*, vol. 35, no. 1, p. 2, 2008.

[40] Scandinavian Simvastatin Survival Study Group, "Randomised trial of cholesterol lowering in 4444 patients with coronary heart disease: the Scandinavian Simvastatin Survival Study (4S)", *The Lancet*, vol. 344, no. 8934, pp. 1383 – 1389, 1994.

[41] M. Akif Gülsün & Hüseyin Tek, "Robust Vessel Tree Modeling", in *MICCAI*, MICCAI '08, Springer-Verlag, Berlin, Heidelberg, pp. 602–611, 2008.

[42] Mehmet A Gülsün & Hüseyin Tek, "Segmentation of carotid arteries by graph-cuts using centerline models", in *SPIE Medical Imaging*, International Society for Optics and Photonics, pp. 762530–762530, 2010.

[43] Hengkai Guo, Guijin Wang, Lingyun Huang, Yuxin Hu, Chun Yuan, Rui Li, Xihai Zhao, "A Robust and Accurate Two-Step Auto-Labeling Conditional Iterative Closest Points (TACICP) Algorithm for Three-Dimensional Multi-Modal Carotid Image Registration", *PLoS ONE*, vol. 11, no. 2, pp. 1–22, 02 2016.

[44] M. Haeker, X. Wu, M. Abramoff, R. Kardon, M. Sonka, "Incorporation of regional information in optimal 3-D graph search with application for intraretinal layer segmentation of optical coherence tomography images", *Inf Process Med Imaging*, vol. 20, pp. 607–618, 2007.

[45] K. Hameeteman, R. van 't Klooster, M Selwaness, A. van der Lugt, J.C.M. Witteman, W.J. Niessen, S. Klein, "Carotid wall volume quantification from magnetic resonance images using deformable model fitting and learning-based correction of systematic errors", *Physics in Medicine and Biology*, vol. 58, 2013.

[46] K. Hameeteman, M.A. Zuluaga, M. Freiman, L. Joskowicz, O Cuisenaire, L. Florez Valencia, M.A. Gulsun, K. Krissian, J. Mille, W.C.K. Wong, M. Orkisz, H. Tek, M. Hernandez Hoyos, F. Benmansour, A.C.S. Chung, S. Rozie, M.J. van Gils, L. van den Borne, J. Sosna, P. Berman, N. Cohen, P. Douek, I. Sańchez, M. Aissat, M. Schaap, C.T. Metz, G. P. Krestin, A van der Lugt, W.J. Niessen, T. van Walsum, "Evaluation framework for carotid bifurcation lumen segmentation and stenosis grading", *Medical Image Analysis*, vol. 15, no. 4, pp. 477–488, 8 2011.

[47] R. Joop Heekeren, Frank G. A. Faas, Lucas J. Vliet, *Image Analysis: 15th Scandinavian Conference, SCIA 2007, Aalborg, Denmark, June 10-14, 2007*, Springer Berlin Heidelberg, Berlin, Heidelberg, 2007, Ch. Finding the Minimum-Cost Path Without Cutting Corners, pp. 263–272.

[48] Albert Hofman, Guy GO Brusselle, Sarwa Darwish Murad, Cornelia M van Duijn, Oscar H Franco, André Goedegebure, M Arfan Ikram, Caroline CW Klaver, Tamar EC Nijsten, Robin P Peeters, others, "The Rotterdam Study: 2016 objectives and design update", *European journal of epidemiology*, vol. 30, no. 8, pp. 661–708, 2015.

[49] M. Hossain, K. AlMuhanna, L. Zhao, B. Lal, S. Sikdar, "Semiautomatic segmentation of atherosclerotic carotid artery lumen using 3D ultrasound imaging", in *SPIE Medical Imaging*, International Society for Optics and Photonics, pp. 86694A–86694A, 2013.

[50] Murad Hossain, Khalid AlMuhanna, Limin Zhao, Brajesh K. Lal, Siddhartha Sikdar, "Semi-automatic segmentation of atherosclerotic carotid artery lumen using 3D ultrasound imaging", in *Medical Imaging: Computer-Aided Diagnosis. Proceedings of SPIE.*, Bram van Ginneken & Carol L. Novak (eds.), 2013.

[51] Md. Murad Hossain, Khalid AlMuhanna, Limin Zhao, Brajesh K. Lal, Siddhartha Sikdar, "Semiautomatic segmentation of atherosclerotic carotid artery wall volume using 3D ultrasound imaging", *Medical Physics*, vol. 42, no. 4, pp. 2029–2043, 2015.

[52] H. Ishikawa, "Exact optimization for Markov random fields with convex priors", *Pattern Analysis and Machine Intelligence, IEEE Transactions on*, vol. 25, no. 10, pp. 1333–1336, 2003.

[53] Y. Jin & H. M. Ladak, "Software for interactive segmentation of the carotid artery from 3D black blood magnetic resonance images", *Comput Methods Programs Biomed*, vol. 75, no. 1, pp. 31–43, Jul 2004.

[54] S. Klein, J. P. W. Pluim, M. Staring, M. A. Viergever, "Adaptive Stochastic Gradient Descent Optimisation for Image Registration", *International Journal of Computer Vision*, vol. 81, pp. 227–239, 2009.

[55] Stefan Klein, Marius Staring, K. Murphy, Max Viergever, Josien Pluim, "Elastix: a toolbox for intensity-based medical image registration", *IEEE Transactions on Medical Imaging*, vol. 29, no. 1, pp. 196–205, 2010.

[56] Jaroslaw Krejza, Michal Arkuszewski, Scott E. Kasner, John Weigele, Andrzej Ustymowicz, Robert W. Hurst, Brett L. Cucchiara, Steven R. Messe, "Carotid Artery Diameter in Men and Women and the Relation to Body and Neck Size", *Stroke*, vol. 37, no. 4, pp. 1103–1105, 2006.

[57] Robert M Kwee, "Systematic review on the association between calcification in carotid plaques and clinical ischemic symptoms", *Journal of vascular surgery*, vol. 51, no. 4, pp. 1015–1025, 2010.

[58] Robert M Kwee, Gerrit JJ Teule, Robert J van Oostenbrugge, Werner H Mess, Martin H Prins, Rob J van der Geest, Johannes WM ter Berg, Cees L Franke, Arthur GGC Korten, Bé J Meems, others, "Multimodality Imaging of Carotid Artery Plaques", *Stroke*, vol. 40, no. 12, pp. 3718–3724, 2009.

[59] H. M. Ladak, J. S. Milner, D. A. Steinman, "Rapid three-dimensional segmentation of the carotid bifurcation from serial MR images", *J Biomech Eng*, vol. 122, no. 1, pp. 96–99, Feb 2000.

[60] David Lesage, Elsa D. Angelini, Isabelle Bloch, Gareth Funka-Lea, "A review of 3D vessel lumen segmentation techniques: Models, features and extraction schemes", *Medical Image Analysis*, vol. 13, no. 6, pp. 819 – 845, 2009. Includes Special Section on Computational Biomechanics for Medicine.

[61] Kang Li, Xiaodong Wu, Danny Z. Chen, Milan Sonka, "Optimal surface segmentation in volumetric images – a graph-theoretic approach", *IEEE Transactions on Pattern Analysis and Machine Intelligence*, vol. 28, no. 1, pp. 119–134, 2006.

[62] Peter Libby, Paul M Ridker, Göran K Hansson, "Progress and challenges in translating the biology of atherosclerosis", *Nature*, vol. 473, no. 7347, pp. 317–325, 2011.

[63] Shubao Liu, Dirk Padfield, Paulo Mendonca, "Tracking of carotid arteries in ultrasound images", in *Medical Image Computing and Computer-Assisted Intervention–MICCAI 2013*, Springer Berlin Heidelberg, pp. 526–533, 2013.

[64] Shubao Liu, Dirk Padfield, Paulo Mendonca, "Tracking of Carotid Arteries in Ultrasound Images", in *Medical Image Computing and Computer-Assisted Intervention MICCAI 2013*, vol. 8150 of *Lecture Notes in Computer Science*, Springer Berlin Heidelberg, pp. 526–533, 2013.

[65] Xiaomin Liu, Danny Z. Chen, Merryn H. Tawhai, Xiaodong Wu, Eric A. Hoffman, Milan Sonka, "Optimal Graph Search Based Segmentation of Airway Tree Double Surfaces Across Bifurcations", *IEEE Trans. Med. Imaging*, vol. 32, no. 3, pp. 493–510, 2013.

[66] Andres M.Arias Lorza, Diego D.B. Carvalho, Jens Petersen, Anouk C. Dijk, Aad Lugt, Wiro J. Niessen, Stefan Klein, Marleen Bruijne, "Carotid Artery Lumen Segmentation in 3D Free-Hand Ultrasound Images Using Surface Graph Cuts", in *Medical Image Computing and Computer-Assisted Intervention MICCAI 2013*, Kensaku Mori, Ichiro Sakuma, Yoshinobu Sato, Christian Barillot, Nassir Navab (eds.), vol. 8150 of *Lecture Notes in Computer Science*, Springer Berlin Heidelberg, pp. 542–549, 2013.

[67] Lozano et al., "Global and regional mortality from 235 causes of death for 20 age groups in 1990 and 2010: a systematic analysis for the Global Burden of Disease Study 2010", *The Lancet*, vol. 380, no. 9859, pp. 2095 – 2128, 2013.

[68] Aldons J Lusis, "Atherosclerosis", *Nature*, vol. 407, pp. 233–241, 2000.

[69] S. Mendis, P. Puska, B. Norrving, World Health Organization, World Heart Federation, World Stroke Organization, *Global atlas on cardiovascular disease prevention and control.*, World Health Organization, Geneva, Switzerland, 2011.

[70] Dariush Mozaffarian, Emelia J Benjamin, Alan S Go, Donna K Arnett, Michael J Blaha, Mary Cushman, Sandeep R Das, Sarah de Ferranti, Jean-pierre Després, Heather J Fullerton, others, "Executive summary: Heart Disease and Stroke Statistics-2016 update: A report from the American Heart Association.", *Circulation*, vol. 133, no. 4, p. 447, 2016.

[71] Mayberg MR, Wilson S, Yatsu F, et al, "Carotid endarterectomy and prevention of cerebral ischemia in symptomatic carotid stenosis", *JAMA*, vol. 266, no. 23, pp. 3289–3294, 1991.

[72] N. D. Nanayakkara, B. Chiu, A. Samani, J. D. Spence, J. Samarabandu, G. Parraga, A. Fenster, "Nonrigid registration of three-dimensional ultrasound and magnetic resonance images of the carotid arteries", *Medical Physics*, vol. 36, no. 2, pp. 373–385, 2009.

[73] Kiran R Nandalur, Erol Baskurt, Klaus D Hagspiel, Michael Finch, C Douglas Phillips, Sirisha R Bollampally, Christopher M Kramer, "Carotid artery calcification on CT may independently predict stroke risk", *American Journal of Roentgenology*, vol. 186, no. 2, pp. 547–552, 2006.

[74] Arlette E Odink, Aad van der Lugt, Albert Hofman, Myriam GM Hunink, Monique MB Breteler, Gabriel P Krestin, Jacqueline CM Witteman, "Association between calcification in the coronary arteries, aortic arch and carotid arteries: the Rotterdam study", *Atherosclerosis*, vol. 193, no. 2, pp. 408–413, 2007.

[75] DRJ Owen, AC Lindsay, RP Choudhury, ZA Fayad, "Imaging of atherosclerosis", *Annual review of medicine*, vol. 62, pp. 25–40, 2011.

[76] Jens Petersen, Mads Nielsen, Pechin Lo, Lars Haug Nordenmark, Jesper Holst Pedersen, Mathilde Marie Winkler Wille, Asger Dirksen, Marleen de Bruijne, "Optimal surface segmentation using flow lines to quantify airway abnormalities in chronic obstructive pulmonary disease", *Medical Image Analysis*, vol. 18, no. 3, pp. 531–541, 2014.

[77] Jens Petersen, Mads Nielsen, Pechin Lo, Zaigham Saghir, Asger Dirksen, Marleen De Bruijne, "Optimal graph based segmentation using flow lines with application to airway wall segmentation", in *Proceedings of the 22nd international conference on Information processing in medical imaging*, IPMI'11, Springer-Verlag, Berlin, Heidelberg, pp. 49–60, 2011.

[78] Esben Plenge, Stefan S Klein, Wiro J Niessen, Erik Meijering, "Multiple sparse representations classification", *PloS one*, vol. 10, no. 7, p. e0131968, 2015.

[79] Thomas Pock, Reinhard Beichel, Horst Bischof, "A Novel Robust Tube Detection Filter for 3D Centerline Extraction", in *Image Analysis*, Heikki Kalviainen, Jussi Parkkinen, Arto Kaarna (eds.), vol. 3540 of *Lecture Notes in Computer Science*, Springer Berlin / Heidelberg, Berlin, Heidelberg, Ch. 49, pp. 55–94, 2005.

[80] Miroslav Radojević, Ihor Smal, Erik Meijering, "Fuzzy-Logic Based Detection and Characterization of Junctions and Terminations in Fluorescence Microscopy Images of Neurons", *Neuroinformatics*, pp. 1–19, 2015.

[81] RJ Rennenberg, AG Kessels, LJ Schurgers, JM Van Engelshoven, PW De Leeuw, AA Kroon, "Vascular calcifications as a marker of increased cardiovascular risk: a meta-analysis", *Vasc Health Risk Manag*, vol. 5, no. 1, pp. 185–197, 2009.

[82] Mathieu H. Rodallec, Vronique Marteau, Sophie Gerber, Loc Desmottes, Marc Zins, "Craniocervical Arterial Dissection: Spectrum of Imaging Findings and Differential Diagnosis1", *Radiographics*, vol. 28, no. 6, pp. 1711–1728, 2008.

[83] D. Rueckert, L.I. Sonoda, C. Hayes, D.L.G. Hill, M.O. Leach, D.J. Hawkes, "Nonrigid registration using free-form deformations: application to breast MR images", *Medical Imaging, IEEE Transactions on*, vol. 18, no. 8, pp. 712–721, 1999.

[84] T Saam, MS Ferguson, VL Yarnykh, N Takaya, D Xu, NL Polissar, TS Hatsukami, C Yuan, "Quantitative evaluation of carotid plaque composition by in vivo MRI", *Arteriosclerosis, Thrombosis, and Vascular Biology*, vol. 25, no. 1, pp. 234–239, 2005.

[85] M. Schaap, C.T. Metz, T. van Walsum, A.G. van der Giessen, A.C. Weustink, N.R.A. Mollet, C. Bauer, H. Bogunović, C. Castro, X. Deng, E. Dikici, T. O'Donnell, M. Frenay, O. Friman, M. Hernández Hoyos, P.H. Kitslaar, K. Krissian, C. Kühnel, M. A. Luengo-Oroz, M. Orkisz, Ö Smedby, M. Styner, A. Szymczak, H. Tek, C. Wang, S. K. Warfield, S. Zambal, Y. Zhang, G. P. Krestin, W.J. Niessen, "Standardized Evaluation Methodology and Reference Database for Evaluating Coronary Artery Centerline Extraction Algorithms", *Medical Image Analysis*, vol. 13/5, pp. 701–714, 2009.

[86] U. Schminke, L. Motsch, B. Griewing, M. Gaull, C. Kessler, "Three-dimensional power-mode ultrasound for quantification of the progression of carotid artery atherosclerosis", *J. Neurol.*, vol. 247, no. 2, pp. 106–111, Feb 2000.

[87] Mariana Selwaness, Reinhard Hameeteman, Ronald Van 't Klooster, Quirijn Van den Bouwhuijsen, Albert Hofman, Oscar H. Franco, Wiro J. Niessen, Stefan Klein, Meike W. Vernooij, Aad Van der Lugt, Jolanda J. Wentzel, "Determinants of carotid atherosclerotic plaque burden in a stroke-free population", *Atherosclerosis*, vol. 255, pp. 186 – 192, 2016.

[88] J. A. Sethian, "Fast Marching Methods", *SIAM Review*, vol. 41, no. 2, pp. 199–235, 1999.

[89] Mauro Silvestrini, Barbara Rizzato, Fabio Placidi, Roberto Baruffaldi, Alberto Bianconi, Marina Diomedi, "Carotid Artery Wall Thickness in Patients With Obstructive Sleep Apnea Syndrome", *Stroke*, vol. 33, no. 7, pp. 1782–1785, 2002.

[90] M. Sitzer, W. Muller, M. Siebler, W. Hort, H. W. Kniemeyer, L. Jancke, H. Steinmetz, "Plaque ulceration and lumen thrombus are the main sources of cerebral microemboli in high-grade internal carotid artery stenosis", *Stroke*, vol. 26, no. 7, pp. 1231–1233, Jul 1995.

[91] P. J. Slomka, J. Mandel, D. Downey, A. Fenster, "Evaluation of voxel-based registration of 3-D power Doppler ultrasound and 3-D magnetic resonance angiographic images of carotid arteries", *Ultrasound in Medicine & Biology*, vol. 27, no. 7, pp. 945–955, 2001.

[92] C. Studholme, D.L.G. Hill, D.J. Hawkes, "An overlap invariant entropy measure of 3D medical image alignment", *Pattern Recognition*, vol. 32, no. 1, pp. 71 – 86, 1999.

[93] Norihide Takaya, Chun Yuan, Baocheng Chu, Tobias Saam, Hunter Underhill, Jianming Cai, Nam Tran, Nayak L. Polissar, Carol Isaac, Marina S. Ferguson, Gwenn A. Garden, Steven C. Cramer, Kenneth R. Maravilla, Beverly Hashimoto, Thomas S. Hatsukami, "Association Between Carotid Plaque Characteristics and Subsequent Ischemic Cerebrovascular Events: A Prospective Assessment With MRIInitial Results", *Stroke*, vol. 37, no. 3, pp. 818–823, 2006.

[94] H. Tang, T. van Walsum, R. S. van Onkelen, K. Hameeteman, S. Klein, M. Schaap, Q. J.A. B Bouwhuijsen, J.C.M. Witteman, A. van der Lugt, L. J. van Vliet, W.J. Niessen, "Semiautomatic Carotid Lumen Segmentation for Quantification of Lumen Geometry in Multispectral MRI", *Medical Image Analysis*, vol. 16, no. 6, pp. 1202–1215, 8 2012.

[95] Hui Tang, Theo van Walsum, Robbert S. van Onkelen, Stefan Klein, Reinhard Hameeteman, Michiel Schaap, Quirijn J. A. van den Bouwhuijsen, Jacqueline C. M. Witteman, Aad van der Lugt, Lucas J. van Vliet, Wiro J. Niessen, "Multispectral MRI centerline tracking in carotid arteries", 2011.

[96] Adrien Treuille, Seth Cooper, Zoran Popović, "Continuum Crowds", *ACM Trans. Graph.*, vol. 25, no. 3, pp. 1160–1168, July 2006.

[97] M. T. B. Truijman, M. E. Kooi, A. C. van Dijk, A. A. J. de Rotte, A. G. van der Kolk, M. I. Liem, F. H. B. M. Schreuder, E. Boersma, W. H. Mess, R. J. van Oostenbrugge, P. J. Koudstaal, L. J. Kappelle, P. J. Nederkoorn, A. J. Nederveen, J. Hendrikse, A. F. W. van der Steen, M. J. A. P. Daemen, A. van der Lugt, "Plaque At RISK (PARISK): prospective multicenter study to improve diagnosis of high-risk carotid plaques", *International Journal of Stroke*, vol. 9, no. 6, pp. 747–754, 2014.

[98] A. Tuenter, M. Selwaness, A. Arias Lorza, J.C.H. Schuurbiers, L. Speelman, M. Cibis, A. van der Lugt, M. de Bruijne, A.F.W. van der Steen, O.H. Franco, M.W. Vernooij, J.J. Wentzel, "High shear stress relates to intraplaque haemorrhage in asymptomatic carotid plaques", *Atherosclerosis*, vol. 251, pp. 348 – 354, 2016.

[99] Greg Turk & James F. O'Brien, "Shape transformation using variational implicit functions", in *Proceedings of the 26th annual conference on Computer graphics and interactive techniques*, SIGGRAPH '99, ACM Press/Addison-Wesley Publishing Co., pp. 335–342, 1999.

[100] N.J. Tustison, B.B. Avants, P.A. Cook, Yuanjie Zheng, A. Egan, P.A. Yushkevich, J.C. Gee, "N4ITK: Improved N3 bias correction", *IEEE Transactions on Medical Imaging*, vol. 29(6), pp. 1310 – 1320, 2010.

[101] E. Ukwatta, J. Awad, D. Buchanan, G. Parraga, A. Fenster, "Three-dimensional semi-automated segmentation of carotid atherosclerosis from three-dimensional ultrasound images", in *SPIE Medical Imaging*, International Society for Optics and Photonics, pp. 83150O–83150O, 2012.

[102] E. Ukwatta, J. Awad, D. Buchanan, G. Parraga, A. Fenster, "Three-dimensional semi-automated segmentation of carotid atherosclerosis from three-dimensional ultrasound images", in *Medical Imaging: Computer-Aided Diagnosis. Proceedings of SPIE.*, Bram van Ginneken & Carol L. Novak (eds.), 2012.

[103] E. Ukwatta, Jing Yuan, M. Rajchl, Wu Qiu, D. Tessier, A. Fenster, "3-D Carotid Multi-Region MRI Segmentation by Globally Optimal Evolution of Coupled Surfaces", *Medical Imaging, IEEE Transactions on*, vol. 32, no. 4, pp. 770–785, 2013.

[104] Quirijn JA Van Den Bouwhuijsen, Daniel Bos, M Arfan Ikram, Albert Hofman, Gabriel P Krestin, Oscar H Franco, Aad Van der Lugt, Meike W Vernooij, "Coexistence of calcification, intraplaque hemorrhage and lipid core within the asymptomatic atherosclerotic carotid plaque: the Rotterdam Study", *Cerebrovascular Diseases*, vol. 39, no. 5-6, pp. 319–324, 2015.

[105] Quirijn J.A. van den Bouwhuijsen, Meike W. Vernooij, Albert Hofman, Gabriel P. Krestin, Aad van der Lugt, Jacqueline C.M. Witteman, "Determinants of magnetic resonance imaging detected carotid plaque components: the Rotterdam Study", *European Heart Journal*, 2011.

[106] Quirijn J. A. van den Bouwhuijsen, Mariana Selwaness, Hui Tang, Wiro J. Niessen, Albert Hofman, Oscar H. Franco, Aad van der Lugt, Meike W. Vernooij, "Change in Carotid Intraplaque Hemorrhage in Community-dwelling Subjects: A Follow-up Study Using Serial MR Imaging", *Radiology*, vol. 282, no. 2, pp. 526–533, 2017. PMID: 27541684.

[107] A. C. van der Wal & A. E. Becker, "Atherosclerotic plaque rupture–pathologic basis of plaque stability and instability.", *Cardiovascular research*, vol. 41, no. 2, pp. 334–344, Feb. 1999.

[108] MJ Van Gils, MC Bodde, LGM Cremers, DWJ Dippel, Aad van der Lugt, "Determinants of calcification growth in atherosclerotic carotid arteries; a serial multi-detector CT angiography study", *Atherosclerosis*, vol. 227, no. 1, pp. 95–99, 2013.

[109] MJ Van Gils, Danijela Vukadinovic, AC Van Dijk, DWJ Dippel, WJ Niessen, Aad van der Lugt, "Carotid atherosclerotic plaque progression and change in plaque composition over time: a 5-year follow-up study using serial CT angiography", *American Journal of Neuroradiology*, vol. 33, no. 7, pp. 1267–1273, 2012.

[110] Ronald van 't Klooster, Patrick J.H. de Koning, Reza Alizadeh Dehnavi, Jouke T. Tamsma, Albert de Roos, Johan H.C. Reiber, Rob J. van der Geest, "Automatic lumen and outer wall segmentation of the carotid artery using deformable three-dimensional models in MR angiography and vessel wall images", *Journal of Magnetic Resonance Imaging*, vol. 35, no. 1, pp. 156–165, 2012.

[111] R. van 't Klooster, M. Staring, S. Klein, R.M. Kwee, M.E. Kooi, J. H. C. Reiber, B.P.F. Lelieveldt, R.J. van der Geest, "Automated registration of multispectral MR vessel wall images of the carotid artery", *Medical Physics*, vol. 40, no. 12, pp. 121904–1 – 121904–12, 2013.

[112] Chunliang Wang & Orjan Smedby, "An automatic seeding method for coronary artery segmentation and skeletonization in CTA", *The Insight Journal*, pp. 1–8, 2008.

[113] I. Wendelhag, T. Gustavsson, M. Suurkula, G. Berglund, J. Wikstrand, "Ultrasound measurement of wall thickness in the carotid artery: fundamental principles and description of a computerized analysing system", *Clin Physiol*, vol. 11, no. 6, pp. 565–577, Nov 1991.

[114] Renske G Wieberdink, Mariëlle MF Poels, Meike W Vernooij, Peter J Koudstaal, Albert Hofman, Aad van der Lugt, Monique MB Breteler, M Arfan Ikram, "Serum lipid levels and the risk of intracerebral hemorrhage: the Rotterdam Study", *Arteriosclerosis, thrombosis, and vascular biology*, vol. 31, no. 12, pp. 2982–2989, 2011.

[115] R. L. Wilensky, H. K. Song, V. A. Ferrari, "Role of magnetic resonance and intravascular magnetic resonance in the detection of vulnerable plaques", *J. Am. Coll. Cardiol.*, vol. 47, no. 8 Suppl, pp. 48–56, Apr 2006.

[116] Wilbur CK Wong, Ronald WK So, Albert CS Chung, "Principal curves: a technique for preliminary carotid lumen segmentation and stenosis grading", *MIDAS Journal*, 2009.

[117] Ting-Fan Wu, Chih-Jen Lin, Ruby C Weng, "Probability estimates for multi-class classification by pairwise coupling", *Journal of Machine Learning Research*, vol. 5, no. 975-1005, p. 4, 2004.

[118] Xiaodong Wu & Danny Chen, "Optimal Net Surface Problems with Applications", in *Automata, Languages and Programming*, Peter Widmayer, Stephan Eidenbenz, Francisco Triguero, Rafael Morales, Ricardo Conejo, Matthew Hennessy (eds.), vol. 2380 of *Lecture Notes in Computer Science*, Springer Berlin / Heidelberg, pp. 775–775, 2002.

[119] Xiaodong Wu, Xin Dou, A. Wahle, M. Sonka, "Region Detection by Minimizing Intraclass Variance With Geometric Constraints, Global Optimality, and Efficient Approximation", *Medical Imaging, IEEE Transactions on*, vol. 30, no. 3, pp. 814–827, March 2011.

[120] X. Xu, M. Niemeijer, Q. Song, M.K. Garvin, J.M. Reinhardt, M.D. Abramoff, "Retinal vessel width measurements based on a graph-theoretic method", in *Biomedical Imaging: From Nano to Macro, 2011 IEEE International Symposium on*, pp. 641–644, April 2011.

[121] Sebastian Zambal, Jirı Hladuvka, Armin Kanitsar, K Bühler, "Shape and appearance models for automatic coronary artery tracking", *The Insight Journal*, vol. 4, 2008.

[122] L. Zhang, S. Parrini, C. Freschi, V. Ferrari, S. Condino, M. Ferrari, D. Caramella, "3D ultrasound centerline tracking of abdominal vessels for endovascular navigation", *International Journal of Computer Assisted Radiology and Surgery*, vol. 9, no. 1, pp. 127–135, 2013.

Samenvatting

In dit proefschrift hebben we verscheidene (semi) - automatische beeldverwerkingstechnieken voorgesteld voor het analyseren van het lumen en de vaatwand van de halsslagader in MRI en Echografie. De gepresenteerde methoden omvatten beeldsegmentatie, beeldregistratie, extractie van de vaat-middellijn en kwantificering van componenten.

Segmentatie

In hoofdstuk 2 hebben we een nieuwe methode gepresenteerd om de halsslagaderwand in MRI te segmenteren. Segmentatie van de slagaderwand is een belangrijke stap in de detectie en de analyse van de samenstelling van een atherosclerotische plaque. De -methode segmenteert tegelijkertijd zowel de binnen- als de buitenwandgrens op basis van een graafsnede die een optimale oplossing garandeert. Lokale beeldinformatie in de vorm van beeld afgeleiden wordt gebruikt. De methode maakt het ook mogelijk meerdere MRI-sequenties te integreren, waarmee complementaire informatie uit de verschillende afbeeldingen gebruikt kan worden. We hebben hiermee goede binnenwandsegmentaties en redelijke buitenwandsegmentaties verkregen. De prestatie van zowel de binnen- als de buitenwandsegmentatie was vergelijkbaar met andere onlangs gepubliceerde halsslagadersegmentatiemethoden. Het voordeel van de hier gepresenteerde methode is dat het minder gebruikersinteractie vereist, enkel drie gemarkeerde punten in de slagader, en dat de volledige bifurcatie wordt gesegmenteerd.
In hoofdstuk 3 hebben we de methode beschreven in hoofdstuk 2 uitgebreid om nog nauwkeurigere segmentaties te krijgen. Aangezien de methode die wordt gepresenteerd in hoofdstuk 2 alleen beeld afgeleiden als lokale beeldinformatie gebruikt, is deze relatief gevoelig voor ruis en gebrek aan lokaal beeldcontrast. Dat resulteerde in fouten specifiek bij de buitenwand van de slagaderwand, waar het contrast in het algemeen minder is dan bij de binnenwand. De methode uit hoofdstuk 2 hebben we daarom uitgebreid met meer beeldkenmerken dan alleen beeld afgeleiden. Deze beschrijvende beeldkenmerken worden dan met behulp van voxel classificatie omgerekend naar waarschijnlijkheden per klasse. De graafsnede maximaliseert vervolgens de waarschijnlijkheden per gebied (lumen, wand, of achtergrond) om de uiteindelijke segmentatie te bepalen. We hebben aangetoond dat deze methode beter is dan die in hoofdstuk 2, en resulteert in goede segmentaties van zowel de binnen- als de buitenwand.
In hoofdstuk 4 hebben we een methode gepresenteerd om het halsslagaderlumen in

3-dimensionale echografie beelden te segmenteren. Halsslagaders worden vaak met de echografie in beeld gebracht. Lumensegmentatie in deze echobeelden zou het mogelijk maken de geometrie van de halsslagader en de vernauwing als gevolg van aderverkalking te onderzoeken. Voor deze segmentatie hebben we een vergelijkbare graafbenadering gebruikt als beschreven in hoofdstuk 2, maar dan om alleen de binnenste rand van de slagader te segmenteren. In echografie zien de wanden van de slagaders er echter onregelmatiger uit in vergelijking met MRI. De graafbenadering is daarom iteratief toegepast zodat deze ook werkt in gevallen waar de initialisatie zeer ver van de vaatwand ligt. Bij toepassing van deze segmentatiemethode werden goede resultaten verkregen bij gezonde vrijwilligers, en redelijke resultaten bij patinten.

MRI-Echo Registratie

In hoofdstuk 5 hebben we een methode gepresenteerd om de halsslagader in MRI en echografie te registreren met behulp van geometrische kenmerken. Vaat-middellijnen en lumensegmentaties zijn gebruikt als registratiekenmerken. Registratie is nodig om analyse en visualisatie van de complementaire informatie van beide beeldvormende modaliteiten te vergemakkelijken. Echter, huidige methoden om MRI en echografie beelden te registreren geven grote fouten wanneer correlatie van intensiteit wordt gebruikt voor registratie, of vereisen een grote mate van gebruikersinteractie. We hebben de methoden uit hoofdstukken 2 en 4 gebruikt om de vaat-midellijnen te extraheren en de lumensegmentaties in respectievelijk MRI en echografie te verkrijgen. De registratieprocedure vindt een transformatie het verschil tussen deze geometrische kenmerken minimaliseert. Goede registraties werden verkregen met fouten in de orde van grootte van de MRI en echografie voxelgrootte.

Vaat-midellijnextractie

In hoofdstuk 6 hebben we een nieuwe methode gepresenteerd om de twee halsslagadermiddellijnen tegelijkertijd te extraheren. De middellijn is belangrijk om de geometrie van het bloedvat te analyseren en wordt gebruikt als input voor segmentatie- en registratiemethoden. In het algemeen worden de twee middellijnen van CCA naar ICA en van CCA naar ECA afzonderlijk gedetecteerd. Dit, samen met het gebruik van minimale-kosten-paden, kan leiden tot fouten als de kosten niet goed gedefinieerd zijn. De gepresenteerde methode beschouwt de geometrie van beide slagaders (ICA en ECA) in de minimale-kosten-padenbenadering, wat resulteert in aanzienlijk minder fouten dan de aanpak waarbij beide middellijnen afzonderlijk van elkaar worden beschouwd.

Populatiestudies

In hoofdstuk 7 hebben we een vergelijking tussen de calciumvolumes gemeten in CT en MRI gepresenteerd om te beoordelen of een MRI scan de CT-scan kan vervangen om aderverkalking te detecteren en te kwantificeren. Aangezien verscheidene MRI-sequenties nodig zijn voor een goede plaque-detectie en kwantificering, is het nodig om de plaque-componenten in de verschillende beelden te registreren. Daarom hebben

we de verschillende MRI-sequenties eerst geregistreerd om vervolgens de verkalking te annoteren. Daarna is de hoeveelheid kalk gemeten in MRI vergeleken met de hoeveelheid verkregen met CT, wat resulteerde in een sterke correlatie. MRI kan daarom mogelijk gebruikt worden om calcificaties te detecteren in plaats van CT, wat het gebruik van ioniserende straling zou vermijden.

PhD Portfolio

In-Depth Courses:

- Biomedical English Writing, ErasmusMC, 2012-2013
- Knowledge Driven Image Segmentation, ASCI, 2012
- Advanced Pattern Recognition, ASCI, 2012
- Front end Vision & Multi-Scale Image Analysis, ASCI, 2011

International Conference Attendance:

- MICCAI 2013, Nagoya Japan, 09-2013
- MICCAI 2012, Nice France, 09-2012
- European Congress of Radiology 2012, Vienna Austria, 02-2012

Summer Schools:

- Medical Imaging Summer School, Favignana Italy, 07-2014
- Computer Vision Summer School, Sicily Italy, 07-2012
- Biomedical Image Analysis Summer School, Paris France, 07-2012

Other Activities:

- Medical Informatics Research presentations, ErasmusMC, 2011-2015
- COEUR Research seminar, ErasmusMC, 2012
- Model Base group meetings, ErasmusMC, 2011-2015
- BIGR seminars, ErasmusMC, 2011-2015
- Literature meetings organizer, ErasmusMC, 2013-2015

- Biostress group meetings, ErasmusMC, 2011-2015
- Vascular group meetings, ErasmusMC, 2011-2014

Publications

Publications in International Journals:

- B. Mujaj, **A. Arias Lorza**, A. van Engelen, M. de Bruijne, O. H. Franco, A. van der Lugt, M. W. Vernooij, D. Bos, *"Comparison of CT and MRI for detection and quantification of carotid artery calcification: The Rotterdam Study,"* Journal of Cardiovascular Magnetic Resonance, 2017

- D.D.B. Carvalho, **A. Arias Lorza**, W.J. Niessen, M. de Bruijne, and S. Klein, *Automated Registration of Freehand B-Mode Ultrasound and Magnetic Resonance Imaging of the Carotid Arteries Based on Geometric Features,* Ultrasound in Medicine & Biology, 2016

- M. Cibis, Potters, M Selwaness, F.J.H. Gijsen, O. Franco, **A. Arias Lorza**, M. de Bruijne, A. Hofman, A. van der Lugt, A. Nederveen and J.J. Wentzel, *Relation between wall shear stress and carotid artery wall thickening MRI versus CFD,* Journal of Biomechanics, 2016

- Van Tuenter, M Selwaness, **A. Arias Lorza**, J.C.H. Schuurbiers, L Speelman, M. Cibis, A. van der Lugt, M. de Bruijne, A.F.W. van der Steen, O. Franco, M.W. Vernooij and J.J. Wentzel, *High shear stress relates to intraplaque haemorrhage in asymptomatic carotid plaques,* Atherosclerosis, 2016

- **A. Arias Lorza**, J. Petersen, A. van Engelen, M. Selwaness, A. van der Lugt, W.J. Niessen and M. de Bruijne, *Carotid Artery Wall Segmentation in Multispectral MRI by Coupled Optimal Surface Graph Cuts,* IEEE Transactions on Medical Imaging, 2015

- **A. Arias Lorza**, A. van Engelen, J. Petersen, A. van der Lugt, and M. de Bruijne, *"Maximization of Regional probabilities using Graphs: Application to Carotid Artery Segmentation in MRI,"* submitted

- **A. Arias Lorza**, D. Bos, A. van der Lugt, and M. de Bruijne, *"Cooperative Carotid Artery Centerline Extraction in MRI,"* submitted

Publications in International Conference Proceedings:

- **A. Arias Lorza**, D.D.B. Carvalho, J. Petersen, A.C. van Dijk, A. van der Lugt, W.J. Niessen, S. Klein and M. de Bruijne, *Carotid artery lumen segmentation in 3D free-hand ultrasound images using surface graph cuts,"* MICCAI, 2013
- **A. Arias Lorza**, J. Petersen, A. van Engelen, H. Tang, M Selwaness, A. van der Lugt, W.J. Niessen and M. de Bruijne, *Carotid artery wall segmentation by coupled surface graph cuts,,* MICCAI Medical Computer Vision Workshop, 2012

Acknowledgments

There were many people that contributed to the realization of this thesis during these years of my PhD studies that I want to thank and acknowledge.

First, I start with my parents Guillermo and Ana Milena because thanks to their support I was able to carry out my studies. Spanish: Estimados padres gracias por todo el apoyo que me han dado para que realizara mi sueño de obtener una educacion de primer nivel, los aprecio mucho, esta tesis de PhD tambien es de ustedes.

Next I want to thank my promoter Wiro and co-promoter Marleen. First of all, thanks both for giving me the opportunity to be part of a great research group as BIGR. Wiro thanks for being always positive and friendly, you are an example to me to follow. Marleen, you gave me freedom to present new ideas and projects, but at the same time you helped me to develop and improve these ideas. I learned from you many value lessons in how to be a researcher.

I want to acknowledge the rest of my family. They were attentive of how I was doing during the PhD, also giving me moral support. Spanish: Gracias a mi hermano Alex, su esposa Maria Fernanda, mi sobrino Nicolas, mis tios Elsy, Harold y esposa Berta, Patty y familia por estar pendientes durante estos años de estudios.

During these years I met many valuable people. First I want to acknowledge great friends I made in the medical informatics department. Osemeke, Diego, Rene, Gerardo, Pierre thanks for the friendship and the uncountable joyful moments. Special thanks to Osemeke and Diego for also being my paranymphs. I also want to acknowledge other great people I met in the department I spent memorable times: Fabiola, Jean Marie, Wei Sun, Esben, and Daniel. In general, I want to recognize all other members of BIGR for being always kind, willing to help, for the times at the lunch breaks, the outings, research drinks,... I had a very good time, thanks!

There were several collaborators that I want to recognize. Arna, I was pleased to work with you, also thanks for helping me with the Dutch translation of the summary. Stefan, you were not only a collaborator but also a very friendly person, it was nice working with you. Blerim, you were very diligent and kind. I also want to recognize all members of the model base group (Zahra, Annegreet, Esther, Adria, Hakim, Gijs) for their collaboration. Finally, I want to thank some external collaborators: Aad,

Daniel Bos, Jens Petersen, and Jolanda.

I should also recognize the great work of the secretaries and human resources staff from the department. Desiree, Petra and Andreas thanks for your kindness and diligence.

Social life was very important to me during the PhD, so I want to thank several friends outside Erasmus: Erica, John, Hector, Manuel, Ozgur, Patricio, Salas, Srinu, and Yeisson thanks for your friendship.

I want to finalize acknowledging a very special person I met during the PhD. Dear Sylwia, we have spent many remarkable moments, and I hope there are more to come. Thanks for all your patience and support. Also thanks for helping me with the Dutch translation of the summary together with your friend Bas.

Curriculum Vitae

I was born in Cali, Colombia. I received my bachelor degree in Electrical engineer from the Javeriana University, Cali, Colombia, in 2007. Between 2009 and 2011, I followed the master of science in embedded system from Eindhoven University of Technology, Eindhoven, The Netherlands. From 2011 to 2016 I was a Ph.D. student at the Biomedical imaging group (BIGR) in the departments for Medical Informatics and Radiology from Erasmus MC, Rotterdam, The Netherlands. My research mainly consisted in the development of tools for the automatic segmentation, registration, center-line extraction, and geometry analysis of the carotid artery from diverse image modalities as MRI and Ultrasound.